ALUMINUM NITRIDE-ON-SILICON TEMPERATURE-STABLE RESONATORS AND FILTERS FOR TIMING APPLICATIONS

by

Vikram Atul Thakar

A dissertation submitted in partial fulfillment
of the requirements for the degree of
Doctor of Philosophy
(Mechanical Engineering)
in The University of Michigan
2014

Doctoral Committee:

Assistant Professor Mina Rais-Zadeh, Chair
Professor Yogesh Gianchandani
Professor Karl Grosh
Professor Khalil Najafi

© Vikram Thakar

All rights reserved

2014

To

Friends and Family

Acknowledgements

First and foremost I would like to thank my advisor, Professor Mina Rais-Zadeh, for providing me the opportunity to pursue this research and supporting me through the years. I also thank my thesis committee members, Professor Karl Grosh, Professor Khalil Najafi, and Professor Yogesh Gianchandani for their help and support. Through interactions with them during research meetings, academic conferences and course work, I have grown both as a researcher and as an individual.

I would like to take this opportunity to thank my group members in the resonant MEMS group. Yonghyun, Zhengzheng and Vikrant have provided a good source of intellectual stimulation through discussions and played the role of family away from home. Azadeh, Adam and more recently Muzhi, Cesar and Feng have continued that tradition. I will be forever grateful for their help and support and for providing a friendly and conducive research environment in the lab.

WIMS, the umbrella organization for research in Microsystems at the University of Michigan has played a strong role in my development as a MEMS researcher. This work has benefited profusely due to the ancillary support provided through WIMS to student members.

This work would not have been complete without the support, guidance and the patience of the Lurie Nanofabrication Facility staff. I would like to thank them for bearing with me through the years and supporting my research efforts in the

cleanroom. I would also like to thank my colleagues working in the cleanroom for providing ample company, moral support and process training. The long nights spent in the cleanroom were enjoyable to a large part due to their support and friendship. In particular, I would like to thank Dr. Jae Yoong Cho, Dr. Razi-ul Haque, Dr. Erkan Aktakka, Dr. Ali Besharatian, Dr. Tao Ling, Dr. Zongliang Cao, Katherine Knisely, Dr. Anurag Tripathi, Dr. Seokjun Park, Dr. Animesh Banerjee, Dr. Ayan Das, Professor Gaurav Bahl, Dr. Anne Itsuno, Dr. Alex Kaplan, Kyunghoon Lee, Yi Yuan, Stacey Tang, Jun Tang for their advice and support.

My friends at Michigan, Girish Kulkarni, Siddharth Gaba, Saniya Deshpande, Deepti Joshi, Kishore Aravamudhan, Jallal El-Hazzat, Dr. Victor Lee, Ning Gulari, Dr. Seow Yuen Yee, Dr. Naveen Gupta, Sarang Supekar and Prasad Shingne have given me plenty of reasons to smile and am truly grateful for their support.

My friends from India have kept in touch and have constantly motivated me to work harder to accomplish my goals. I came to Michigan in 2008 with their encouragement and support and I am extremely happy that their support continues to this day.

I would like to thank my cousins who helped me settle down in the US through moral, emotional and financial support. My nephew, Advay and niece Avani have been a treat to interact with and my life has been truly enriched by their presence.

Finally, I want to express my deepest appreciation to my parents and sister who have always encouraged me to pursue my dreams. This thesis would not have been possible without their unconditional love and support.

TABLE OF CONTENTS

Dedication ii

Acknowledgements iii

List of Figures x

List of Tables xx

Abstract xxii

Chapter 1 Introduction to Resonators and Frequency References 1

1.1 Background and Motivation 1

1.2 Classification of Micromachined Resonators 3

1.2.1 Electrostatic Actuation 4

1.2.2 Piezoelectric Actuation 6

1.2.3 Other Actuation Mechanisms 8

1.3 Loss Mechanisms in Mechanical Resonators 9

1.4 Temperature Compensation of Micromachined Resonators 13

1.5 Temperature stable precision timing references 14

1.6 Research Objectives 16

1.7 Organization of Thesis 20

Chapter 2 Temperature Compensation and Piezoelectric Actuation of Silicon resonators 21

2.1 Flexural Mode Resonators 23

2.1.1 Position dependence of passive compensation 24

2.1.2 Experimental Verification 28

2.1.3 Fabrication process 29

2.1.4 Resonator Design 32

2.1.5 Measured Results 34

2.1.6 Active Temperature Compensation 37

2.1.7 Estimation of Resonator Stability 41

2.1.8 Flexural-Mode Resonator: Summary of Results 42

2.2 Coupled-Ring Resonators 44

2.2.1 Device Structure 44

2.2.2 Device Geometry 45

2.2.3 Temperature Compensation 45

2.2.4 Resonator Fabrication 46

2.2.5 Measured Results 48

Chapter 3 Description of the Multi-Resonator Clock and its Implementation . 51

3.1 Description of the Multi-Resonator Clock 53

3.2 Sensitivity to Resonator Drift 55

3.3 Sensitivity to Measurement Errors ... 56

3.3.1 Non-uniform temperature distribution in measurement chamber .. 56

3.3.2 Temperature sensor calibration error ... 57

3.4 Other sources of non-idealities ... 58

3.5 Oscillator Implementation ... 59

3.5.1 Oscillator Circuit ... 59

3.5.2 Oscillator Measurements ... 61

3.6 System Implementation ... 64

3.6.1 Oscillator Temperature Dependence ... 64

3.6.2 Estimation of system multipliers ... 65

3.6.3 Clock Measurement Results ... 65

3.7 Discussion ... 69

Chapter 4 Experimental Investigation of Loss Mechanisms in Lamé-Mode Resonators ... 71

4.1 Electrostatically Actuated Lamé-Mode Resonators ... 74

4.1.1 Device structure ... 74

4.1.2 Estimation of anchor loss ... 74

4.1.3 Optimization of tether geometry for Lamé-mode resonators ... 77

4.1.4 Origin of anchor loss in Lamé-mode resonators ... 78

4.1.5 Experimental Verification ... 80

4.2 Temperature Compensation of Lamé-mode Resonators 83
4.2.1 Fabrication process of temperature-compensated capacitive Lamé-mode resonators 85
4.2.2 Measured Results 87
4.3 Piezoelectrically Actuated Temperature-Compensated Lamé Resonators 91
4.3.1 Resonator Design 91
4.3.2 Fabrication process of temperature-compensated piezoelectrically actuated Lamé resonators... 94
4.3.3 Measured Results 96
4.4 Conclusions 100
Chapter 5 Acoustically Coupled AlN-on-Silicon Filters 103
5.1 Introduction and Motivation... 103
5.2 Thickness-Extension Acoustically Coupled Filters 106
5.2.1 Working Principle 107
5.2.2 Equivalent Electrical Model of Acoustically Coupled Filters...... 110
5.2.3 Fabrication Process.. 111
5.2.4 Measurement Results 113
5.2.5 Finite Element Modeling of Acoustically Coupled filters 119
5.2.6 Design guidelines for acoustically coupled filters 128
5.3 In-plane acoustically coupled filters.. 138

5.3.1 Design of an in-plane acoustically coupled filter 138

5.3.2 Finite element modeling of the filter response 141

5.3.3 Measured Results 142

5.3.4 In-plane filters: Merits and Challenges 144

5.4 Conclusions 146

Chapter 6 Future Work 148

6.1 Summary 148

6.2 Future Research Directions 149

6.2.1 Clock Implementation 149

6.2.2 AlN-on-Silicon Lamé-Mode Resonators..................................... 149

6.2.3 In-Plane Acoustically Coupled Filters 151

Appendix A-1 Dispersion Curves 154

Bibliography 160

LIST OF FIGURES

Figure 1-1: Block diagram of a MEMS oscillator. 2

Figure 1-2: Classification of micro-mechanical resonators based on their transduction mechanism. 3

Figure 1-3: (Left) SEM image of an electrostatically-actuated Lamé-mode resonator [12]. (Right) A schematic of the resonator highlighting the important parameters. 4

Figure 1-4 : (Left) A SEM image of a piezoelectrically actuated AlN-on-silicon flexural-mode resonator. (Right) A schematic of the resonator highlighting the top electrode layout designed to excite the in-plane flexural mode piezoelectrically. 7

Figure 1-5: Classification of the important loss mechanisms in resonators. 10

Figure 1-6: Block diagram of the proposed multi-resonator temperature stable frequency reference. 15

Figure 2-1: A schematic view of the AlN-on-silicon resonator, showing the flexural mode of operation. The tuning electrodes are not shown in this schematic. 24

Figure 2-2: (a) Simulated mode shape and (b) simulated strain energy density along section A-A'. (c) A close-up view of the strain energy density variation across the resonator flange cross-section. The overlaid parabolic curve (in black) represents the variation of the strain across the width of the resonator flange. The color spectrum in (a) plots the total displacement and in (b) and (c) plots the strain energy density. 25

Figure 2-3: Location of oxide-refilled trenches within the resonator (not to scale). Trenches with similar hatch/fill patterns form a trench pair. The section A-A' corresponds to that seen in Figure 2-2. 26

Figure 2-4: Plot showing the variation in strain energy density (normalized) across the width of the resonator. Only one half of the flange width is shown here. The TCF of the composite resonator is plotted as a function of the trench location. A clear correlation between the strain energy across the trench and the resonator TCF can be observed. In all cases, the width of the oxide trenches is 5.5 μm and the total volume of oxide is the same. 27

Figure 2-5: Different trench configurations used in the experimental verification of passive temperature compensation. All trenches have the same dimensions and are shown

with dotted lines. The spacing between the two etched trenches is kept as 1.5 µm (as marked) in order to ensure that the trenches are fully refilled with thermal oxide........... 28

Figure 2-6: Fabrication process flow of the AlN-on-silicon flexural-mode resonators.... 30

Figure 2-7: (a) An SEM image of a fabricated resonator. There are a total of eight tuning electrodes, which can be used for tuning the center frequency. (b) A close-up view showing the metal routing on the central rod. The black line (dash-dot) marks the outline of the resonating body.. 31

Figure 2-8: Cross-section SEM images showing the oxide-refilled trenches for a two trench sample. The close-up view on the right reveals small air pockets formed during the refill process, which is caused as an effect of scalloping seen during the trench DRIE... 32

Figure 2-9: Measured response of the resonators with (a) no TCF compensation (b) single oxide-refilled trench (c) two oxide-refilled trenches and (d) three oxide-refilled trenches. All measurements are taken in vacuum and at room temperature. 34

Figure 2-10: Measured resonance frequency as a function of temperature for different trench configurations. In case of no trench and single trench resonators, the TCF value is averaged across the temperature range. For the case of two and three trench devices, the TCF value is estimated at 25 °C. 35

Figure 2-11: Measured peak frequency shift in parts per million (ppm) as a function of temperature for different trench configurations. Inset: measured results in a smaller ppm range... 36

Figure 2-12: Measured and calculated frequency tuning as a function of applied DC voltage for a trenchless device. (a) The change in peak frequency and (b) the total frequency tuning in ppm. 38

Figure 2-13: (a) Measured frequency change with temperature for a three trench device. The tuned frequency with applied DC voltage is also plotted to demonstrate the viability of this approach in achieving temperature stable resonators. (b) Tuned peak frequency as a function of temperature and voltage. The graph details the tuning error for multiple measurements (total 20 readings at each temperature) at each voltage setting and the average value. The tuning error is within 1 ppm and is set by power supply fluctuations, resonator drift and the stability of the temperature controller. 39

Figure 2-14: Cross-section schematic of the AlN-on-silicon flexura-mode resonator, detailing the stack layers and the measurement conditions for piezoelectric tuning........ 40

Figure 2-15: Measured bidirectional frequency tuning using the piezoelectric effect. The total tuning range is measured to be 5 Hz for a three-trench device. The tuning range can be significantly improved by improving the thickness ratio of AlN to silicon in the device. 40

Figure 2-16: Measured drift of the resonator center frequency (a) without and (b) with feedback control loop. (c) Histogram plot of the resonator center frequency with feedback control showing the calculated statistical parameters assuming a Gaussian distribution. The resonator intrinsic drift is seen to be better than 110 ppb (3σ number). 42

Figure 2-17: Schematic of a temperature-compensated coupled-ring breathing-mode resonator. The oxide-refilled regions are clearly marked for clarity. Note that the schematic does not show the piezoelectric stack. 44

Figure 2-18: Simulated mode shape of the coupled-ring resonator 45

Figure 2-19: Simulated turnover temperature for the compensated ring resonators as a function of 'edge' spacing. This dimension is marked for clarity in Figure 2-17. Note that all devices have the same 23.5 µm width of silicon dioxide.. 46

Figure 2-20: Process flow used in the fabrication of the ring resonators. 47

Figure 2-21: Cross-section SEM view of the oxide-refilled trenches within the silicon volume... 47

Figure 2-22: SEM view showing a fully released temperature compensated ring resonator. Note that the oxide rings are not visible due to the presence of the piezoelectric stack... 48

Figure 2-23: Measured frequency response for three temperature-compensated resonators. The measured result for an uncompensated ring resonator is also included for comparison. All measurements are carried out at room temperature and pressure with input power of -10 dBm. 49

Figure 2-24: Measured relative frequency shift in ppm as a function of temperature for the three temperature-compensated resonators shown in Figure 2-23............................. 50

Figure 3-1: Schematic of the proposed multi-resonator clock algorithm. The system requires the development of two main components: multiple resonators with unique turnover temperatures and low bandwidth, low insertion loss bandpass filters to reject the unwanted frequency products at the mixer output. 52

Figure 3-2: Graphical representation of the temperature dependence of the clock frequency output due to (a) temperature errors during measurement and (b) constant temperature sensor calibration error. Note that the plots are representative and are not drawn to scale. 58

Figure 3-3: Circuit diagram of the oscillator implementation using the pierce configuration. The same design is suitable for all the temperature compensated oscillators needed in the proposed multi-resonator system. 60

Figure 3-4: PCB with three out of four oscillator circuits connected. The MEMS chip (resonators) is fixed and wire-bonded to a package for making the circuit connections.. 60

Figure 3-5: Output of the three oscillators on the PCB having three different temperature-compensated resonators. 61

Figure 3-6: Measured phase noise plot for a typical pierce oscillator implemented using the presented temperature-compensated ring resonators. 62

Figure 3-7: Measured relative frequency shift (df/f) as a function of temperature for the three oscillators shown in Figure 3-5. Solid symbols are used to represent the measured data points and the lines represent the least squares fit to the measured data, the equations of which are used in the calculation of the k coefficients. 64

Figure 3-8: Schematic of the full clock system implemented using discrete circuit elements. 66

Figure 3-9: Measured clock output using the oscillators shown in Figure 3-7 and the system shown in Figure 3-8. The uncertainty in frequency measurement is ~ 0.4 ppm. . 67

Figure 3-10: Measured temperature dependence of the individual oscillators along with that of the final system for comparison. 67

Figure 3-11: Measured *Q* for different ring resonators as a function of its temperature compensation design. The 'edge' labels indicate the distance of the oxide from the resonator edge. The 'No TCF' label indicates the uncompensated device without any oxide rings. 70

Figure 4-1: A SEM image of a fabricated electrostatically-actuated Lamé-mode resonator. The close-in schematic on the right identifies the tether geometry variables. 74

Figure 4-2: Model of a beam resonator for anchor loss estimation. The interface region ensures a smooth transition from the beam to the highly attenuating PML region. 76

Figure 4-3: Simulated anchor *Q* for a silicon beam resonator as a function of alpha. The silicon beam is 500 μm long and 7.2 μm wide. The analytical estimate of anchor *Q* for the third-order flexural mode (clamped-clamped boundary) is calculated to be 11,177 [30]. 77

Figure 4-4: Simulated anchor *Q* as a function of the tether length for a 100 μm × 100 μm Lamé-mode resonator. The total simulated *Q* is calculated using the simulated anchor *Q* and the phonon-phonon $f \times Q$ limit in silicon as 2.2×10^{13} [24]. The simulated frequency for these designs is ~ 41.5 MHz. The two local *Q* minima's in the plot correspond with the first two flexural modes of the supporting tether equaling the Lamé-mode frequency. 77

Figure 4-5: (a) Simulated Lamé-mode for a 100 μm square plate. (b) First two flexural modes of the supporting tether equaling the frequency of the Lamé-mode, at tether lengths of 3.3 μm and 11.5 μm. These two tether lengths correspond with the two minima's in the simulated anchor *Q* plot in Figure 4-4. 80

Figure 4-6: Process flow used to fabricate the capacitively transduced Lamé-mode resonators. ... 80

Figure 4-7: Comparison of the measured resonator Q for three different dies with the simulated Q for the 100 μm × 100 μm Lamé-mode resonators. ... 81

Figure 4-8: Measured response of a high-Q Lamé-mode resonator with tether length of 17.5 μm and tether width of 2 μm. A DC bias of 250 V was applied during measurement. (Inset) A SEM image of the resonator. ... 82

Figure 4-9: Representative schematic showing the location of the oxide-refilled trenches embedded within the silicon Lamé-mode resonator. The simulated thermoelastic damping dependent Q and anchor Q for this design are 2.37×10^6 and 0.71×10^6, respectively... 83

Figure 4-10: Temperature dependence of frequency for four designs with different spacing (gap) between the oxide-refilled trenches. The four designs have turnover (TO) temperatures of -40 °C, 0 °C, 40 °C and 80 °C, respectively. Thus, it is clear that by changing the gap, we can change the turnover temperature, without modifying the process parameters. ... 84

Figure 4-11: Fabrication process flow for the temperature-compensated Lamé-mode resonators. ... 86

Figure 4-12: A microscope image of a temperature-compensated Lamé-mode resonator. The four oxide-refilled square trenches can be clearly seen through the polysilicon cap layer. ... 86

Figure 4-13: Measured frequency response of a temperature-compensated Lamé-mode resonator. This resonator has a tether length of 10 μm and a tether width of 2 μm. ... 87

Figure 4-14: Measured frequency response of an uncompensated Lamé-mode resonator. This resonator has a tether length of 17.5 μm and a tether width of 2 μm. While the planar geometry is same as for the result presented in Figure 4-8, this device includes a 1μm polysilicon layer over the low-resistivity silicon device layer. The reduced Q as compared to Figure 4-8 may be due to the inclusion of a 1 μm polysilicon capping layer, amongst other factors. ... 88

Figure 4-15: Measured temperature dependence of frequency for four different temperature-compensated Lamé-mode resonators each having a different 'gap' between oxide-refilled trenches. Thus, we can tune the turnover temperature by varying the 'gap' between the oxide-refilled trenches. ... 89

Figure 4-16: (a) A cross-section SEM image of a temperature-compensated Lamé-mode resonator. The depth of the oxide-refilled trenches (~ 20 μm) can be clearly seen in this image. (b) Close-in SEM view of the oxide-refilled trench. Small silicon regions are visible in between the refilled oxide. ... 89

Figure 4-17: Measured resonator Q as a function of its operating frequency. The resonator center frequency has a strong correlation with its temperature compensation. Black line (dotted) represents the least squares linear fit to the measured data. 90

Figure 4-18: Schematic of a temperature-compensated Lamé-mode resonator. The location of the oxide-refilled trenches and the triangle shaped top electrode layout can be clearly seen.. 92

Figure 4-19: Simulated turnover temperature for the Lamé-mode resonator as a function of 'gap' between the oxide-refilled islands. The schematic on the right marks the location of the oxide within the resonator. The inset on the left plots the simulated strain energy across the resonator. The large sensitivity of temperature compensation to the 'gap' variable is due to the relatively sharp change in strain energy close to the resonator center. 92

Figure 4-20: Net strain across the AlN surface for (a) uncompensated and (b) compensated Lamé-mode resonator. The presence of the oxide islands is seen to skew the strain profile. The color gradient plots the change in net strain across the surface, with red and blue representing positive and negative strains respectively. 93

Figure 4-21: Simulated $|S_{21}|$ for a temperature-compensated (with oxide) and uncompensated (without oxide) Lamé-mode resonator. Simulated response assumes a resonator Q of 100,000. 94

Figure 4-22: Process flow used for the fabrication of temperature-compensated piezoelectrically-actuated Lamé-mode resonators.. 95

Figure 4-23: Cross-section SEM images of (a) the DRIE trenches to be oxidized, (b) a single oxide-refilled island.. 95

Figure 4-24: A SEM image of a fabricated Lamé-mode resonator. The top input and output ports are labeled with '+' and '-' respectively and resembles the net strain profile seen in Figure 4-20. The oxide-refilled trenches are embedded within the silicon body and are not visible through the top metal layer.. 96

Figure 4-25: Measured frequency response of a (left) temperature-compensated and (right) uncompensated piezoelectrically-actuated Lamé-mode resonator, measured at room temperature and in vacuum.. 97

Figure 4-26: Measured peak frequency shift as a function of temperature for three different 'gap' between the oxide islands. 97

Figure 4-27: Measured resonator Q as a function of its center frequency....................... 98

Figure 4-28: Measured resonator frequency, resonator Q and resonator insertion loss as a function of the temperature compensation of the resonator. As can be expected, for smaller 'gap' between the oxide islands, we have a higher resonator frequency. Note the lack of correlation between resonator Q and the 'gap' between the oxide islands. 99

Figure 4-29: Measured resonator insertion loss as a function of its quality factor. In order to achieve the simulated insertion loss of 35 dB, resonators with much higher *Q* will be essential.. 99

Figure 5-1: RF front-end of a modern cellular radio. Image reproduced from [68]....... 104

Figure 5-2: Schematic view of an acoustically coupled thickness-mode TPoS filter. The resonating sections are the areas defined by the input and output electrode fingers. The substrate layer is part of the resonating stack and is a 5 µm thick high resistivity (> 1 kΩ·cm) silicon device layer of an SOI wafer. 1 µm thick aluminum nitride is used as the piezoelectric layer and 100 nm molybdenum (Mo) is used as the top and bottom electrode material. 106

Figure 5-3: Dispersion curves of the fourth-order thickness-extensional (TE) mode and the nearest thickness-shear (TS) mode for the stack shown in Figure 5-2. The curves are computed using the Thomson-Haskell matrix technique with the thickness, Young's modulus, Poisson's ratio, and mass density of the different stack layers as inputs....... 108

Figure 5-4: Lateral waves coupling input and output electrodes with wavelengths corresponding to in-phase and out-of phase modes, superimposed over a two electrode section for clarity. 110

Figure 5-5: In-phase (a) and 180° out-of-phase (b) modes of a thickness-mode TPoS filter simulated using COMSOL®. The color spectrum plots the displacement. The two electroded regions are acoustically coupled and the coupling between them defines the filter bandwidth. The top electrode consists of 38 fingers with electrode width and spacing of 5 µm each. 110

Figure 5-6: Equivalent electrical circuit used to model acoustically coupled TPoS filters. 111

Figure 5-7: Fabrication process flow of a TPoS Filter [38]. The starting substrate is a high resistivity SOI wafer with Si device layer thickness of 5 µm ± 0.5 µm. In order to obtain better device uniformity, commercially available SOI wafers with a tight thickness tolerance (< 0.1 µm) or deposited polysilicon can be used... 112

Figure 5-8: A SEM image of an acoustically coupled TPoS Filter. This device has 10 pairs of top electrode fingers with finger length of 150 µm, finger width of 10 µm and finger spacing of 5 µm. 113

Figure 5-9: Measured (a) magnitude and (b) phase of S_{21} for the AlN-on-Si filter shown in Figure 5-8. The top electrode consists of 10 pairs of electrode fingers each 10 µm wide with 5 µm of inter-electrode spacing. 114

Figure 5-10: The dispersion plot for the TPoS filter stack shown in Figure 5-2. The measured filter response is superimposed for ease of comparison. From the plot, one can see that lateral waves with wavenumbers between 0.59 and 0.706 μm^{-1} in the electroded region contribute to the measured response.. 115

Figure 5-11: Measured and fitted responses for the AlN-on-Si TPoS filter seen in Figure 5-8. 116

Figure 5-12: The frequency response of the AlN-on-Si filter shown in Figure 5-8 at different RF power levels.. 118

Figure 5-13: (a) The peak frequency and (b) the insertion loss *vs.* temperature plots of the TPoS filter shown in Figure 5-8.. 119

Figure 5-14: (a) A cross-section schematic view of a TPoS filter showing the electrical boundary conditions used in 2D simulations and (b) a top view showing the electrode geometric variables (only the boxed area is modeled)... 121

Figure 5-15: A cross-section SEM image of the stack. The measured film thicknesses are used in the fitted simulation. Note that the buried oxide layer and the handle layer are removed from under the filter area. Inset shows a close-up view of the AlN film......... 123

Figure 5-16: Frequency response near the fourth-order thickness mode of the filter shown in Figure 5-8. The design curve shows the simulation result considering the nominal design values and material properties. The fitted response involves variation of geometric parameters and the piezoelectric stress constant, e_{33}. Insets show harmonic response at the in-phase and out-of-phase frequencies... 124

Figure 5-17: The measured and simulated (fitted) phase of the filter shown in Figure 5-8. 124

Figure 5-18: Simulated $|S_{21}|$ of the filter under varying AlN piezoelectric stress coefficient e_{33}. A reduced e_{33} of 1.1 C/m^2 is seen to best match the measured bandwidth and roll-off. The frequency shift seen with the increase in e_{33} may be attributed to the piezoelectric stiffening effect... 126

Figure 5-19: Simulated and measured filter response for (a) second and (b) third –order thickness-mode of resonance. 127

Figure 5-20: Comparison between the measured and simulated filter responses. All filters are on the same die. “n” is the number of electrode fingers. All devices have an electrode width in the range of 9.8 to 10.2 µm and finger spacing in the range of 4.8 to 5.2 µm with number of electrode fingers as shown in the plots. The actual thickness of the AlN and silicon layers as well as electrode dimensions were measured using SEM and used in these simulations. AlN e_{33} of 1.1 C/m^2 is used in all these simulations............. 127

Figure 5-21: Simulated filter (a) bandwidth and (b) insertion loss versus number of fingers for different spacing between electrode fingers. The electrode width is kept constant at 10 µm. All filters are centered around 2.9 GHz. 130

Figure 5-22: Simulated filter (a) bandwidth and (b) insertion loss versus number of fingers for different electrode widths. The electrode spacing is kept constant at 5 µm. All filters are at ~2.9 GHz.. 132

Figure 5-23: (a) Simulated filter response for n=20 and n=44 showing the generation of additional unwanted resonances in the passband as the number of fingers is increased beyond 40. For both curves the top electrode has a width of 10 µm and spacing of 5 µm. (b) Simulated effect of reduced piezoelectric stress constant in AlN. For both curves, the top electrode consists of 20 electrodes each 5 µm wide and having a spacing of 5 µm. 133

Figure 5-24: Simulated filter response indicating the effect of electrode width and electrode spacing. The top electrode layout is as marked. The number of electrode fingers is 20 in all cases. 134

Figure 5-25: Simulated response of a TPoS filter indicating the effect of the electrode thickness on the passband ripple. Increased electrode thickness improves the coupling and can reduce the ripple. Inset shows the filter response with electrode thickness of 200 nm. 134

Figure 5-26: Simulated filter bandwidth and insertion loss versus number of electrode fingers. For AlN-on-Si, the total device width is kept constant at 595 µm and interdigitated finger spacing is fixed at 5 µm. In case of ZnO the device width is 260 µm and finger spacing is 3 µm. In both cases, as the number of fingers is increased, the electrode width is decreased. The results for AlN are at ~2.9 GHz while those for ZnO are at ~1.8 GHz. 135

Figure 5-27: Simulated effect of silicon to AlN thickness ratio on the filter response. For both simulations, the top electrode geometry consists of 20 electrode fingers each 10 µm wide with 5 µm spacing in between. The AlN film thickness is 1 µm in both cases. A wider bandwidth with a larger ripple can be clearly seen for the stack with reduced silicon to AlN thickness ratio. 136

Figure 5-28: Schematic of an AlN-on-silicon contour-mode filter. The width of this structure is 200 µm. The device has the following stack geometry: 20 µm silicon, 100 nm Mo, 1 µm AlN and 100 nm of Au as the top electrode. (Not to scale) 139

Figure 5-29: Dispersion curves around the first order width-extension mode for the device geometry shown in Figure 5-28. The lateral overtone *i.e.* the out-of-phase mode can be designed to have a range of frequencies through the design of the plate length. The highlighted zone shows the frequency range in which the overtone mode should be designed to achieve a coupled filter response. 139

Figure 5-30: Simulated (a) in-phase *i.e.* the fundamental width-extension mode and (b) out-of-phase *i.e.* the first lateral overtone of the width-extension mode. 140

Figure 5-31: Modified representation of the dispersion curves shown in Figure 5-29 with filter frequency plotted as a function of the lateral wavelength as opposed to the lateral wavenumber.. 141

Figure 5-32: Simulated magnitude and phase of the S_{21}, for the in-plane filter shown in Figure 5-28. The filter has a plate width of 200 µm and plate length of 423 µm. The top electrode geometry consists of 2 electrodes with a gap of 10 µm. 142

Figure 5-33: Process flow used in the filter fabrication. (a) Deposit and pattern Mo (100 nm) as bottom electrode, 1 μm AlN as the piezo layer, and lift-off pattern Cr/Au (10/90 nm) as top electrode. (b) Etch resonator contour (RIE and DRIE) to get self-aligned devices and release from backside using DRIE and etch BOX layer using BHF........... 142

Figure 5-34: SEM image of a fabricated AlN-on-silicon in-plane acoustically coupled filter.. 143

Figure 5-35: Measured $|S_{21}|$ for the filter shown in Figure 5-34. This device has plate width of 200 and plate length of 423μm.. 143

Figure 5-36: Measured $|S_{21}|$ for two filters with plate width of 200 μm and plate length of 420 μm and 426 μm respectively. We see a 100 kHz shift in the out-of-phase mode with the change in the plate length in accordance with the nature of the dispersion curves of the width extension mode shown in Figure 5-31.. 144

Figure 6-1: Measured insertion loss of piezoelectrically-actuated Lamé-mode resonators as a function of its *Q*. The black line represents a least squares fit to the measured data. 151

Figure 6-2: Plot of frequency *vs*. wavelength and the rate of change of frequency with wavelength for a silicon plate oriented along (a) <100> and (b) <110> crystal axis. 152

Figure 6-3: (Top) Top electrode layout that may be utilized to implement a third order width-extension mode filter. (Bottom) Simulated mode shape for the 19th overtone of the third-order width-extension mode... 153

Figure A1-1: A multi-layer plate model with two material layers surrounded by air. ... 157

LIST OF TABLES

Table 2-1: Simulated resonator TCF at 25 °C for the four different trench configurations 26

Table 2-2: Material properties used in TCF simulations (all values are at 25 °C). 28

Table 2-3: Simulated TCF at 25 °C for the resonator configurations shown in Figure 2-5. 29

Table 2-4: Resonator geometry used for the experimental TCF characterization. 33

Table 2-5: Contribution of different loss mechanisms on the *Q* at 25 °C. The simulated Q_{Anchor} for the compensated structure assumes ideal geometry with perfectly rectangular refilled trenches. 33

Table 2-6: Ring resonator geometry optimized for high *Q* performance 45

Table 3-1: Comparison of measured phase noise (PN) for temperature-compensated oscillators operating between 1 to 100 MHz in literature. 63

Table 3-2: Extracted coefficients a, b, and c for the three oscillators shown in Figure 3-5 and Figure 3-7. 65

Table 4-1: Published measured data for electrostatically-actuated Lamé-mode resonators. The $f \times Q$ limit in silicon is estimated to be 2.2×10^{13} [24]. 72

Table 4-2: Comparison of the simulated anchor *Q* with analytically calculated estimates for flexural modes of a silicon beam resonator [30]. 78

Table 4-3: Analytically estimated critical tether length for a 100 µm × 100 µm Lamé-mode resonator. 79

Table 4-4: Estimated volume integral of strain in the AlN layer along the resonator in-plane axes showing the effect of silicon and oxide-refilled trenches on the effective charge pick-up. 94

Table 4-5: Analysis of the *Q* limit due to the inclusion of various interface elements in Lamé-mode resonators. 101

Table 5-1: Electromechanical coupling factor of the thickness-extensional modes for the electroded stack presented in Figure 5-2. 107

Table 5-2: Equivalent circuit element values for the filter response shown in Figure 5-11. 117

Table 5-3: Parameters used in the finite element simulations. 126

ABSTRACT

ALUMINUM NITRIDE-ON-SILICON TEMPERATURE-STABLE RESONATORS AND FILTERS FOR TIMING APPLICATIONS

by

Vikram Thakar

Silicon based micromechanical resonators have been successfully utilized as a replacement for Quartz in time keeping applications. Addition of silicon dioxide allows a reduction in the total temperature induced frequency shift for silicon based resonators from 3600 ppm to less than 100 ppm between -40 °C to +85 °C. While this makes their temperature stability comparable to Quartz, much improvement is needed to satisfy requirements for next generation wireless communication applications.

This thesis describes a novel algorithm utilizing three AlN-on-silicon micromechanical oscillators with unique temperature dependence to eliminate the 100 ppm temperature-induced frequency shift of individual oscillators. The frequency outputs from the three oscillators undergo frequency multiplication and mixing in two stages to achieve the temperature-insensitive frequency reference, without the need for accurate temperature sensing on-chip. The output of the mixers generate a number of spurious frequency products that need to be filtered out. AlN-on-silicon acoustically coupled filters are implemented to achieve the filtering function with a potential for a system-on-chip implementation. Such temperature-insensitive

precision clocks are potential candidates for use in small form factor systems, such as miniaturized inertial measurement units.

The design, fabrication, and experimental investigation of two critical building blocks in the clock algorithm are discussed; namely temperature-compensated MEMS resonators and acoustically coupled bandpass filters. Finite element modeling has been rigorously used in the design process to eliminate unnecessary fabrication trials. A novel passive temperature compensation strategy is implemented using silicon dioxide refilled trenches within the resonator body. Through control of the position of the oxide within the resonator, a fine control over the frequency-temperature characteristics of the oscillators is obtained, thus allowing for their use in the clock system. Using these oscillators, the multi-resonator clock is shown to provide a total frequency shift of less than ±4 ppm across -20 °C to +50 °C in a proof of concept implementation, demonstrating a 10× improvement over silicon oscillators compensated passively using silicon dioxide.

Chapter 1 INTRODUCTION TO RESONATORS AND FREQUENCY REFERENCES

1.1 Background and Motivation

Time and by extension frequency have been measured with the most precision of all the physical quantities of interest. It is therefore not surprising that almost every branch of physics relies heavily on the measurement of time [1]. In an electrical circuit, the measurement of time can be achieved using an oscillator to generate a fixed frequency output, the period of which provides a measurement of the time interval. Two primary components of an oscillator include a frequency selecting device called a resonator and an amplifier that provides sufficient gain in the circuit. Figure 1-1 shows a block diagram of a simple oscillator circuit. Small and low-power oscillators find numerous applications in today's technology age, the most important of which is time keeping. Wireless communications, high-speed digital electronics, radars, navigation units, *etc*. all use an oscillator for time synchronization [1]. While quartz-based oscillators have served the industry for decades, the difficulty in micromachining quartz and the limited temperature range at which some quartz cuts are stable are the main drivers for researchers who strive for finding a suitable replacement for quartz, specifically for low-cost and miniature timing units [2], [3], [4]. Silicon microelectromechanical system (MEMS) based resonators have been the main candidate for quartz crystal replacement and resonators made of silicon have been successfully commercialized for certain industrial applications [5], [6], [7].

Phase noise of an oscillator is an important metric that sets the limit on the accuracy of time measurement. This timing uncertainty can be estimated from the oscillator jitter, which has a direct correlation with the oscillator phase noise [8]. The phase noise of a MEMS-based oscillator is largely determined by the performance of the resonator and this relationship can be understood with the help of Leeson's model, presented in Equation 1-1 [9].

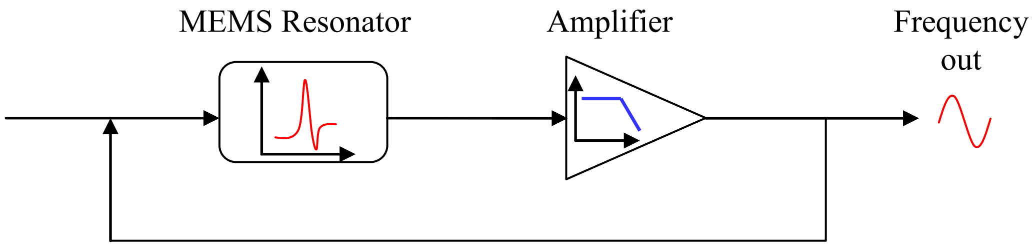

Figure 1-1: Block diagram of a MEMS oscillator.

$$L(\Delta f) = \frac{P_N}{P_{sig}} = \frac{\frac{1}{2} i_N^2}{i_{drive}^2} \left[1 + \left(\frac{f_0}{2Q\Delta f}\right)^2\right], \qquad \text{Equation 1-1}$$

where $L(\Delta f)$ is the oscillator phase noise at a frequency offset of Δf from the oscillator center frequency f_0. Quantity i_N^2 is the input referred noise for the oscillator circuit and i_{drive}^2 is the drive power for the oscillator circuit. From the equation above, we can note that for low oscillator phase noise, the resonator should have a high quality factor (Q), large power handling capability (increased i_{drive}^2), and a low motional impedance (decreased i_N^2) [9].

Given the importance of resonator performance in precision timing references, significant effort has been spent in understanding their performance limitations, its causes and their mitigation strategies.

1.2 Classification of Micromachined Resonators

The resonance of the micro-resonators under consideration is basically the formation of standing elastic waves along the primary geometry of the device. In order to utilize this phenomenon in practical applications, it is important to be able to electrically excite and detect such resonances in real material geometries. As a result, micromachined resonators are most commonly classified based on the transduction mechanism between the electrical and the mechanical domains; most common being electrostatic and piezoelectric. Figure 1-2 shows the classification of micromechanical resonators based on their transduction mechanism. The resonator actuation mechanism determines its performance metrics and thus the actuation mechanism needs to be carefully chosen.

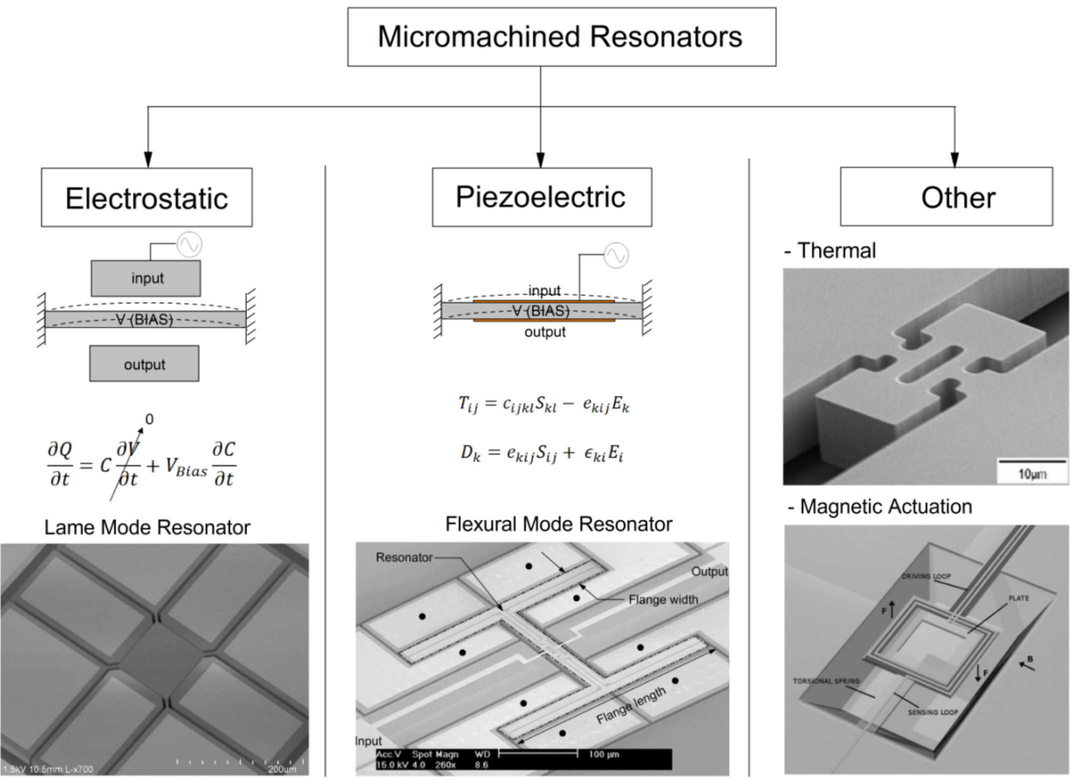

Figure 1-2: Classification of micro-mechanical resonators based on their transduction mechanism**.**

1.2.1 Electrostatic Actuation

Capacitive transduction is one of the first techniques to be employed with microfabricated resonators [10]. Doped silicon is naturally conductive due to which it is fairly straightforward to actuate silicon-based resonators electrostatically. Since the electrodes are physically isolated from the resonator, it is possible to implement electrostatically-actuated resonators with a single material leading to quality factors higher than those achieved by other actuation mechanisms [11]. Figure 1-3 shows a scanning electron microscope (SEM) image and a schematic diagram of an electrostatically-actuated Lamé-mode resonator [12].

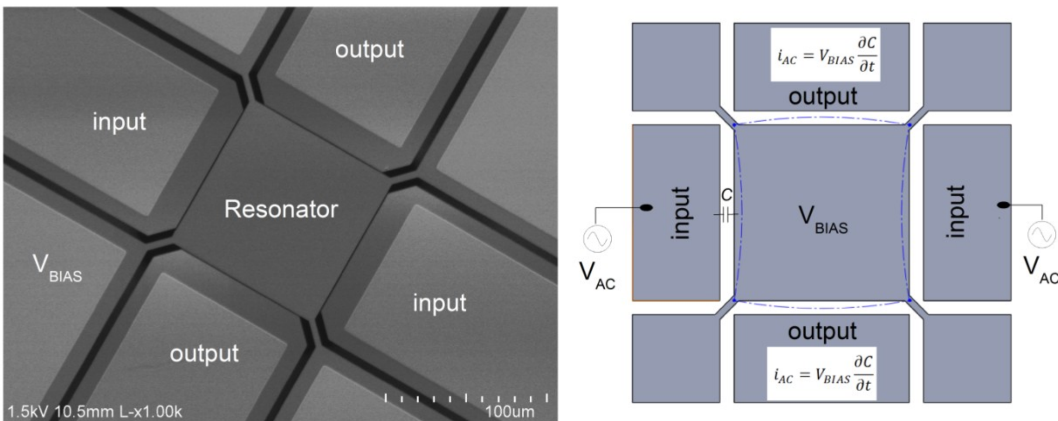

Figure 1-3: (Left) SEM image of an electrostatically-actuated Lamé-mode resonator [12]. (Right) A schematic of the resonator highlighting the important parameters.

The current at the output is determined by the motional impedance (R_m) of the device, which is a function of the applied bias voltage (V_{BIAS}) and the electrostatic gap (d) between the resonator and the electrodes and can be estimated using Equation 1-2 [13].

$$R_m = \frac{k.d^4}{\omega.Q_u.V_{BIAS}^2.\epsilon^2.A^2}, \quad \text{Equation 1-2}$$

where

k *is the dynamic stiffness* $\left[\frac{N}{m}\right]$;

ω *is the angular natural frequency* $\left[\frac{rad}{s}\right]$;

Q_u *is the unloaded quality factor* ;

ϵ *is the dielectric constant of the gap material* $\left[\frac{F}{m}\right]$;

A *is the Area* (μm^2);

The magnitude of the motional impedance determines the insertion loss of the resonator and should be small to achieve low phase noise. From Equation 1-2 it can be seen that the motional impedance can be decreased by reducing the actuation gap. A high aspect ratio combined poly and single crystal silicon (HARPSS) process has been used quite successfully in achieving sub-micron actuation gaps, thereby significantly reducing the motional impedance and the DC bias requirement of the resonators [10]. However, the reduced actuation gap significantly degrades the power handling of the resonator due to (a) non-linear capacitance change with large input power and (b) pull-in behavior of a parallel plate capacitor with a moving electrode. Another approach to improve the motional impedance is by replacing the air gap with a dielectric preferably with a large dielectric coefficient such as aluminum oxide (Al_2O_3) or Hafnium dioxide (HFO_2) [14]. For a given device design, the motional impedance varies inversely with the resonator *Q* and as a consequence there has been a strong push towards improving the *Q* of micromachined resonators.

1.2.2 Piezoelectric Actuation

Piezoelectric materials are characterized by their ability to convert an applied mechanical force into an electrical signal or vice versa. When materials with a non-centrosymmetric crystal structure experience deformation under applied stress, they generate a net dipole potential leading to an electrically measureable potential at the output [15]. The basic constitutive equations for piezoelectricity can be written as,

$$T_{ij} = c_{ijkl}S_{kl} - e_{kij}E_k \,, \qquad \text{Equation 1-3}$$

$$D_k = e_{kij}S_{ij} + \epsilon_{ki}E_i \,, \qquad \text{Equation 1-4}$$

where,

T_{ij} *is the mechanical stress tensor* (MPa) ;
c_{ijkl} *are the coefficients of elasticity* ;
S_{kl} *is the strain tensor* ;
e_{kij} *is the piezoelectric stress tensor* ;
E_k *is the electric field tensor* ;
D_k *is the electric displacement vector* ;
ϵ_{ki} *is the dielectric constant tensor* ;

Materials with wurtzite crystal symmetry such as aluminum nitride (AlN), zinc oxide (ZnO), and gallium nitride (GaN) have been successfully used to make microfabricated resonators [16], [17], [18]. In particular, thin films of high quality c-axis oriented polycrystalline AlN can be sputtered at low temperatures and thus these devices can be directly integrated with CMOS [19]. The most successful device made from thin-film piezoelectric AlN is the film bulk acoustic resonator (FBAR). Avago has successfully commercialized AlN-based FBARs for making duplexers and filters used in the RF front-end of a wireless radios (cellular phones) [20].

Figure 1-4 shows a SEM image and a schematic of a flexural-mode resonator actuated piezoelectrically [17]. In case of piezoelectric resonators, the choice of electrode placement determines the primary mode of resonance. The schematic in Figure 1-4 (right) shows the electrode placement required for exciting the in-plane flexural mode of the resonator.

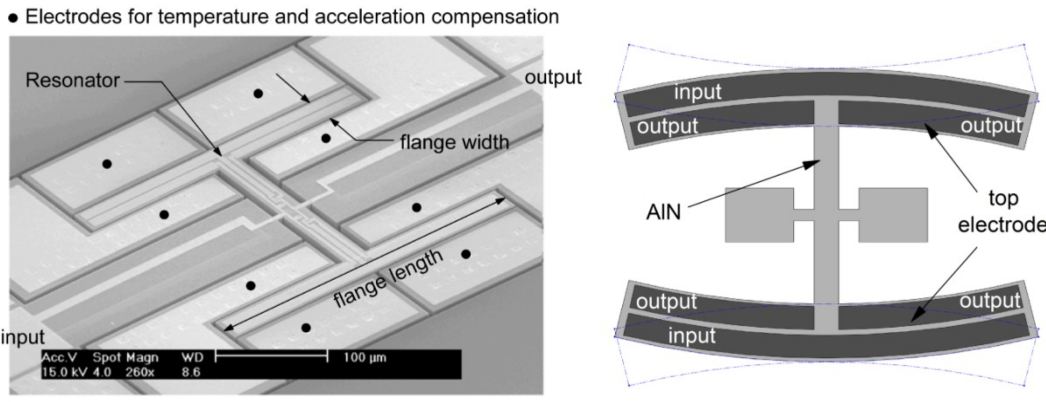

Figure 1-4 : (Left) A SEM image of a piezoelectrically actuated AlN-on-silicon flexural-mode resonator. (Right) A schematic of the resonator highlighting the top electrode layout designed to excite the in-plane flexural mode piezoelectrically.

In general, piezoelectric resonators show a lower motional impedance as compared to their electrostatic counterparts and the motional impedance is a strong function of the strain in the material under the actuation electrodes. Since piezoelectric actuation relies on strain rather than displacement, they usually show excellent power handling capability, limited by the energy density of the piezoelectric layer. Through a careful control of the device geometry excellent power handling with low motional impedance can be obtained [21].

1.2.3 Other Actuation Mechanisms

While most researchers have focused on the above two actuation mechanisms, any means of converting an electrical signal into physical motion can be used to excite mechanical resonance. Magnetomotive force can be used to excite a resonance in suitable materials and/or alloy compositions [22]. Similarly, in resistive materials such as doped silicon, applying a pulsating current leads to alternate thermal expansion and contraction which can be used to excite mechanical resonance in suitable geometries [23]. In most cases, the use of such non-standard excitation techniques is only utilized to achieve specific environmental or application requirements.

1.3 Loss Mechanisms in Mechanical Resonators

An elastic wave propagating in a material experiences a loss in its total energy which is a function of (a) the distance traversed by the wave and (b) the material in which the wave is propagating. Mathematically, the coefficient of attenuation (α) is used to describe this behavior. This attenuation is most conveniently measured through the measurement of the resonator *Q,* which is one of the most critical parameters for the realization of precision timing references.

The resonator Q can be expressed as the ratio of the peak energy stored in the system to the energy dissipated from the system in one oscillation cycle.

$$Q = 2\pi \frac{peak\ energy\ stored}{energy\ dissipated\ per\ cycle} \qquad \text{Equation 1-5}$$

Practically, it is more useful to define the resonator Q in terms of its frequency and the measured bandwidth of its transfer function as,

$$Q = \frac{resonance\ frequency\ (f_0)}{-3dB\ Bandwidth\ (BW)}. \qquad \text{Equation 1-6}$$

Thus, the resonator Q determines the sharpness of the peak of the transfer function, which also determines the spectral purity of the oscillator built using this resonator. In general, higher Qs are preferred for resonators used in practical applications, which is why a lot of effort has been put towards understanding the fundamental causes of loss in micromachined resonators [24], [25].

Figure 1-5 shows a classification scheme for resonator loss mechanisms based on their source. The intrinsic loss mechanisms are primarily determined by the resonator material and its operating frequency while the extrinsic loss mechanisms are set by the resonator geometry and its operating environment.

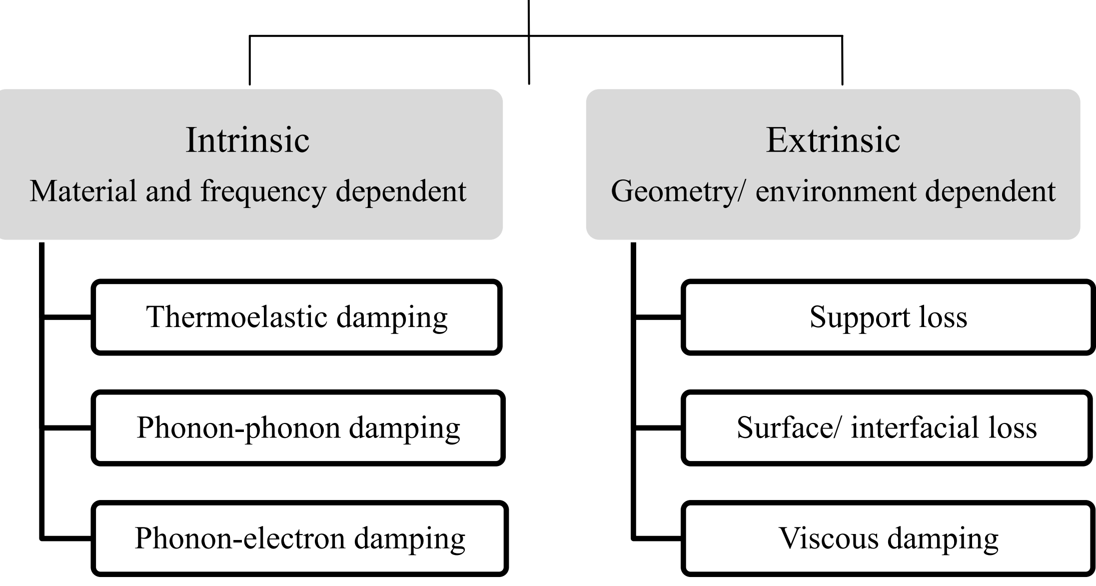

Figure 1-5: Classification of the important loss mechanisms in resonators.

The total resonator Q is determined by the addition of all the individual loss factors. In terms of the individual Qs, we can write,

$$\frac{1}{Q_{total}} = \frac{1}{Q_{intrinsic}} + \frac{1}{Q_{extrinsic}} \qquad \text{Equation 1-7}$$

The intrinsic energy dissipation mechanisms limiting the Q of acoustic resonators consist of thermoelastic, phonon-electron, and phonon-phonon interactions.

$$\frac{1}{Q_{intrinsic}} = \frac{1}{Q_{TED}} + \frac{1}{Q_{phonon-phonon}} + \frac{1}{Q_{phonon-electron}} \qquad \text{Equation 1-8}$$

Amongst these, phonon-phonon dissipation is the dominant loss mechanism in most materials used for MEMS resonators (such as Si and AlN) and thus sets the upper limit on the maximum attainable Q of the resonator. Thermoelastic damping is most prominent at lower frequencies where the temperature gradient due to stress

variations across the resonator can cause an irreversible heat transfer. The stress variations within the resonator are a direct consequence of the mode shape and thus thermoelastic damping shows a strong modal dependency. This implies that for a certain choice of modes (*e.g.*, shear modes), if the stress gradient is small, then thermoelastic damping is also correspondingly small [25].

At higher frequencies, the Akhieser loss mechanism is considered to be the dominant loss factor. In the Akhieser model, the acoustic energy is assumed to be propagating via a slowly varying strain field, *i.e.*, the acoustic energy is assumed to be a wave propagating through a sea of thermal phonons [26]. During this propagation, the acoustic wave loses a part of its energy to the thermal phonons and the nature of the interaction is such that the resonator $f \times Q$ product remains constant for a given material [24]. As this loss mechanism is the dominant loss mechanism across a large resonator operating frequency range (few tens of MHz up to a few GHz), the $f \times Q$ product is used as a figure of merit to compare different resonator topologies. At frequencies higher than the inverse of the phonon relaxation time (exact frequency depends on the resonator material but usually occurs in the GHz range), Akhieser model is no longer valid and we have to use a quantum mechanics approach as proposed by Landau and Rumer [27]. In this model, the energy loss is assumed to originate from collisions between the acoustic and thermal phonons due to the anharmonicity of the crystal. Mathematically, in the Landau-Rumer regime, the $f \times Q$ of the resonator is a function of frequency and thus it is predicted that high-frequency resonators (more than a few GHz for silicon) would not suffer from lower resonator Q as the operating frequency is increased [24].

Estimation of the intrinsic losses in a material determines the theoretical maximum *Q* that a resonator can achieve. However, in reality it is found that the limiting loss mechanisms are usually extrinsic in nature [11], [24]. Fluid damping or viscous damping is one of the most prominent loss mechanisms observed in low-frequency devices operated at standard temperature and pressure conditions. By operating the resonator in a vacuum environment or through hermetic packaging, this loss can be significantly reduced [28].

Support and interface losses are much harder to estimate and therefore pose a significant design challenge. Support loss in resonators is caused primarily due to the energy lost through the supporting tethers which connect the resonator to the substrate. In general, this anchor induced loss can be minimized by placing the tethers at the nodal points of the resonance mode. This significantly reduces the energy lost through the tethers and helps improve the resonator *Q* [29]. The mechanism for surface and interface loss due to stress gradients has received some attention in recent years [30], [31]. There has been some effort on analytical modeling of interface loss motivated by the recent developments in piezoelectric resonators which require a multi-layer stack.

Improved simulation tools are critical to design for high *Q* resonators useful in timing applications. While the appropriate choice of material can provide higher intrinsic device *Q*, advanced modeling techniques such as finite element analysis (FEA) can allow for designing resonator with low extrinsic loss factors, thereby enabling high-*Q* micromachined resonators [32].

1.4 Temperature Compensation of Micromachined Resonators

Most materials used in MEMS exhibit a fairly large temperature coefficient of elasticity (TCE) in addition to a coefficient of thermal expansion, which leads to a significant temperature induced change in the frequency of a resonator. Moderately doped silicon resonators demonstrate a temperature coefficient of frequency (TCF) of -30 ppm/°C at room temperature [33]. This implies that clocks made from silicon resonators will demonstrate a considerable temperature induced timing error. In order to overcome this difficulty, different solutions have been proposed to either compensate for or eliminate the TCE of silicon.

Passive compensation of silicon resonators is usually implemented by creating a silicon and silicon dioxide (SiO_2) composite resonator. Silicon dioxide has a positive TCE of +180 ppm/°C and thus a composite structure can completely cancel the first-order term of the resonator TCF, resulting in a second-order temperature dependence of frequency [33], [34].

More recently, there has been some investigation on the variation of TCE of silicon as a function of its doping levels with some success [35]. The variation of TCE of single crystal silicon as a function of orientation has also been investigated motivated by a similar feature in quartz [36].

1.5 Temperature stable precision timing references

Given their strengths and limitations, a number of approaches have been utilized to enable silicon-based timing references for a variety of applications [5], [6], [7]. While passive compensation technique has the benefit of lower power consumption and simple oscillator circuit design, the relatively large temperature induced frequency shift (~ 100 ppm across the industrial temperature range) is still not small enough to satisfy requirements of the state of the art communication applications. As a consequence active compensation strategies have been employed most commonly through the use of an on-chip temperature sensor to improve the temperature stability of silicon based resonators [9]. However, this approach is strongly limited by the performance of the temperature sensor and the thermal coupling between the resonator and the sensor.

This thesis describes a novel system that utilizes multiple temperature-compensated resonators to achieve sub-ppm temperature stability across a wide temperature range [37]. Figure 1-6 shows a block diagram of the proposed system and identifies the critical components necessary. A minimum of three temperature compensated resonators with unique turnover temperatures are essential to generate the required frequency output. Turnover temperature is defined as inflection point of the parabolic dependence of resonator frequency on temperature. The frequency signals from the three oscillators undergo frequency multiplication and mixing in two stages. In the first stage the first-order temperature dependence is eliminated and thus at its output we have a pure second-order temperature dependence. This temperature dependence is eliminated in the second stage, thereby giving a temperature-stable output.

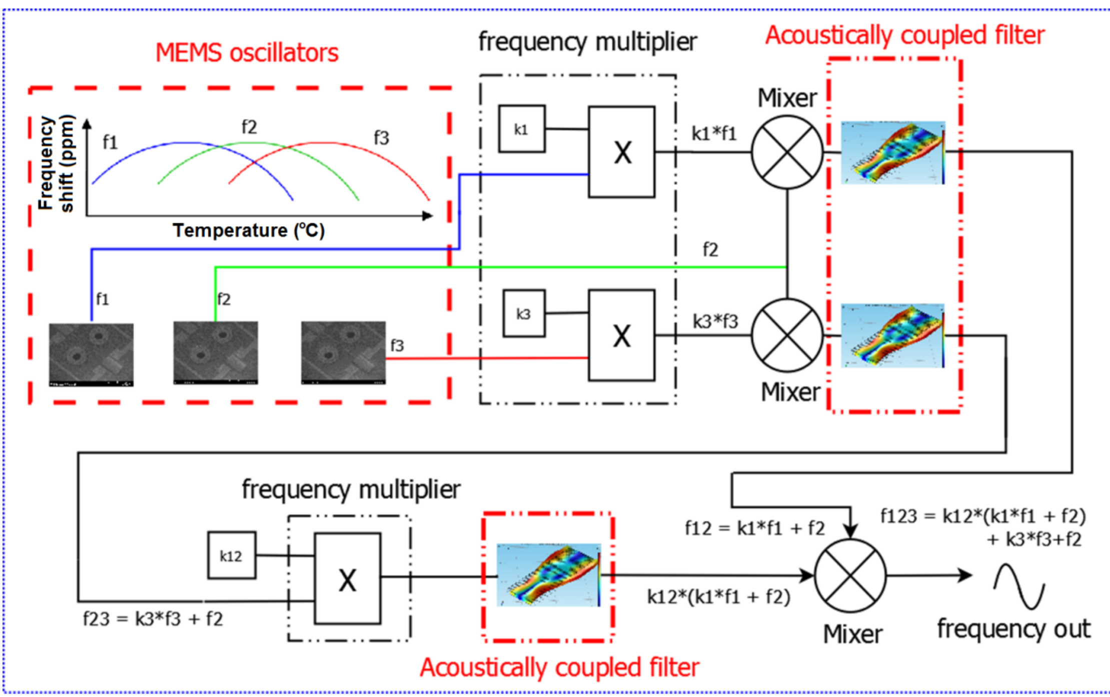

Figure 1-6: Block diagram of the proposed multi-resonator temperature stable frequency reference.

A mixer being a highly non-linear device requires a bandpass filter at its output to eliminate the unwanted frequency products. Acoustically coupled bandpass filters are proposed to achieve this filtering function due to their low insertion loss, small bandwidth, sharp filter skirt angles, and the ability to co-integrate them with the temperature compensated resonators [38].

1.6 Research Objectives

The goal of this work is to achieve sub-ppm temperature stability across a wide temperature range using a new system architecture utilizing multiple temperature-compensated silicon MEMS resonators. The implementation of the proposed multi-resonator clock will require multiple resonators with different turnover temperatures. As a result, this thesis first addresses the challenge of obtaining such multi-compensated resonators in a single die. The passive compensation mechanism of silicon resonators is carefully analyzed and a novel temperature compensation strategy employing silicon dioxide in areas of high strain is proposed to enable high-*Q* temperature compensated resonators. Further the effect of location of silicon dioxide within the resonator volume is studied and multiple turnover temperatures within the same process flow are experimentally demonstrated [17], [37], [39].

As has been discussed previously, the resonator *Q,* its motional impedance, and power handling capability are critical parameters that determine the accuracy of the timing reference. Piezoelectric actuation has been chosen here to obtain low motional impedance and a large power handling capability. While the intrinsic resonator loss mechanisms are set through the choice of materials, minimizing anchor loss is critical to enable a high device *Q*. As a result, this thesis further investigates the modeling of anchor loss to optimize the resonator support design [12]. More importantly, by applying this analysis to the temperature compensated resonators, the effect of silicon dioxide on the resonator *Q* is shown to be largely mitigated. Specifically, a temperature compensated flexural-mode resonator is demonstrated with a measured *Q* of 20,000 at 1.37 MHz, limited by the fundamental thermoelastic

damping in the material. Through optimized design of the resonator supporting tethers, the compensated device has a small *Q* degradation as compared with the uncompensated device which demonstrated a *Q* of 25,000 [17].

While the flexural-mode resonators have a relatively large *Q* and achieved the required temperature compensation, their motional impedance is quite high owing to the shear mode of operation. To overcome this limitation, piezoelectrically-actuated breathing-mode ring resonators were designed with different turnover temperatures on the same die. These resonators show a low motional impedance between 300 to 600 Ω with a large power handling limit of more than +5 dBm. The compensated resonators exhibit measured *Q* of 6,000 at 19 MHz as compared to the uncompensated ring resonator which demonstrated a *Q* of 9,000 at 21 MHz, implying that the presence of silicon dioxide is not the primary cause of the lower *Q* [37]. The presence of the piezoelectric stack over the resonator points towards interface losses degrading the resonator *Q*. A careful experiment utilizing Lamé-mode resonators, known to provide very high $f \times Q$ products, is implemented to further study this loss mechanism. Electrostatically-actuated Lamé-mode resonators operating at 41.5 MHz are implemented as a reference. These resonators demonstrate a very high *Q* of 300,000 giving an $f \times Q$ of 1.25×10^{13}, one of the highest reported to date for silicon [12]. Using these resonators the anchor loss model is verified through a comparison of measured *Q* as a function of tether geometry [12]. Subsequently, electrostatically actuated temperature-compensated Lamé-mode resonators are fabricated to study the effect of silicon dioxide on the performance of the resonator. Optimized electrostatic devices reveal a *Q* between 60,000 to 100,000 at 36 MHz for the compensated Lamé-

mode resonators. To understand the effect of vertical interface namely the silicon-piezoelectric-metal stack, temperature-compensated piezoelectrically actuated Lamé-mode resonators are fabricated. While the symmetric nature of the Lamé-mode is unsuitable for piezoelectric actuation, it is shown that using the oxide islands within the resonator, this mode can be reliably actuated. These devices measured a Q between 20,000 to 30,000 at 36 MHz (as opposed to 60,000 to 100,000 for electrostatic resonators), suggesting that the piezoelectric stack leads to a large Q degradation through the mechanism of interface loss [39].

The same AlN-on-silicon stack can be used to build integrated low-loss bandpass filters along with the temperature-compensated resonators. A 2.8 GHz bandpass filter with an insertion loss of 2.4 dB is experimentally demonstrated and analyzed [38], [40]. Using analytical models, the results of the FEM analysis are explained and it is shown that low-loss filters with bandwidth up to 1% of the center frequency can be designed across a wide frequency range [40].

These results are utilized in the design of a low frequency bandpass filter at 21 MHz suitable for use in the multi-resonator clock. This filter shows a measured bandwidth of 4 KHz and is suitable for use in the proposed clock system to clean up the mixer output. While there have been reports of thickness-mode acoustically coupled filters in literature, this design utilizes the contour or in-plane mode of device operation. As a result, multiple filters with varying frequencies and passband characteristics can be designed on the same wafer, catering to the requirements of the proposed clock system.

In summary, the important contributions of this thesis work are

- Development of an algorithm to enable temperature-stable timing references across a wide temperature range. Using this algorithm, a clock is demonstrated with a total frequency shift of ±4 ppm across -20 °C to +50 °C.
- Demonstration of a passive compensation scheme that allows for temperature compensation of MEMS resonators with minimum Q degradation.
- Demonstration of temperature-compensated resonators with control over the turnover temperature through placement of silicon dioxide temperature-compensating islands in the resonator.
- Analysis of anchor loss in bulk acoustic wave resonators and demonstration of a piezoelectrically actuated and temperature-compensated Lamé-mode resonator showing record high Q.
- Detailed analysis and the development of design guidelines of acoustically coupled filters for applications in modern communication systems.
- Design and experimental verification of in-plane acoustically coupled filters for use in the multi-resonator clock.

1.7 Organization of Thesis

In Chapter 1 we discussed the resonator requirements for precision timing references. We described the two primary resonator actuation techniques and justified our choice of piezoelectric actuation through a detailed comparison with electrostatic actuation. A novel multi-resonator clock is proposed and the objectives of this research are presented in the context of implementing this system. Chapter 2 describes the implementation details of the temperature-compensated flexural and ring resonators. Chapter 3 describes the oscillator implementation for use in the proposed multi-resonator clock. A detailed analysis of the clock algorithm is presented highlighting the system advantages and limitations. Through the use of discrete components, a proof of concept implementation of the full system is demonstrated. Chapter 4 describes the Lamé-mode design and measurement results used to analyze the effect of the proposed temperature compensation technique as well as the effect of interface losses induced from the piezoelectric stack on the resonator Q. In Chapter 5 we introduce the acoustically coupled filters, present a detailed analysis of their working principle and show their applicability to signal filtering in a large frequency range from a few MHz all the way up to a few GHz. Finally this thesis is concluded in Chapter 6 with a brief discussion on the future research directions.

Chapter 2 TEMPERATURE COMPENSATION AND PIEZOELECTRIC ACTUATION OF SILICON RESONATORS

Precision timing references benefit from the large power handling of piezoelectrically actuated resonators. As was discussed in Chapter 1, by increasing the drive current, the circuit noise and thus the oscillator noise floor can be significantly reduced. This chapter describes our efforts on implementing piezoelectrically-actuated silicon resonators suitable for use in the multi-resonator clock system briefly described in Chapter 1 Section 1.5.

The ability to deposit high-quality thin-film AlN at post-CMOS compatible temperatures can be utilized to realize high-Q AlN-on-silicon resonators for applications in timing references. The AlN-on-silicon platform benefits from the low acoustic loss in silicon thereby enabling high Qs [24], [25] and eliminates the large motional impedance and power handling limitation of electrostatic actuation [21]. In order to utilize the AlN-on-silicon resonator in a stable oscillator, it is necessary to compensate for the relatively large TCF of AlN and silicon.

A commonly used scheme for temperature compensation is the use of a material with a TCF opposite to that of the main resonating material. For example, using a thermally grown oxide coating, which has a positive TCF, a silicon resonator (with a negative TCF) has been demonstrated with frequency variation of less than 200 ppm over a wide temperature range [33]. In this implementation, the oxide was coated on the surface of the resonator, which is disadvantageous considering that

dielectric charging can cause significant frequency instability [41]. An alternative strategy involves replacing the surface oxide with uniformly distributed oxide pillars or trenches through the resonator volume [34]. Through detailed FEA and experimental demonstration, we show that such a strategy is inherently inefficient and leads to an unnecessary loading of the resonator *Q*. We hypothesize that the position of the oxide-refilled regions is critical and plays an important role in the efficient compensation of silicon resonators. By placing the silicon dioxide within the resonator body in areas of high strain energy, maximum temperature compensation can be achieved with minimum oxide volume, thereby leading to a minimum degradation of the resonator *Q*.

2.1 Flexural Mode Resonators

In the low frequency range, two types of flexural-mode resonators with good performance characteristics have been successfully implemented in literature: the double ended tuning fork (DETF) [33] and the I-shaped bulk acoustic resonator (I-BAR) [13]. The main distinction between the two lies in the location of their support tethers. While both these implementations have been using electrostatic actuation, we choose to utilize the piezoelectric actuation of the flexural mode for improved power handling capability. Figure 2-1 shows the schematic of a piezoelectrically-actuated AlN-on-silicon flexural-mode resonator. This resonator is designed in the I-BAR configuration [13] composed of a central rod holding the resonating flanges and anchored to the substrate through small tethers. This device configuration with two connector rods and using electrostatic actuation has been proven to provide high-Q resonators with a large electrostatic tuning range [13]. The choice of using a single connector rod was made so as to allow for a simpler electrode layout required for piezoelectric actuation. The resonator is designed for operation in the first-order flexural mode for which the resonance frequency can be approximated as,

$$f \cong 0.646 \frac{w}{L^2} \sqrt{\frac{E}{\rho}} \ , \qquad \text{Equation 2-1}$$

where w is the width of the resonator flange, L is length of resonator flange, E and ρ are the effective Young's modulus and density of the resonator stack, respectively.

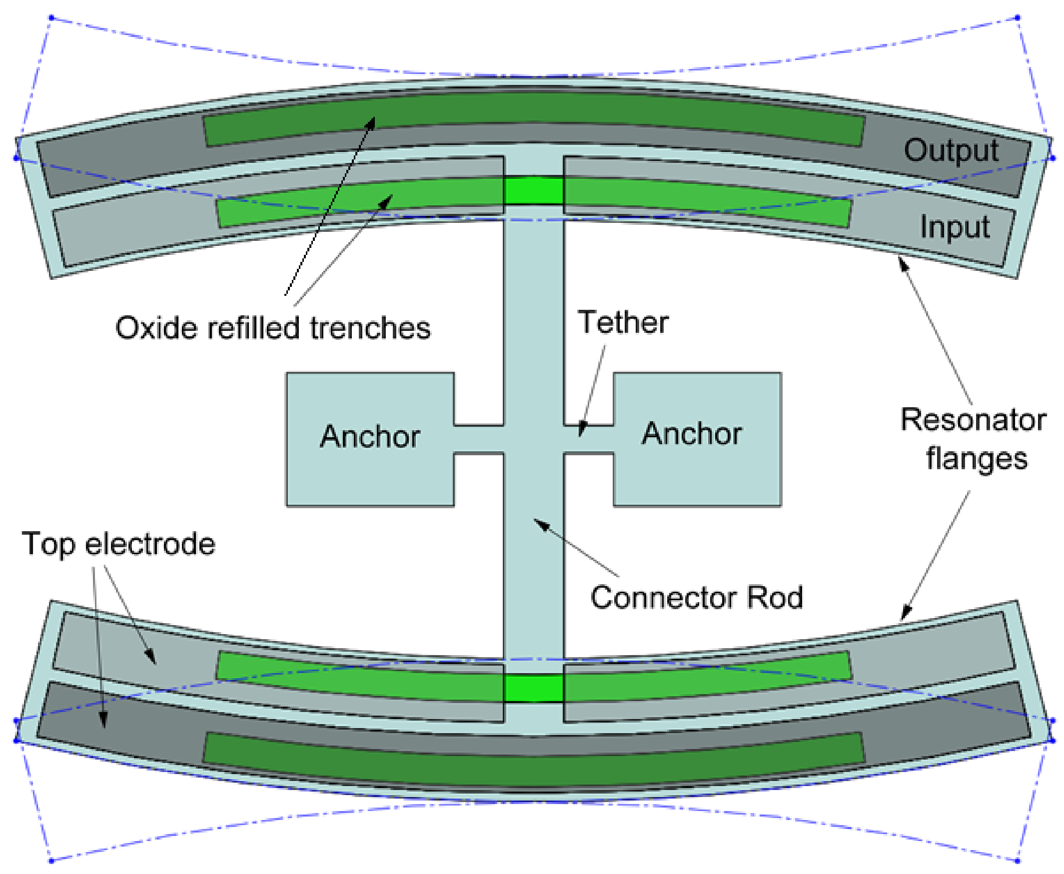

Figure 2-1: A schematic view of the AlN-on-silicon resonator, showing the flexural mode of operation. The tuning electrodes are not shown in this schematic.

2.1.1 Position dependence of passive compensation

In order to achieve temperature compensation of flexural-mode silicon resonators, we create a composite resonator having silicon and silicon dioxide with the goal of nullifying the TCE of silicon. In order to improve the efficiency of compensation, we hypothesize that the location of oxide-refilled trenches should be in regions that experience high strain energy during resonance.

Figure 2-2 (a) plots the mode shape of the first-order flexural resonance mode. Figure 2-2 (b) and Figure 2-2 (c) plot the distribution of strain energy across the cross section A-A' as marked in Figure 2-2 (a). From these simulation results, we can find

areas of high strain for the mode of interest. As shown in Figure 2-2, these regions are near the device edges in case of flexural modes. By placing oxide-refilled trenches close to the resonator edge, where strain energy is high, efficient temperature compensation can be achieved.

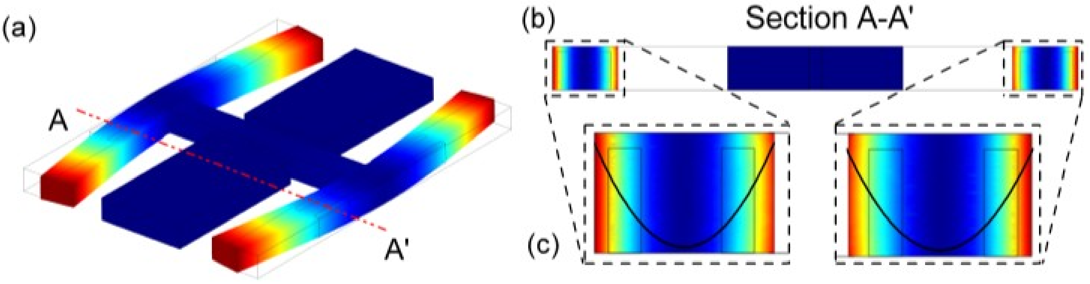

Figure 2-2: (a) Simulated mode shape and (b) simulated strain energy density along section A-A'. (c) A close-up view of the strain energy density variation across the resonator flange cross-section. The overlaid parabolic curve (in black) represents the variation of the strain across the width of the resonator flange. The color spectrum in (a) plots the total displacement and in (b) and (c) plots the strain energy density.

To verify our hypothesis, simulations were performed with a specific oxide-refilled trench size but located at different regions across the resonator flange width with the goal of estimating the temperature coefficient of frequency (TCF) in each case. Figure 2-3 shows the location of four trench pairs used in this study. These trench pairs are located at an offset of 2 µm, 4.5 µm, 7 µm, and 9.5 µm from the resonator edge respectively. In all cases, the total width of the trenches is kept to be 5.5 µm implying that the volume of oxide remains the same. Given the four trench pair combinations, the TCF of the composite resonator is simulated and the results are summarized in Table 2-1.

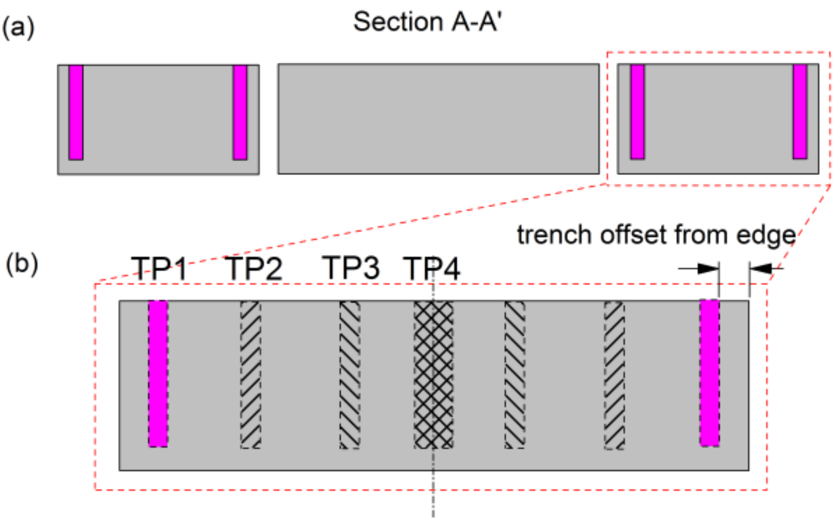

Figure 2-3: Location of oxide-refilled trenches within the resonator (not to scale). Trenches with similar hatch/fill patterns form a trench pair. The section A-A' corresponds to that seen in Figure 2-2.

Table 2-1**:** Simulated resonator TCF at 25 °C for the four different trench configurations

Trench configuration	Total width of oxide (μm)	Trench offset from resonator edge (μm)	Simulated TCF (ppm/K)
TP1	5.5	2	+4
TP2	5.5	4.5	-12
TP3	5.5	7	-21
TP4	5.5	9.5	-26
No Trench	0	-	-30

Figure 2-4 plots the simulated strain energy density across the resonator flange width and the TCF as a function of trench offset from the resonator edge. The simulated strain energy density across the resonator width is plotted on the left y-axis (red curve) of Figure 2-4. The simulated TCF of the resonator as a function of the trench location is plotted on the right y-axis (blue curve). The physical location of

oxide-refilled trenches within the device is noted on the x-axis, which represents the flange width from its edge to center.

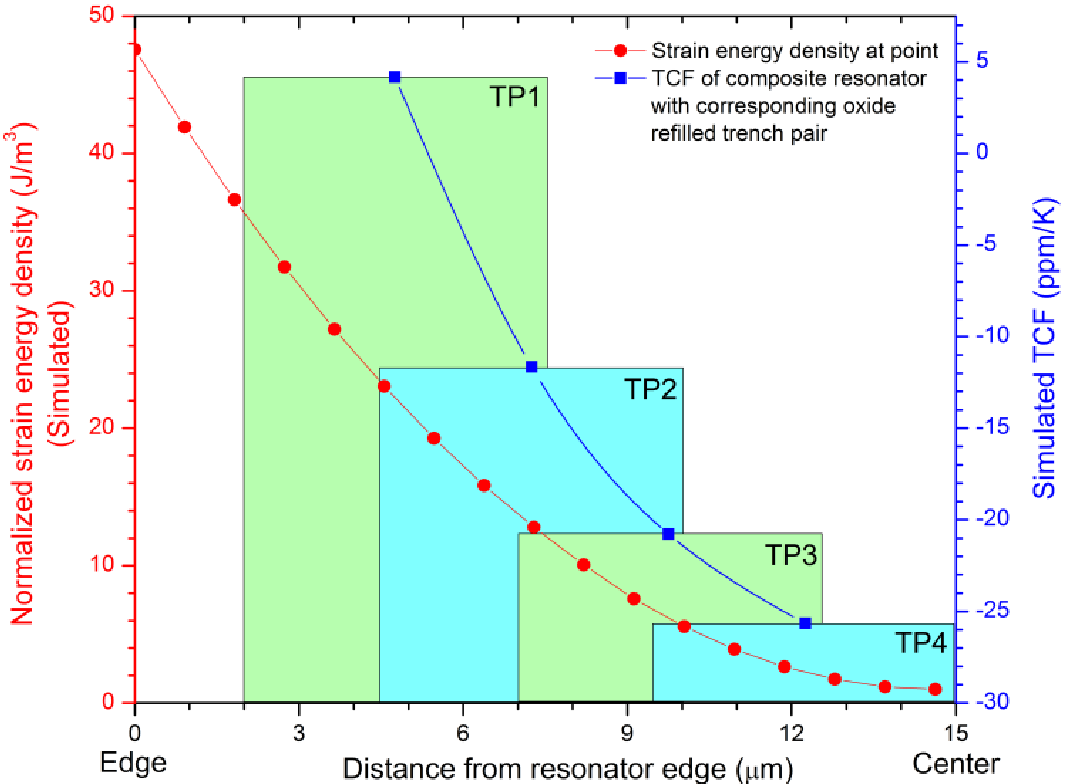

Figure 2-4: Plot showing the variation in strain energy density (normalized) across the width of the resonator. Only one half of the flange width is shown here. The TCF of the composite resonator is plotted as a function of the trench location. A clear correlation between the strain energy across the trench and the resonator TCF can be observed. In all cases, the width of the oxide trenches is 5.5 μm and the total volume of oxide is the same.

As noted earlier, the volume of the compensation material (silicon dioxide) taken in each simulation is the same. The height of the trenches in Figure 2-4 correlates to the simulated TCF while its width correlates with the physical location of the trench within the resonator. The material properties used in the TCF simulations are summarized in Table 2-2. From the results in Figure 2-4, a strong

correlation between the strain energy within the oxide-refilled trench area and the compensated TCF of the resonator can be observed, thus verifying the original hypothesis.

Table 2-2: Material properties used in TCF simulations (all values are at 25 °C).

	E (GPa)	TCE (ppm/K)	∝ (ppm/K)
Silicon	169	-64	2.6
Silicon dioxide	71	187.5	0.5

2.1.2 Experimental Verification

Based on the optimization results, the four configurations shown in Figure 2-5 have been experimentally investigated in this work.

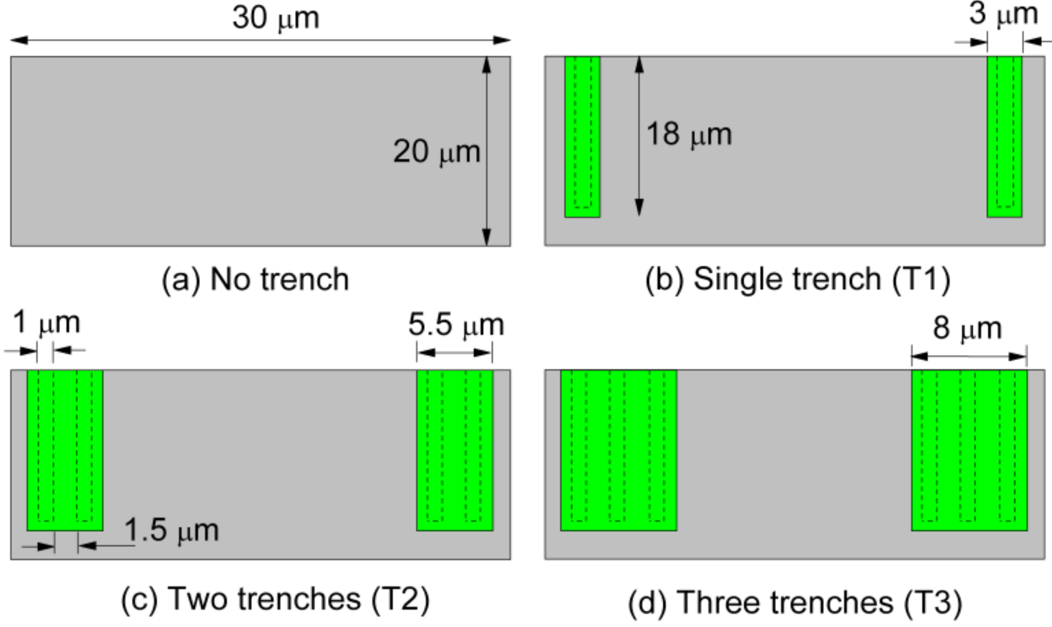

Figure 2-5: Different trench configurations used in the experimental verification of passive temperature compensation. All trenches have the same dimensions and are shown with dotted lines. The spacing between the two etched trenches is kept as 1.5 μm (as marked) in order to ensure that the trenches are fully refilled with thermal oxide.

While all configurations have the trenches at the same distance from the resonator edge, they have different oxide-refilled trench widths, and thus they are expected to result in different TCF values. Table 2-3 summarizes the simulated TCF values for the four configurations in Figure 2-5. For the three-trench configuration, the total strain energy in the trenches is ~ 35% of the total energy of the mode, while its volume is less than 10 % of that of the whole resonator.

Table 2-3: Simulated TCF at 25 °C for the resonator configurations shown in Figure 2-5.

Configuration	TCF (ppm/K)	Configuration	TCF (ppm/K)
No oxide	-30	2 Trenches	-2
1 Trench (T1)	-14.9	3 Trenches	4.3

2.1.3 Fabrication process

The process flow used to fabricate these devices is presented in Figure 2-6. The starting wafer is a 100 mm SOI wafer with a 20 µm thick high resistivity (>1000 Ω.cm) device layer. In the first step, the temperature compensation trenches are etched using deep reactive ion etching (DRIE) (Figure 2-6 (a)). These trenches are subsequently refilled by growing 1.4 µm of thermal silicon dioxide at 1200 °C. It should be noted that the trench depth is kept slightly less than the device layer thickness to ensure that there is silicon separating the buried oxide layer from the oxide-refilled trenches. This feature allows us to etch the buried oxide layer during device release without affecting the oxide refilled trenches. Post oxidation, the wafer surface is polished to a smooth and flat finish using an IPEC-472 chemical mechanical polishing (CMP) tool (Figure 2-6 (b)). A smooth surface is essential for the reactive sputtering of high quality AlN with low stress and vertical c-axis

orientation. After CMP, 100 nm thick Mo is deposited as the bottom electrode. The Mo layer is patterned to reduce eddy currents during AlN sputtering which enables better control of the AlN film stress. A 0.5 μm thick low-stress AlN transduction layer is subsequently deposited in a Tegal AMS SMT^{TM} reactive sputtering system [19]. A 100 nm thick gold (Au) layer is evaporated and lift-off patterned as the top metal. A thin chrome (Cr) layer (10 nm) is used to improve adhesion between Au and AlN (Figure 2-6 (c)). The gap between the resonator and the tuning electrodes is defined by etching the AlN and the silicon device layer using DRIE (Figure 2-6 (d)). Finally, the device is released by selective backside removal of silicon and buried oxide layer (Figure 2-6 (e)). Figure 2-7 shows the SEM images of a fabricated device.

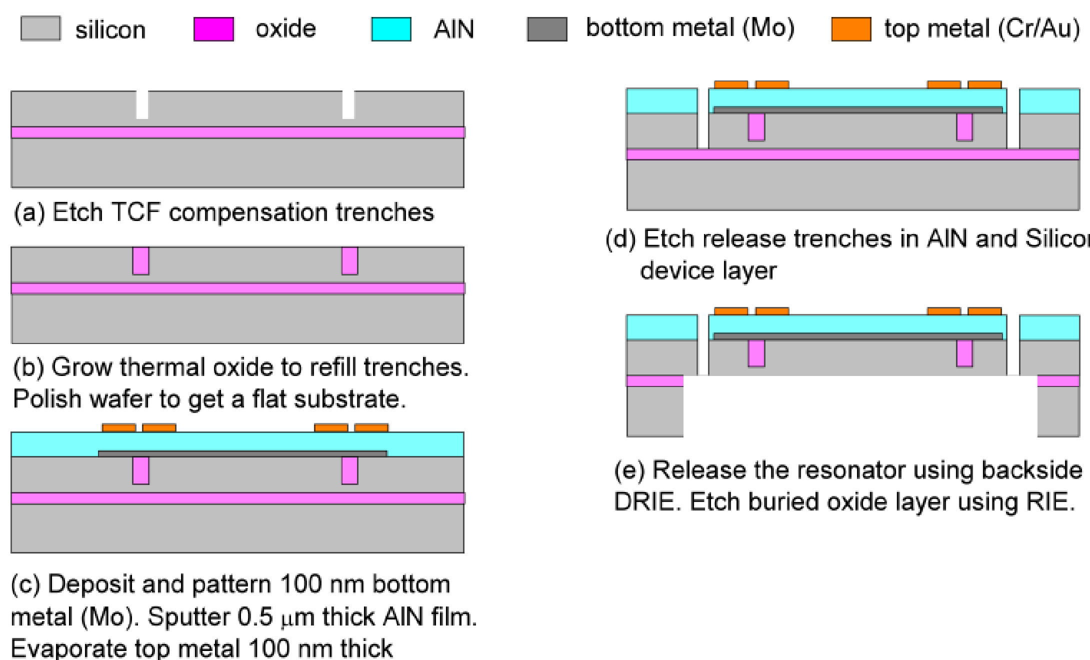

Figure 2-6: Fabrication process flow of the AlN-on-silicon flexural-mode resonators.

● Electrodes for temperature compensation

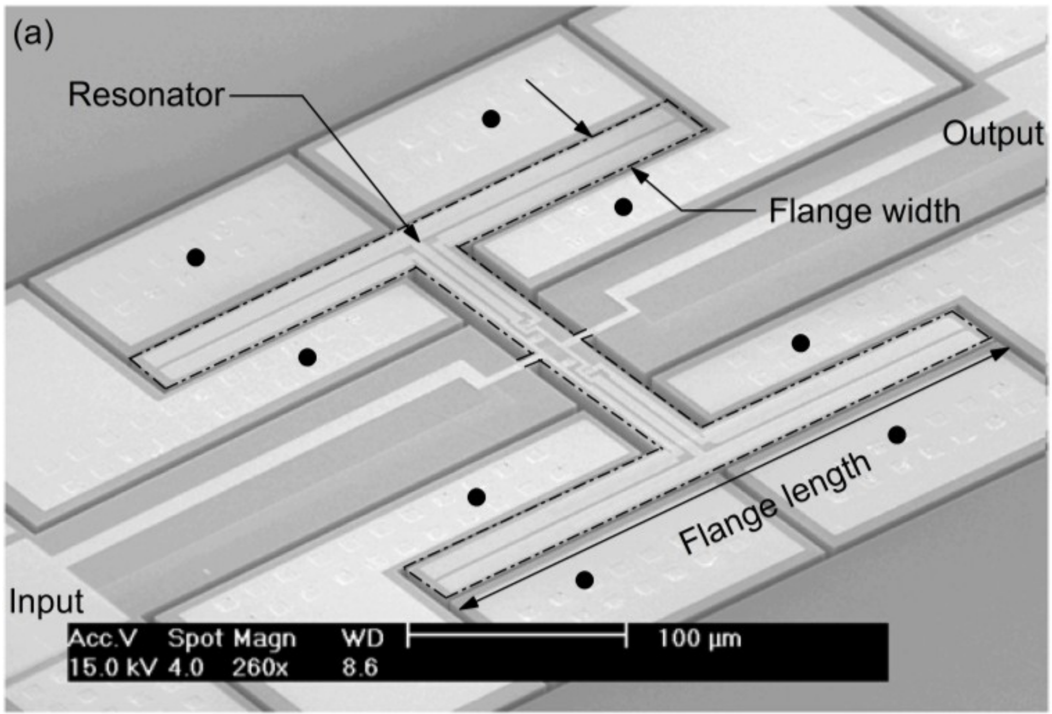

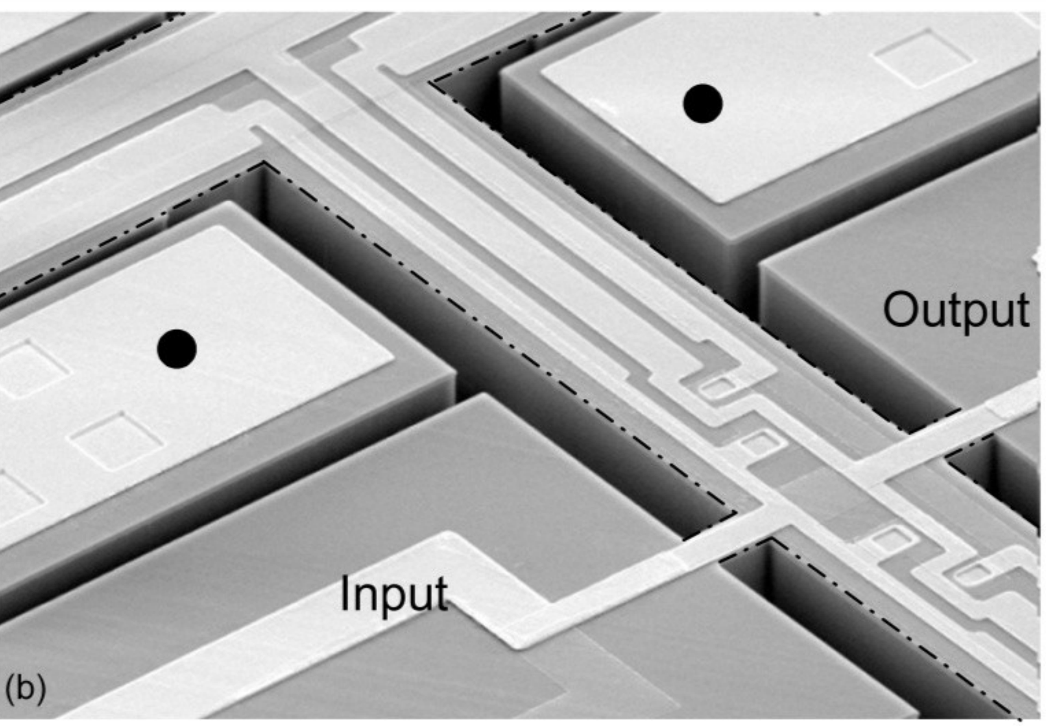

Figure 2-7: (a) An SEM image of a fabricated resonator. There are a total of eight tuning electrodes, which can be used for tuning the center frequency. (b) A close-up view showing the metal routing on the central rod. The black line (dash-dot) marks the outline of the resonating body.

For efficient compensation of the resonator, the trench-refill process is critical. It is important to ensure that the trenches are completely refilled with thermal oxide. Figure 2-8 shows cross-section SEM views of a two trench sample and reveals the quality of the trench refill process. To allow for fabrication tolerances, a 2 µm offset from the resonator edge is maintained in the resonator designs.

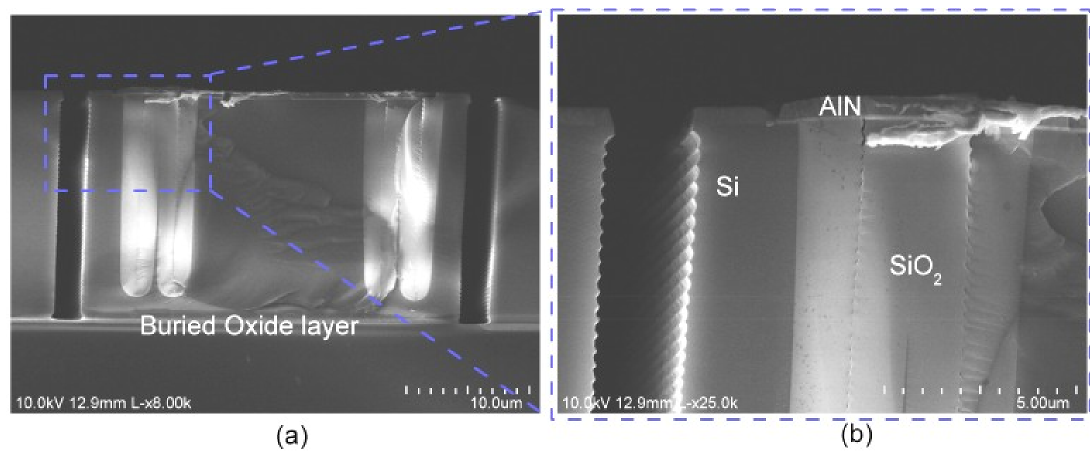

Figure 2-8: Cross-section SEM images showing the oxide-refilled trenches for a two trench sample. The close-up view on the right reveals small air pockets formed during the refill process, which is caused as an effect of scalloping seen during the trench DRIE.

2.1.4 Resonator Design

The device is designed such that the 20 µm thick silicon layer is actuated with only a thin layer of AlN (500 nm). The resonator layout and the AlN thickness is optimized for reduced anchor loss using simulations based on a PML based simulation method [32]. An anchor Q of ~ 180,000 was simulated for the device shown in Figure 2-7. The device dimensions are presented for reference in Table 2-4.

A silicon resonator operating around the frequency of 1.5 MHz is expected to have its Q limited by thermoelastic damping (TED) when operated in vacuum. Q_{TED} is simulated to be ~32,000 for the uncompensated structure using the method outlined

in [42]. Table 2-5 summarizes the contribution of different loss mechanisms on the Q of the resonator.

Table 2-4: Resonator geometry used for the experimental TCF characterization.

Parameter	**Dimension (µm)**	**Parameter**	**Dimension (µm)**
Flange length (L)	320	Tether length (L_t)	7.5
Flange width (w)	30	Tether width (w_t)	6
Rod length (L_R)	180	Si device thickness (t_{Si})	20
Rod width (w_R)	25	AlN thickness (t_{AlN})	0.5

Table 2-5: Contribution of different loss mechanisms on the Q at 25 °C. The simulated Q_{Anchor} for the compensated structure assumes ideal geometry with perfectly rectangular refilled trenches.

	Q_{TED} (simulated)	Q_{Anchor} (simulated)	Q_{Total} (simulated)	Q_{Total} (measured)
No Trench	31,890	180,000	~27,090	25,000
T1	31,915	180,000	~27,110	21,000
T2	31,410	180,000	~26,740	20,000
T3	32,575	180,000	~27,580	19,000

While we expect the inclusion of oxide-refilled trenches to improve Q_{TED} (due to the significantly lower thermal conductivity of oxide [43]), the simulated results in Table 2-5 seem to suggest otherwise. The presence of AlN, which has a high thermal conductivity of 284 $Wm^{-1}K^{-1}$, seems to offset the benefit obtained from the oxide trenches, leading to no net improvement in the simulated Q_{TED}. It should be noted that in these simulations, the effect of fabrication induced geometric variations have been ignored. Nevertheless, the measured and simulated results in Table 2-5 are in excellent agreement suggesting that fabrication induced losses are insignificant compared to thermoelastic damping in the structure.

2.1.5 Measured Results

The fabricated devices are measured using an Agilent E5061B Network Analyzer in an enclosed chamber at a vacuum level of ~ 10 μTorr. Figure 2-9 shows the measured results for devices with different oxide trench sizes shown in Figure 2-5.

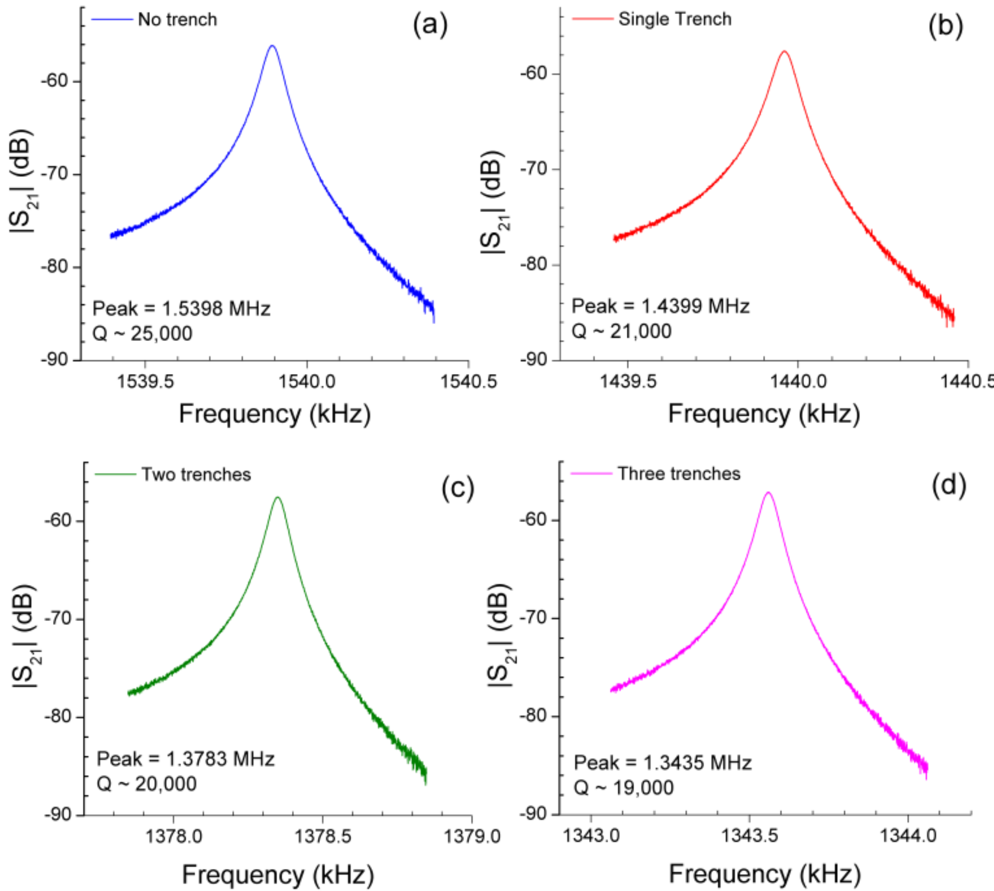

Figure 2-9: Measured response of the resonators with (a) no TCF compensation (b) single oxide-refilled trench (c) two oxide-refilled trenches and (d) three oxide-refilled trenches. All measurements are taken in vacuum and at room temperature.

From the analysis of loss mechanisms, the resonator Q was found to be limited by thermoelastic damping. From the simulated Q_{TED} given in Table 2-5, it was seen that the presence of AlN works to offset any improvement in the Q_{TED} and the device Q remained independent of the number of trenches. However, measured

results show a small Q drop as the number of trenches is increased. From cross-section SEM images (Figure 2-8 (b)), small air pockets can be seen as a consequence of the trench-refill process. The number of lines of air pockets (voids) corresponds to the number of trenches refilled. These voids along with the higher stress in the devices with larger volume of oxide may be responsible for the measured Q degradation. Secondly, any misalignment in the location of the trenches with respect to the resonator edge can also degrade the anchor Q, consequently leading to a reduction in the measured Q. A maximum Q degradation of 24% is measured for the device with three trenches.

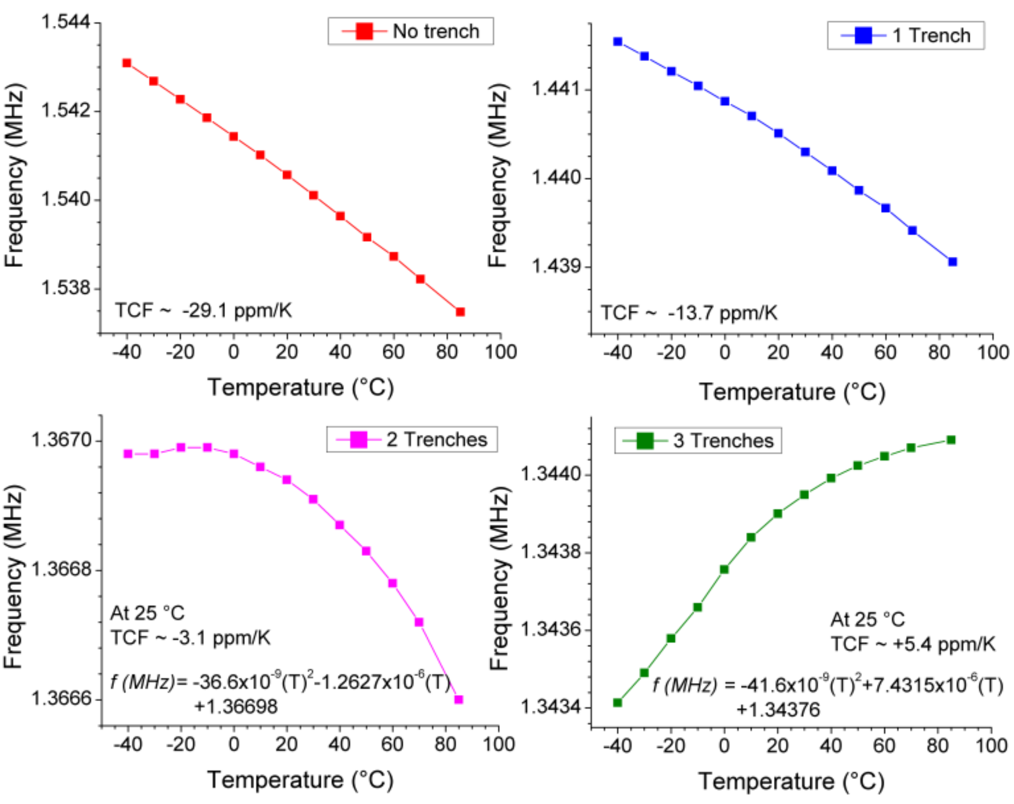

Figure 2-10: Measured resonance frequency as a function of temperature for different trench configurations. In case of no trench and single trench resonators, the TCF value is averaged across the temperature range. For the case of two and three trench devices, the TCF value is estimated at 25 °C.

In order to characterize the temperature dependence of resonance frequency, devices are measured in a Lakeshore cryogenic probe station. The temperature stability of the devices was characterized between -40 °C to +85 °C and the results are shown in Figure 2-10. In order to compare the performance of devices with different trench configurations, their relative frequency shift (in ppm) is plotted as a function of temperature in Figure 2-11. The two- and three-trench configurations show the lowest variation of less than 500 ppm over the temperature range of -40 °C to +85 °C.

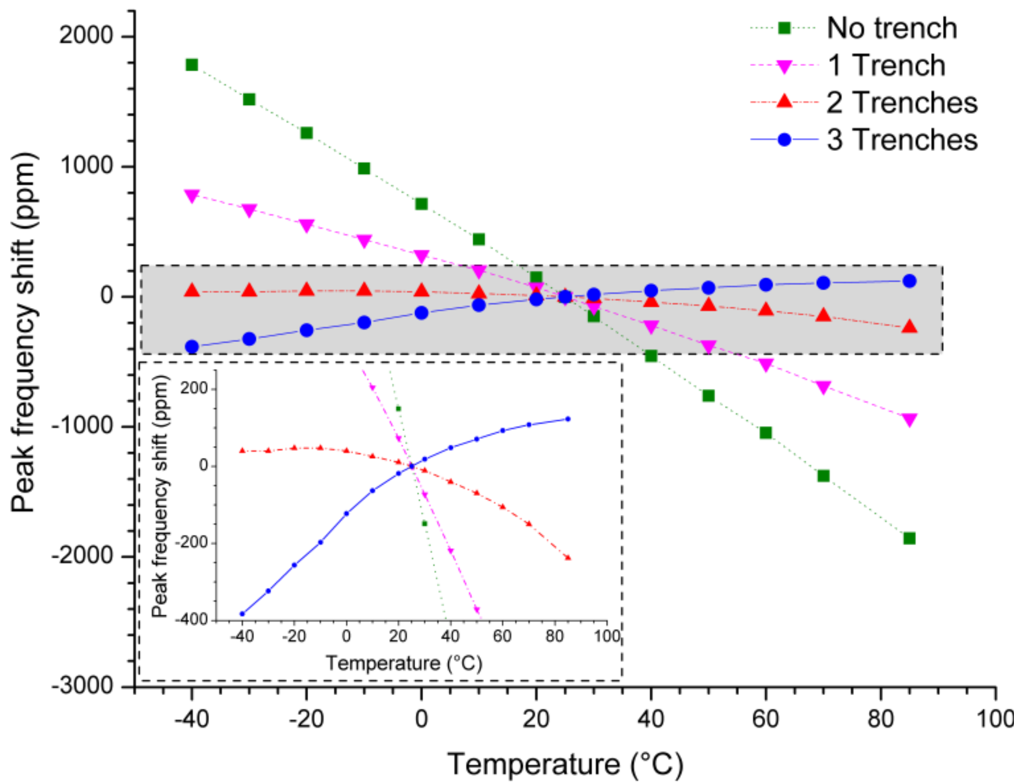

Figure 2-11: Measured peak frequency shift in parts per million (ppm) as a function of temperature for different trench configurations. Inset: measured results in a smaller ppm range.

2.1.6 Active Temperature Compensation

From the measured results of the compensated resonators, it is clear that active compensation is still essential in order to tune out the measured second-order term of the temperature dependence of frequency. More importantly, process variations can shift the center frequency, which may be tuned back using electrostatic or piezoelectric techniques [44]. For fine control over the resonator center frequency, tuning through electrostatic spring softening is a commonly implemented strategy [13] and is used in this work to demonstrate a compensated resonator across the temperature range of +50 °C to +85 °C, near its turnover temperature of ~ 90 °C. As shown in Figure 2-7 (a), the device has eight separate pads for active temperature compensation. Using all available electrodes, a total tuning range of 425 Hz is possible with an applied voltage of 60 V (Figure 2-12). The resonator frequency as a function of applied DC bias can be analytically calculated using [17],

$$f = \frac{1}{2\pi} . \sqrt[2]{\left[\frac{1}{12}\frac{E}{\rho} w^2 . \frac{z_1^4}{l^4} - 2\frac{\epsilon}{\rho} . \frac{1}{w.d^3} . V^2\right]}, \qquad \text{Equation 2-2}$$

from which the expected tuning can be estimated. In Equation 2-2, we have

$E = Effective\ Young's\ modulus\ of\ the\ resonator\ stack\ (Pa)$
$\rho = \ Effective\ density\ of\ the\ resonator\ stack (kg/m^3)$
$w = width\ of\ IBAR\ side\ flange\ (m)$
$L = \ Length\ of\ IBAR\ side\ flange\ (m)$
$gap = electrostatic\ gap\ between\ the\ flanges\ and\ the\ tuning\ electrodes\ (m)$
$t = thickness\ of\ silicon\ device\ layer\ (IBAR\ thickness)(m)$
$\varepsilon = dielectric\ constant\ for\ air\ (F/m)$
$A_e = area\ across\ which\ tuning\ potential\ is\ applied\ (m^2)$
$V = applied\ tuning\ potential\ (V)$

Figure 2-12 plots the measured and analytically estimated resonator frequency as a function of applied DC bias for comparison. The low tuning sensitivity of -0.125 Hz/V^2 extracted from Figure 2-12 can be attributed to the relatively large gap between the resonator body and the tuning electrodes (~ 2 μm). Figure 2-13 shows the result of electrostatic tuning of the three trench resonator across the temperature range of +50 °C to +85 °C using a single tuning electrode.

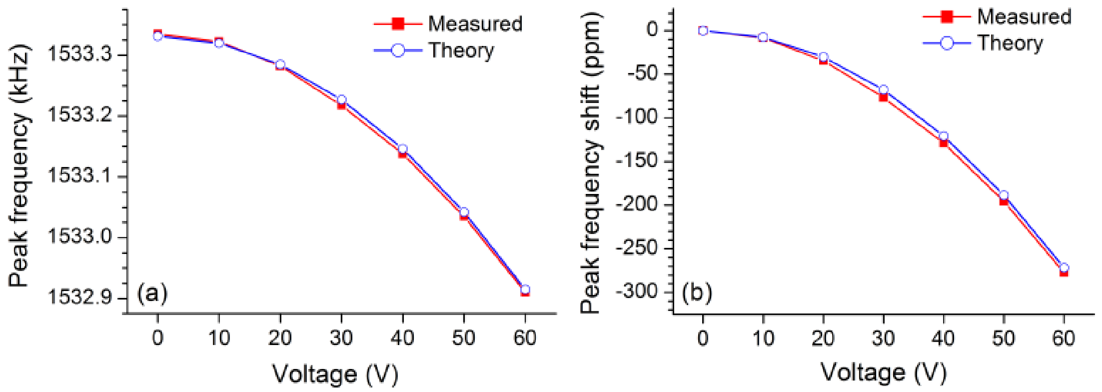

Figure 2-12: Measured and calculated frequency tuning as a function of applied DC voltage for a trenchless device. (a) The change in peak frequency and (b) the total frequency tuning in ppm.

To obtain the data in Figure 2-13, the reference temperature was chosen to be +50 °C (since device has positive TCF). As the temperature was increased, the frequency increases due to the resonator TCF. A corresponding DC bias voltage, calculated from the frequency-voltage curve at that temperature, was then applied at each temperature reading to tune the center frequency back to that at the reference temperature. Multiple readings were recorded at each temperature and voltage setting to look at the stability of tuning. The overall tuning accuracy is seen to be within 1 ppm. It should be noted that only a single tuning electrode was used to compensate the temperature induced frequency shift for this measurement.

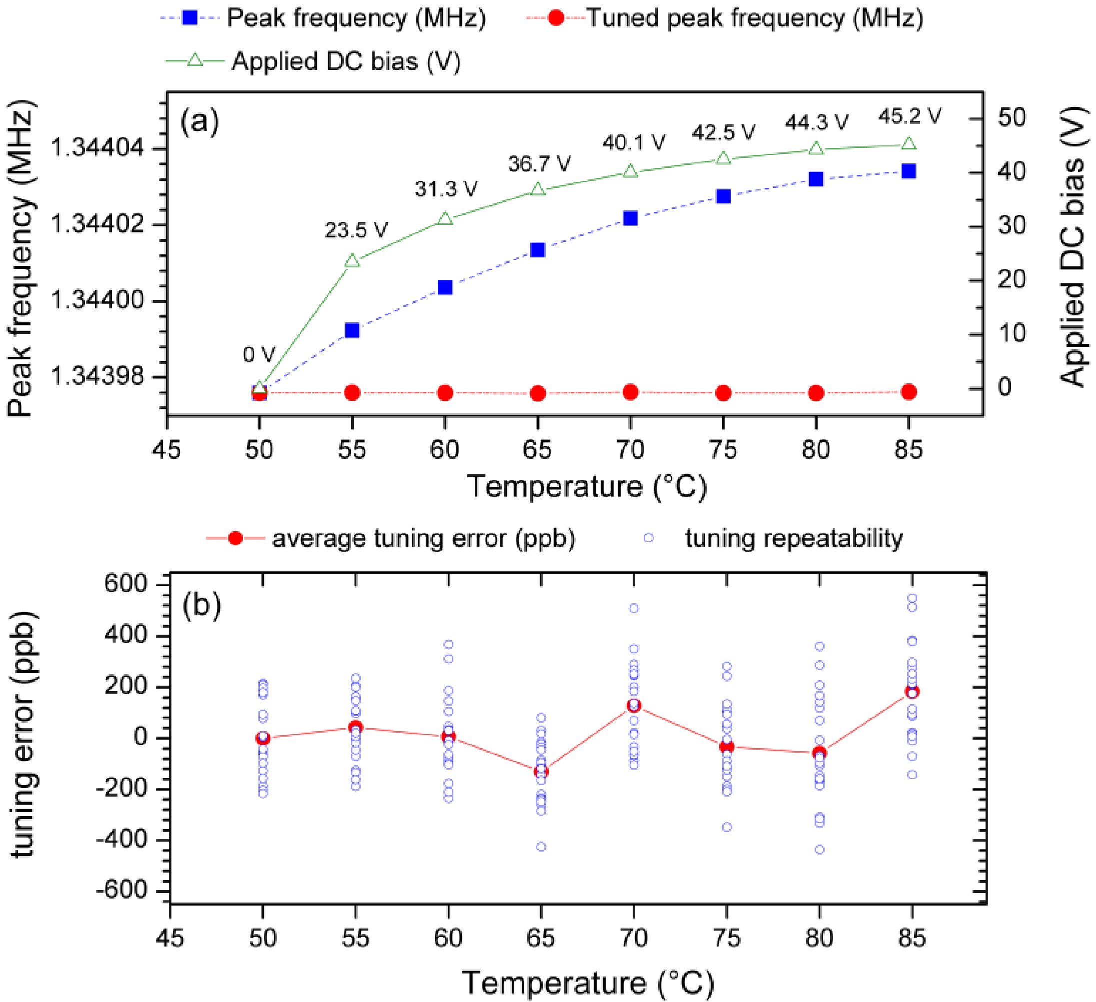

Figure 2-13: (a) Measured frequency change with temperature for a three trench device. The tuned frequency with applied DC voltage is also plotted to demonstrate the viability of this approach in achieving temperature stable resonators. (b) Tuned peak frequency as a function of temperature and voltage. The graph details the tuning error for multiple measurements (total 20 readings at each temperature) at each voltage setting and the average value. The tuning error is within 1 ppm and is set by power supply fluctuations, resonator drift and the stability of the temperature controller.

Active tuning using electrostatic spring softening effect requires the application of a nominal DC bias voltage since the tuning is unidirectional. An alternative way is to utilize the piezoelectric tuning effect under the application of DC bias. Figure 2-14 shows the measurement setup that is used to measure the piezoelectric tuning. Figure 2-15 shows the measured piezoelectric tuning result for a

three trench device. The total tuning range is ~5 Hz and may be increased by improving the ratio of thickness of AlN to silicon in the resonator. Such a bidirectional compensation technique can be extremely useful in ovenized reference oscillators, where the total frequency fluctuation is small but a fine control on the output is essential to meet the stringent timing error specifications [45].

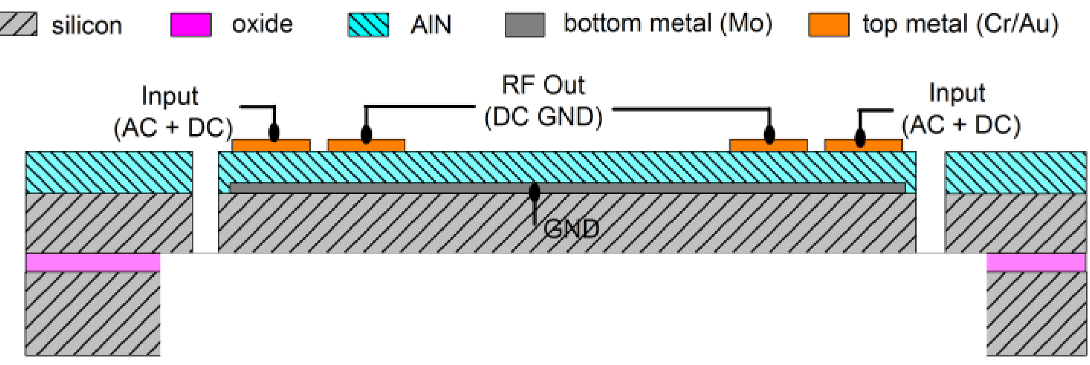

Figure 2-14: Cross-section schematic of the AlN-on-silicon flexura-mode resonator, detailing the stack layers and the measurement conditions for piezoelectric tuning.

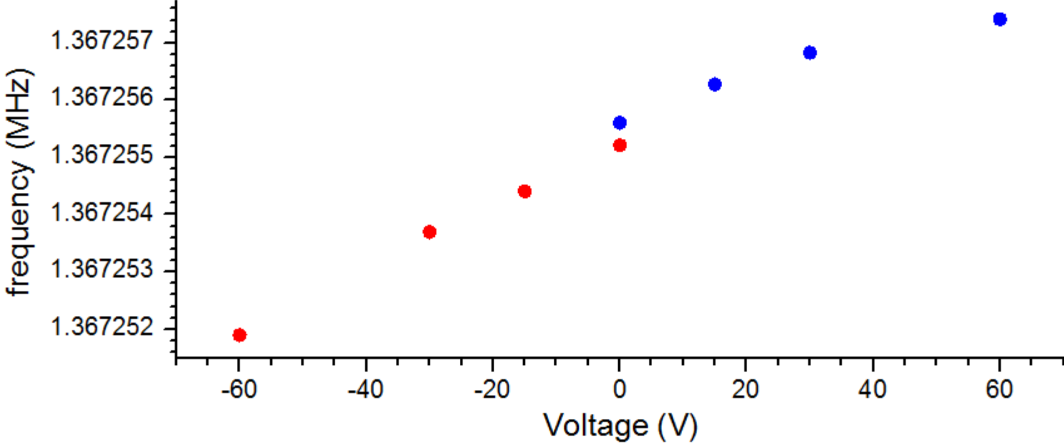

Figure 2-15: Measured bidirectional frequency tuning using the piezoelectric effect. The total tuning range is measured to be 5 Hz for a three-trench device. The tuning range can be significantly improved by improving the thickness ratio of AlN to silicon in the device.

2.1.7 Estimation of Resonator Stability

A major challenge in the application of MEMS resonators in timing references is their susceptibility to frequency noise which is added to the phase noise in an oscillator implementation [1]. Likely causes of frequency instability in resonators include external factors such as temperature drifts, power supply fluctuations, along with the intrinsic resonator drift. A clear manifestation of such instabilities can be seen from the measured tuning stability in Figure 2-13. In order to provide an estimate of the resonator intrinsic drift, a compensation scheme is implemented to keep the resonator center frequency constant by changing the applied DC bias in a feedback loop. With this technique, any drift effects can be reduced leading to a more frequency stable resonator performance. Thus the measured variation, with the applied compensation, provides a rough estimate of the resonator intrinsic drift. Figure 2-16 shows the measured results for the same device obtained with and without frequency compensation.

The feedback algorithm is implemented using LabVIEW (National Instruments, Austin, TX) with the error signal calculated as the difference in the measured frequency and the reference frequency. The starting DC bias is taken to be 50 V and a proportional feedback correction is applied with a resolution of 0.1 V. These measurements are carried out at room temperature in vacuum. The histogram of the measurement data is also plotted for reference. From the results, the standard deviation (σ) for center frequency shift is calculated to be 36 ppb and demonstrates the improved resonator stability possible with appropriate drift compensation techniques. It should be noted that this σ is a conservative estimate and can be further

improved either by optimizing the feedback control implementation or by compensating out any correlated drift effects through the use of multiple resonators.

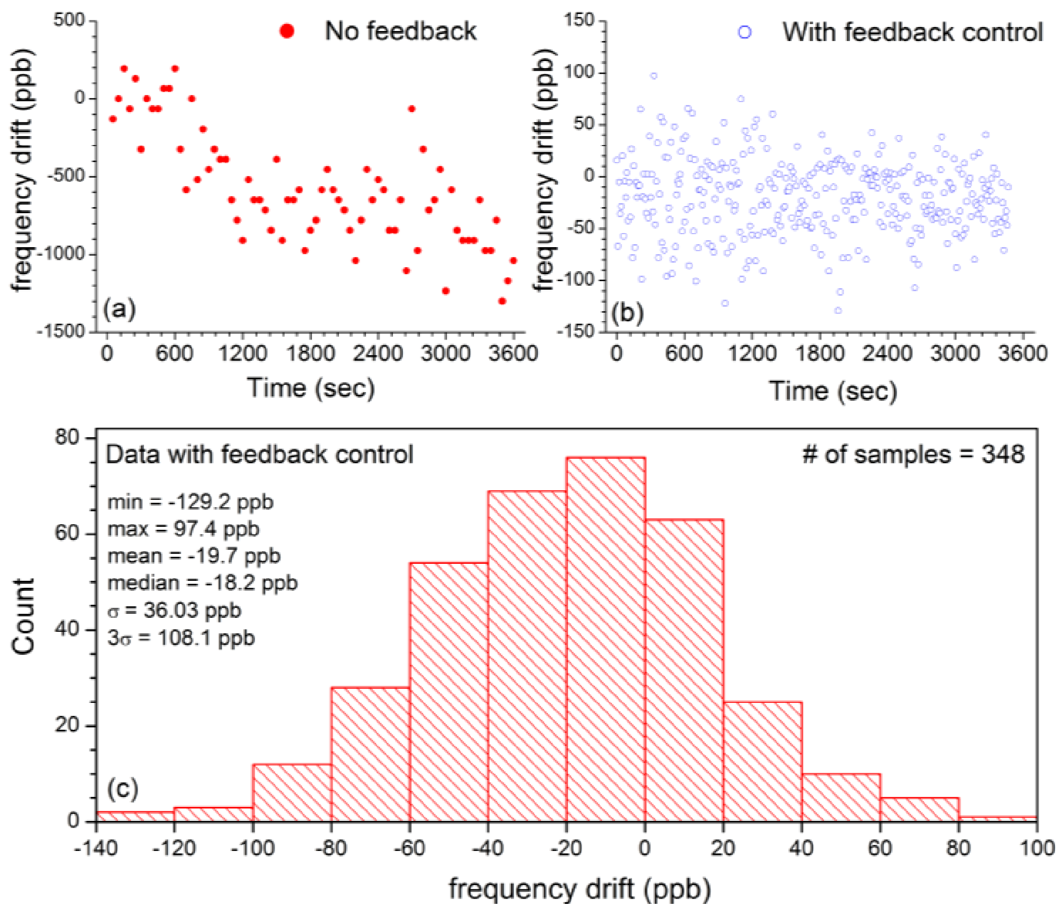

Figure 2-16: Measured drift of the resonator center frequency (a) without and (b) with feedback control loop. (c) Histogram plot of the resonator center frequency with feedback control showing the calculated statistical parameters assuming a Gaussian distribution. The resonator intrinsic drift is seen to be better than 110 ppb (3σ number).

2.1.8 Flexural-Mode Resonator: Summary of Results

The passive temperature-compensation scheme was verified using flexural resonators. Oxide-refilled trenches were positioned at the location of maximum strain, reducing the volume of oxide required for elimination of the first-order TCF terms. From the results presented it is clear that the flexural-mode resonators have a

reasonably high Q that is limited by thermoelastic damping. The temperature compensation scheme is verified through the measurement results and we note a small degradation in resonator Q with the addition of the oxide trenches. The short-term stability of this resonator was also studied and is shown to be below 110 ppb at room temperature and in vacuum. Capacitive and piezoelectric tuning techniques were both demonstrated on these resonators, which can be used to compensate for small frequency drift. Packaged resonators hermetically sealed from the atmosphere are likely to show an improved performance, suitable for use in the multi-resonator system.

The motional impedance for the flexural resonators presented is found to be quite large due to charge cancellation in shear modes and thus implementing low-noise oscillators with these resonators will be challenging. However, use of alternate resonator topologies such as the coupled-ring resonator, described in the next section, can show a much lower motional impedance. The same temperature compensation strategy is utilized for the coupled-ring resonators and measured results are in good agreement with the analysis presented for the flexural-mode resonators.

2.2 Coupled-Ring Resonators

Extensional mode resonators have been explored in literature and have been shown to provide a low motional impedance with piezoelectric actuation [34]. Breathing-mode ring resonators implemented with AlN-on-silica have been recently shown with a low insertion loss of 12 dB, and are thus ideally suited for oscillator implementation [21], [46]. This section describes our effort on the design of temperature-compensated breathing-mode ring resonators [37].

2.2.1 Device Structure

Figure 2-17 shows the schematic of the coupled-ring resonator with the relative position of the oxide rings within the silicon body marked for clarity.

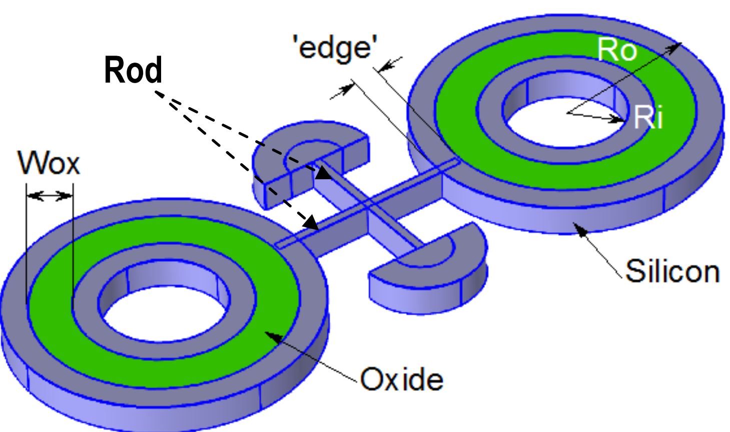

Figure 2-17: Schematic of a temperature-compensated coupled-ring breathing-mode resonator. The oxide-refilled regions are clearly marked for clarity. Note that the schematic does not show the piezoelectric stack.

The central beam connectors are designed to provide a strong elastic coupling between the two rings and to effectively isolate the displacement of the beams from its support. This approach allows us to minimize the effect of anchor loss on the resonator *Q*. The mode-shape of resonator is shown in Figure 2-18.

2.2.2 Device Geometry

Using finite element models tested with the flexural-mode resonators, coupled-ring resonators are designed to maximize the anchor *Q* and minimize thermoelastic damping. Table 2-6 presents the resonator geometry used in the experimental demonstration. The simulated frequency for this resonator is 21 MHz with a total simulated *Q* of 700,000.

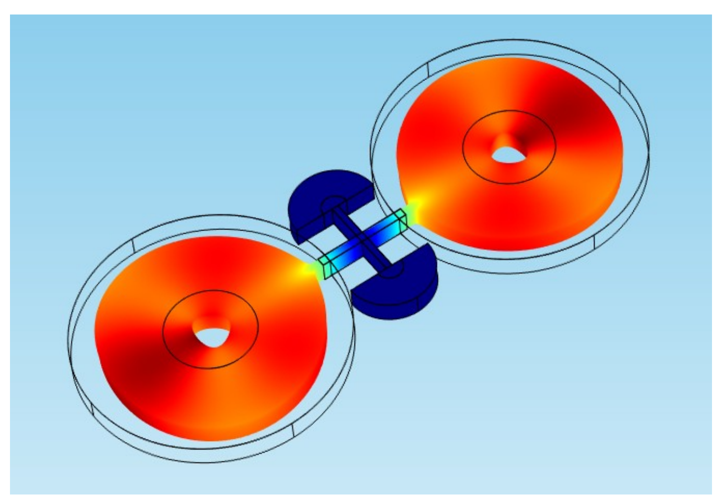

Figure 2-18: Simulated mode shape of the coupled-ring resonator

Table 2-6: Ring resonator geometry optimized for high *Q* performance

Parameter	Dimension (µm)	Parameter	Dimension (µm)
Ring inner radius	35	Rod width	6
Ring outer radius	90	Rod length	110
Silicon thickness	20	AlN thickness	1

2.2.3 Temperature Compensation

Using an approach similar to the one presented in Section 2.1.1, the ring resonators can be compensated relatively easily by the inclusion of oxide rings within the silicon body. Two parameters are critical to note here: width of oxide and its

spacing from the resonator edge and these are marked in Figure 2-17 for reference. It is found that while maintaining the same width of oxide, the amount of temperature compensation can be changed by changing the distance of this oxide from the edge of the resonator. This is clearly seen from the plot in Figure 2-19. Thus it is possible to achieve multiple turnover temperatures for adjacent ring resonators through only lithography variations keeping the same process flow [37].

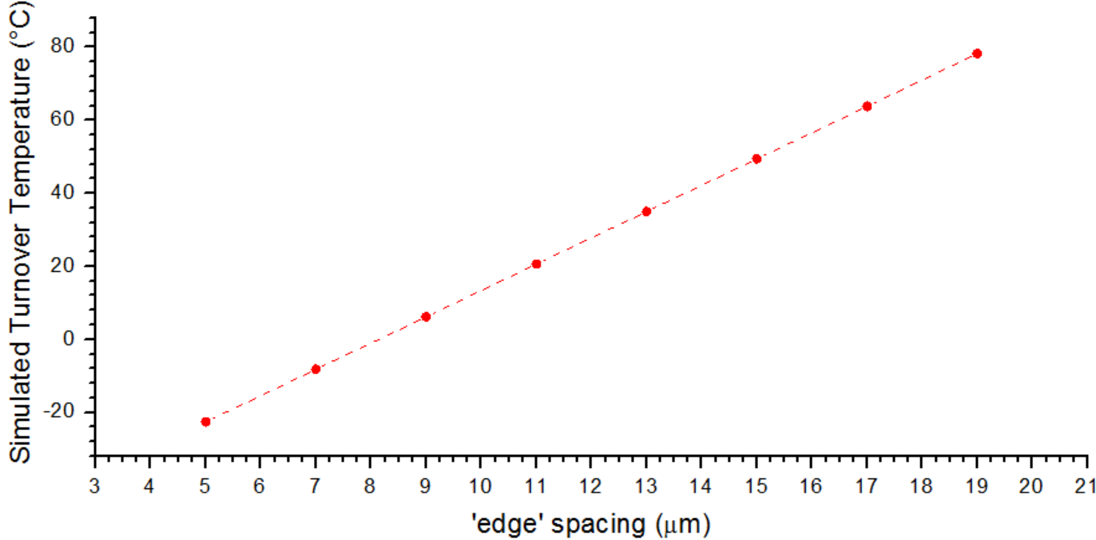

Figure 2-19: Simulated turnover temperature for the compensated ring resonators as a function of 'edge' spacing. This dimension is marked for clarity in Figure 2-17. Note that all devices have the same 23.5 μm width of silicon dioxide.

2.2.4 Resonator Fabrication

The fabrication process used is very similar to the one described in Section 2.1.3 earlier and a brief overview of the process flow is presented in Figure 2-20. To achieve the required oxide-refilled rings, 5 trenches are made in the silicon device layer each 2.5 μm wide with 2.1 μm of silicon in between. After 2.5 μm of wet thermal oxidation, we obtain fully refilled oxide rings within the silicon body. Figure 2-21 shows a cross-section view revealing the quality of the trench refill process.

Figure 2-21 reveals a top SEM view of a fabricated temperature-compensated ring resonator having an 'edge' spacing of 13 µm.

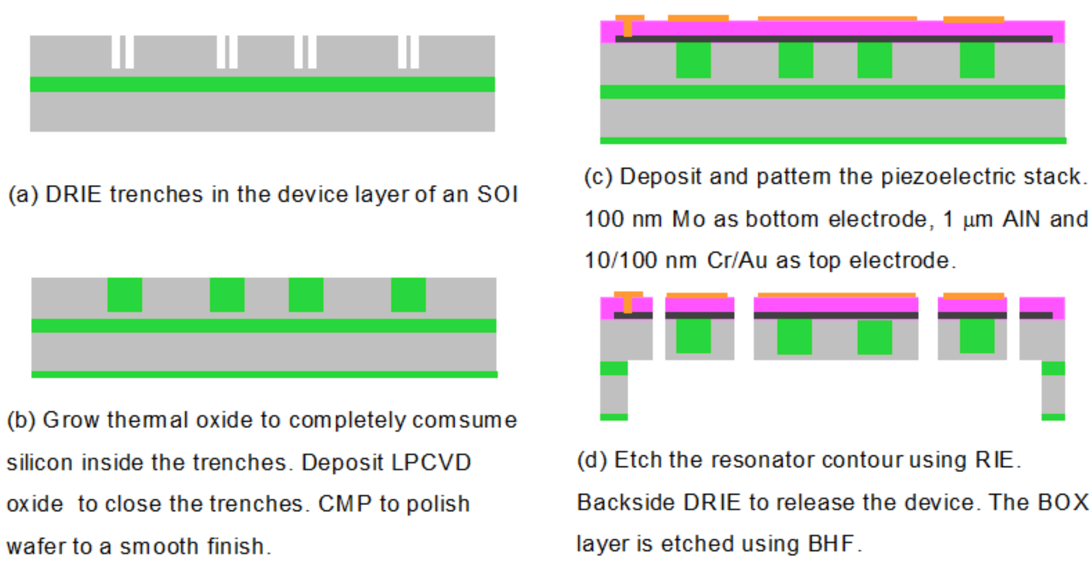

Figure 2-20: Process flow used in the fabrication of the ring resonators.

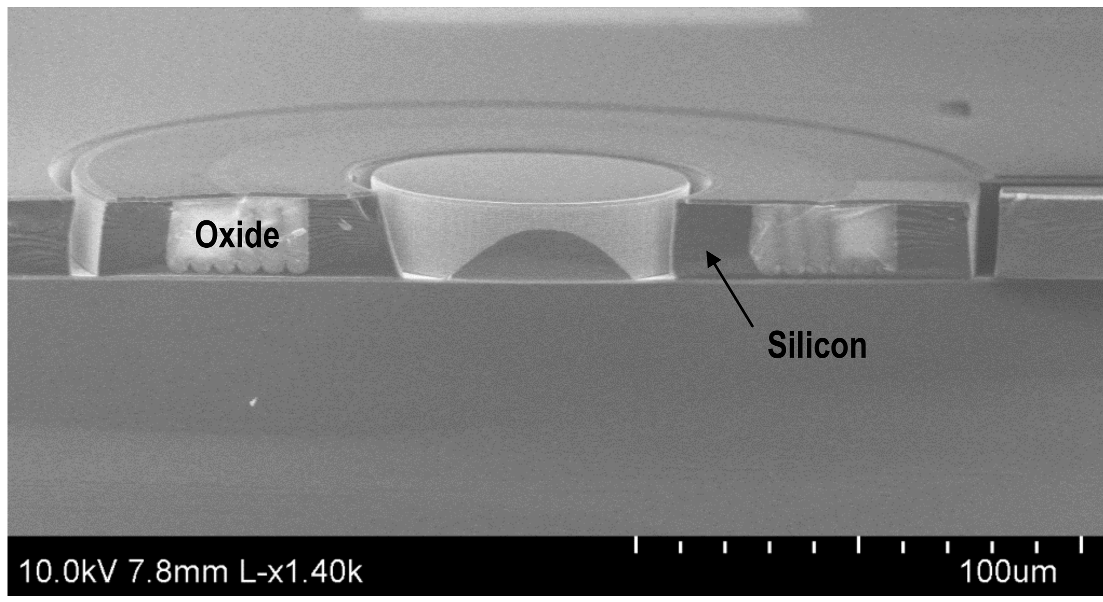

Figure 2-21: Cross-section SEM view of the oxide-refilled trenches within the silicon volume.

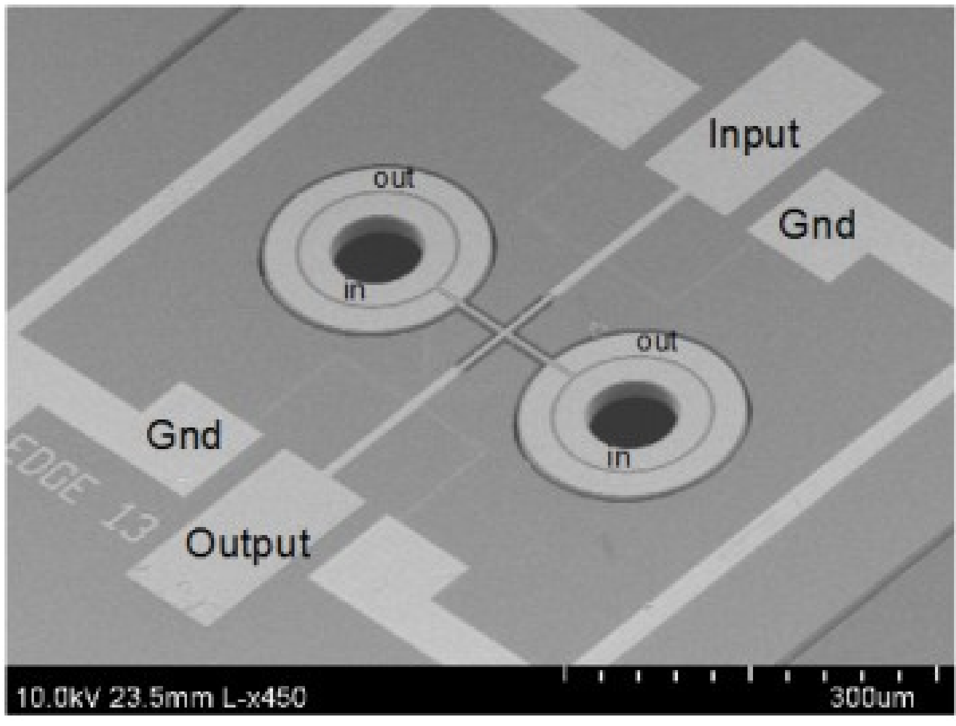

Figure 2-22: SEM view showing a fully released temperature compensated ring resonator. Note that the oxide rings are not visible due to the presence of the piezoelectric stack.

2.2.5 Measured Results

A number of ring resonators were measured in air using an Agilent E5061B Network Analyzer. Owing to the relatively large operating frequency and large device contour openings, air damping is found to be insignificant. Figure 2-23 shows the measured frequency response (transfer function) for three temperature-compensated ring resonators and an uncompensated ring resonator for comparison. From the results in Figure 2-23 we note that the motional impedance of the ring resonators is between 300 Ω to 600 Ω, which is suitable for low-noise oscillator implementation. We also note the relatively small performance degradation between the compensated and uncompensated ring resonators indicating the advantages of optimized oxide placement within the resonator body.

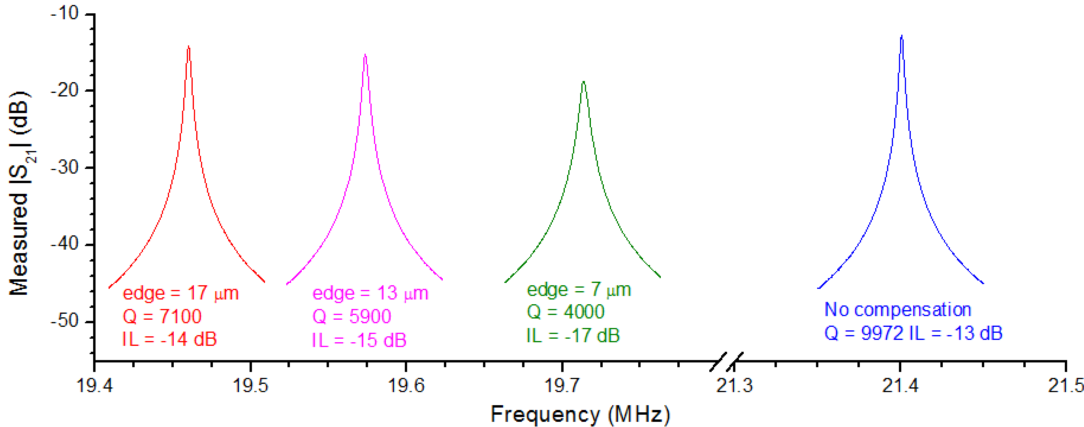

Figure 2-23: Measured frequency response for three temperature-compensated resonators. The measured result for an uncompensated ring resonator is also included for comparison. All measurements are carried out at room temperature and pressure with input power of -10 dBm.

In order to characterize the effect of temperature on the resonator frequency, the same devices are measured in a Lakeshore cryogenic probe station from -40 °C to +85 °C with the results plotted in Figure 2-24. We note a small deviation in the measured turnover temperature as compared to the simulated data presented in Figure 2-19. This is attributed to fabrication variations due to which the trenches in silicon have non-ideal opening size. Thus post-oxidation, we may either have some leftover silicon between the trenches or air gaps due to insufficient silicon for complete trench-oxidation.

The results in Figure 2-23 and Figure 2-24 suggest that the ring resonators are ideally suited for the multi-resonator clock system. The low motional impedance in addition to the availability of multiple resonators with unique turnover characteristics will be utilized for the proof-of-concept implementation of the clock architecture in Chapter 3.

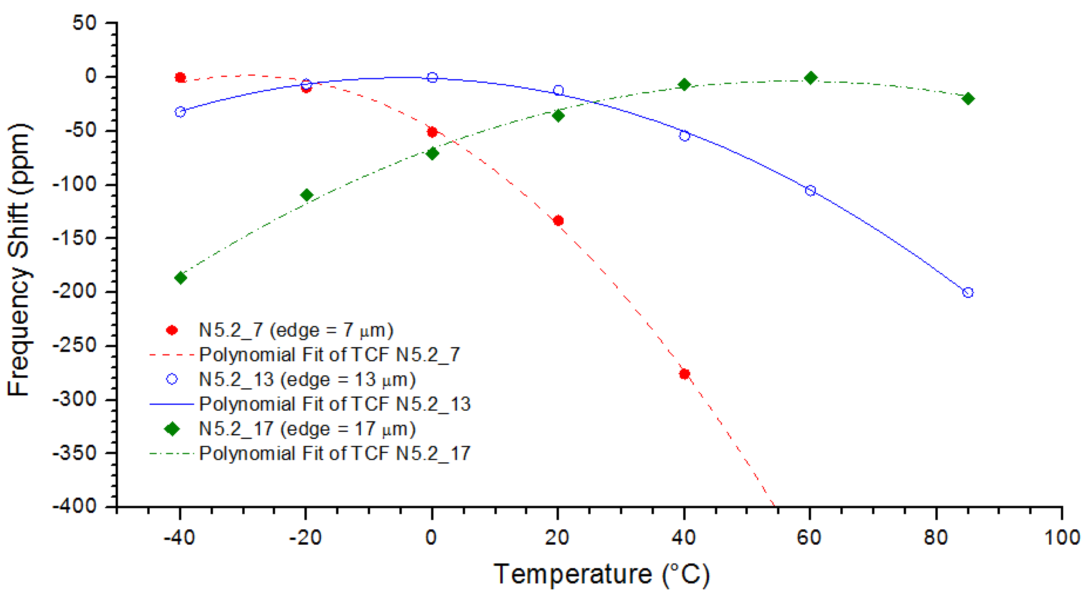

Figure 2-24: Measured relative frequency shift in ppm as a function of temperature for the three temperature-compensated resonators shown in Figure 2-23.

In summary, this chapter includes the following research contributions:

- Development and demonstration of a new temperature-compensation technique based on the relative position of silicon dioxide within a silicon resonator.
- Control over the turnover temperatures within the same process flow through positioning the oxide trenches. This has been demonstrated for both flexural-mode and extensional-mode resonators.

Chapter 3 DESCRIPTION OF THE MULTI-RESONATOR CLOCK AND ITS IMPLEMENTATION

As has been discussed in Chapter 1, temperature-stable frequency references serve critical functions in timekeeping applications, inertial measurement units (IMU), and communication systems. A number of approaches have been proposed and successfully implemented to realize temperature-stable oscillators. Use of ovenization, wherein the resonator is maintained at a relatively high temperature of ~ 90 °C has been successfully used to achieve temperature-stable frequency references [45], [47]. More recently, the temperature stability of MEMS-based electrostatic resonators has been improved through the use of a temperature sensor fabricated adjacent to the resonator and by compensating for the sensed temperature variation through a phase locked loop (PLL) based frequency multiplication [9].

In this chapter we discuss a novel approach to achieve temperature-stable clocks. Figure 3-1 presents a schematic of the proposed multi-resonator clock algorithm. The clock uses three silicon based temperature-compensated resonators each with a different turnover temperature. The resonators are compensated using the passive compensation technique discussed in Chapter 2. Due to the nature of the temperature coefficients, the passively compensated silicon resonators demonstrate a second-order temperature dependence of frequency, as was seen from the data in Figure 2-11 and Figure 2-24. Through frequency manipulation in two stages, we can achieve a temperature-insensitive clock signal at the output. This approach requires

significantly lower power as compared with ovenized solutions and circumvents the need to integrate an accurate temperature sensor with the resonator as is required in [9]. Using this approach it will be possible to completely eliminate the second-order temperature dependence of silicon MEMS resonators.

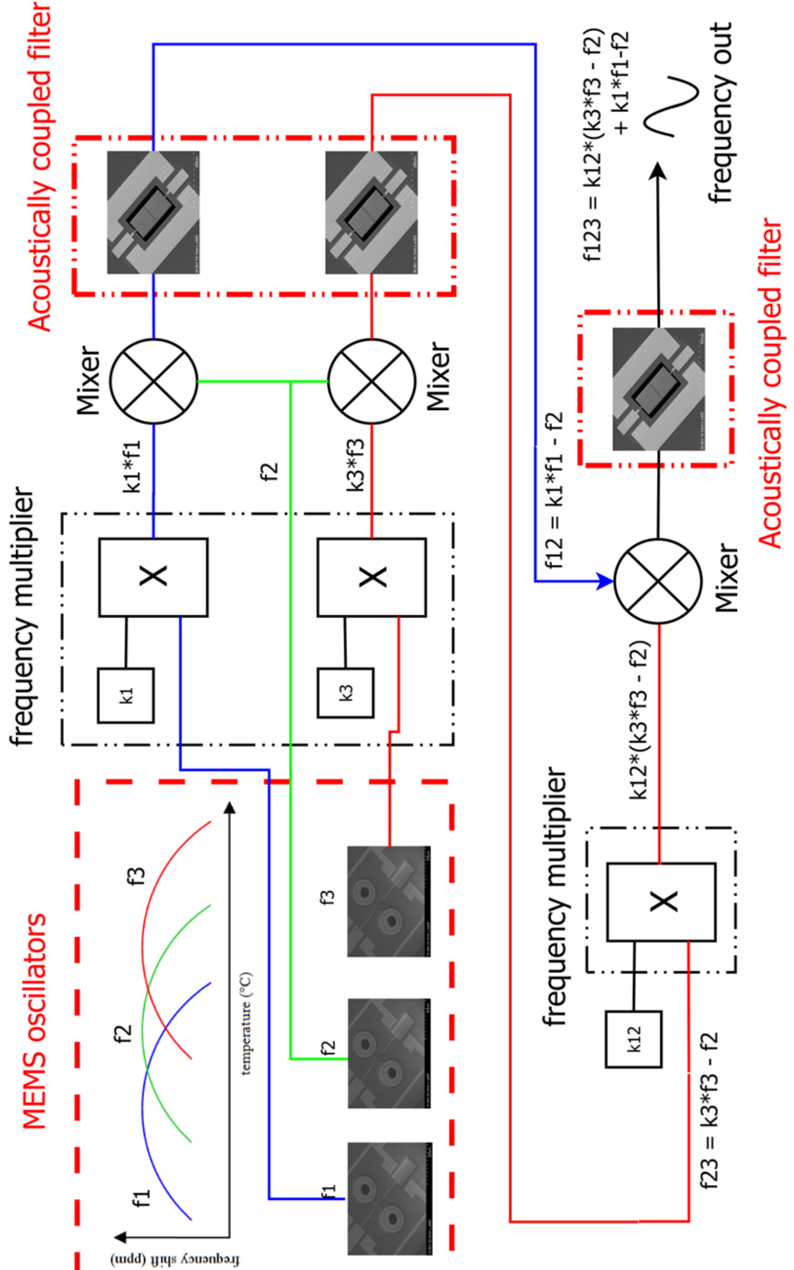

Figure 3-1: Schematic of the proposed multi-resonator clock algorithm. The system requires the development of two main components: multiple resonators with unique turnover temperatures and low bandwidth, low insertion loss bandpass filters to reject the unwanted frequency products at the mixer output.

3.1 Description of the Multi-Resonator Clock

As can be seen from the schematic in Figure 3-1, the system utilizes three oscillators with different turnover temperatures, which is defined as the inflection point of the parabolic dependence of the resonator frequency with temperature. The frequency of each oscillator can be written as

$$f_n = a_n T^2 + b_n T + c_n. \qquad \text{Equation 3-1}$$

Because of having different turnover temperatures, the three resonators have unique and non-zero coefficients a, b and c. The output of the three oscillators undergoes frequency multiplication and mixing in two stages to achieve a final temperature-stable frequency reference. Stage I multiplication factors k_1 and k_3 are set so as to ensure a purely second-order frequency dependence on temperature. At the output of the first set of mixers we can write,

$$\begin{cases} f_{12} = (k_1 a_1 + a_2)T^2 + (k_1 b_1 + b_2)T + (k_1 c_1 + c_2) \\ f_{23} = (k_3 a_3 + a_2)T^2 + (k_3 b_3 + b_2)T + (k_3 c_3 + c_2) \end{cases}. \qquad \text{Equation 3-2}$$

The above equation sets the multipliers k_1 and k_3; to ensure no first-order dependence of frequency on temperature, we have

$$k_1 = -\frac{b_2}{b_1} \text{ and } k_3 = -\frac{b_2}{b_3}. \qquad \text{Equation 3-3}$$

Thus, at the input of the second mixer, the two frequency signals have a pure second-order temperature dependence, which can be compensated using a similar approach. The multiplier k_{12} is subsequently determined such that the second-order term is canceled. The parameter k_{12} can be calculated using,

$$k_{12} = -\left[\frac{k_3 a_3 + a_2}{k_1 a_1 + a_2}\right], \qquad \text{Equation 3-4}$$

and the final output frequency can be written as,

$$f_{123} = k_{12} k_1 c_1 + (1 + k_{12}) c_2 + k_3 c_3. \qquad \text{Equation 3-5}$$

The equation for the output frequency is a combination of constants independent of temperature, and thus this system allows for the realization of a temperature-insensitive clock.

Compared to existing clock algorithms, the system described in Figure 3-1 does not require a fractional phase locked loop (PLL) with a temperature dependent frequency multiplier. Frequency multiplication using fractional PLLs has a limited resolution on the multiplier set by the number of control bits available and thus the proposed clock architecture allows for a considerable simplification in the PLL design. Secondly, by the inclusion of an additional (fourth) temperature-compensated resonator, a temperature-insensitive clock output can be designed with a range of k values. More importantly, through appropriate design of the clock architecture, the k multipliers can be set to be integers instead of fractions. This would allow the fractional PLL to be replaced with an integer PLL, reducing the overall system phase noise and thus improving the clock timing accuracy.

While the following sections describe the system dependence on resonator performance for three resonators, the presented analysis can be easily extended to include additional resonators.

3.2 Sensitivity to Resonator Drift

The effect of temperature-independent frequency drift can be captured in Equation 3-1 by noting,

$$f_n = a_n T^2 + b_n T + (c_n + d_n), \qquad \text{Equation 3-6}$$

where d_n is temperature-independent frequency drift for the nth resonator. Following a similar approach as in the previous section, the effect of individual resonator drift at the clock output can be written as,

$$(f_{123})_d = f_{123} + k_{12}k_1d_1 + (1 + k_{12})d_2 + k_3d_3. \qquad \text{Equation 3-7}$$

As can be noted from Equation 3-7, since k_1, k_3 and k_{12} are invariant with temperature, the resultant frequency $(f_{123})_d$ is also independent of temperature, but has a constant offset from the original calibrated output frequency.

An important point to note here is the effect of the frequency multipliers. Since the output frequency is a linear combination of the product of individual resonator frequency and the k multipliers, the drift components are also multiplied by the same ratio. By setting smaller values for the k multipliers (< 1), the effect of frequency instability on the clock output can be made smaller than that for the individual oscillators.

3.3 Sensitivity to Measurement Errors

3.3.1 Non-uniform temperature distribution in measurement chamber

Considering that most low-frequency resonator measurements are performed in low-vacuum conditions [28], it is quite possible that the measurement chamber has some temperature non-uniformity. Since the temperature controller strives to maintain the sensor at the set temperature rather than the temperature of the actual resonator, this implies the resonator may either lead or lag the sensor temperature depending on the nature of the non-uniformity. This can cause an error in the measurement during the calibration process, due to which we have,

$$f'_n = a'_n T^2 + b'_n T + c'_n, \qquad \text{Equation 3-8}$$

whereas the real temperature dependence is given using Equation 3-1. For the purpose of this analysis we can split the measured individual coefficients a'_n, b'_n and c'_n into a real component and an error component. Then, we can express f'_n as,

$$f'_n = (a_{0n} + a_n)T^2 + (b_{0n} + b_n)T + (c_{0n} + c_n) \qquad \text{Equation 3-9}$$

and,

$$f'_n = f_n + f_{0n}. \qquad \text{Equation 3-10}$$

Here, a_{0n}, b_{0n} and c_{0n} are the respective error components for the nth resonator while f_{0n} is the total frequency error for the nth resonator. Again, following the same steps from Equation 3-1 to Equation 3-5, we can express the effect of measurement error on the system output as,

$$f'_{123} = f_{123} + k_1 k_{12} f_{01} + (1 + k_{12}) f_{02} + k_3 f_{03}. \qquad \text{Equation 3-11}$$

We should note here that f_{0n} values are temperature dependent and thus the clock output too has second-order temperature dependence.

3.3.2 Temperature sensor calibration error

In this case, while we assume the resonator to be at temperature *T*, in reality it is operating at temperature *T'*. This would lead to a simplified case of Equation 3-11 wherein the turnover temperature is incorrectly estimated by *(T-T')* but the shape of the frequency-temperature dependence (parabola) remains unchanged. In this case, we have no change in a_{0n} and we can write,

$$f_{0n} = b_{0n} T + c_{0n}. \qquad \text{Equation 3-12}$$

Equation 3-11 and Equation 3-12 given above suggest that non-idealities during measurement of the individual resonators can significantly impact the temperature sensitivity of the clock output. This is graphically represented in Figure 3-2. Figure 3-2(a) plots the expected nature of the temperature dependence of clock frequency with temperature errors. Figure 3-2(b) plots the clock output in presence of a constant temperature sensor calibration error. Results suggest that proper care must be taken during calibration to ensure that these errors are minimized to enable the temperature-insensitive clock output.

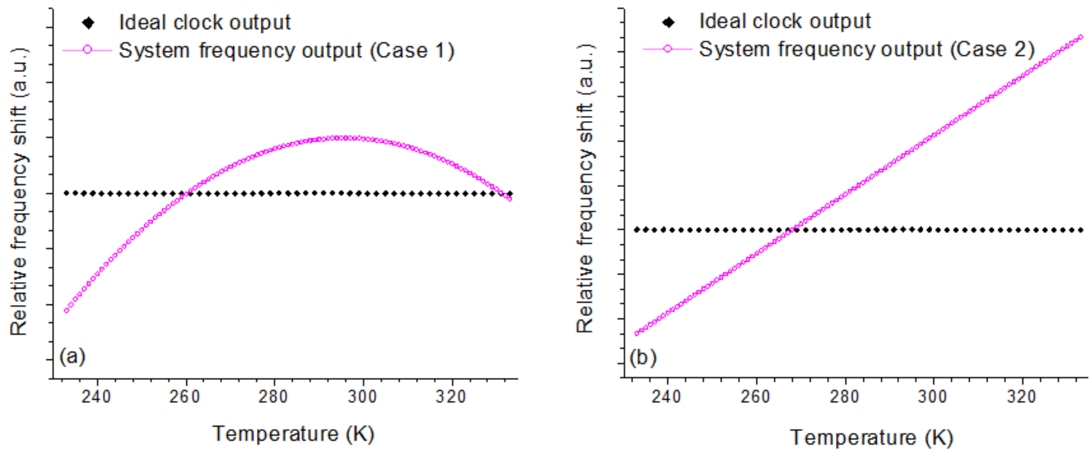

Figure 3-2: Graphical representation of the temperature dependence of the clock frequency output due to (a) temperature errors during measurement and (b) constant temperature sensor calibration error. Note that the plots are representative and are not drawn to scale.

3.4 Other Sources of Non-Idealities

While it is known that a passively compensated resonator (*i.e.*, a silicon/silicon dioxide composite resonator) demonstrates second-order temperature dependence, the oscillators may deviate from this behavior on account of the inclusion of the amplifier and passive elements in the feedback loop (the temperature dependence of the circuit components may not be limited to second order). The effect of the circuit components can be easily captured during the initial calibration through the measurement of temperature dependence of the full oscillator instead of only the resonators. Considering an *n*-order temperature dependence of frequency for the oscillators, the presented algorithm can be expanded to a clock consisting of $n+1$ oscillators to nullify the temperature dependence of the clock output frequency. Thus, the higher order temperature dependence of the circuit may be cancelled out through the inclusion of additional oscillators in the system.

3.5 Oscillator Implementation

The coupled-ring resonators presented in Chapter 2, Section 2.2 are ideally suited for low-noise oscillator implementation, due to their low motional impedance. This section describes the design and characterization of a pierce oscillator using the ring resonators [46], [48].

3.5.1 Oscillator Circuit

An oscillator is designed in the pierce configuration using the ring-resonators as the frequency setting element. Since the ring resonators have a low insertion loss, a simple sustaining amplifier circuit was designed consisting of a single BJT (NESG4030M14) connected in the common emitter configuration [49]. Figure 3-3 shows the circuit diagram of the oscillator. Resistor values for the common emitter configuration were chosen to ensure the transistor is biased in its forward-active region, where the collector current is a proportional amplification of the small base current going into the BJT. Capacitors C_1 and C_2 are used as coupling capacitors to separate AC signal from DC biasing of the transistor. A transformer balun (180° phase shifter) was used to adjust the phase shift around the oscillator loop, thus ensuring satisfaction of the Barkhausen criteria for oscillation. The same circuit is used for all three MEMS oscillators that are needed to implement the proposed multi-resonator clock.

The MEMS coupled-ring resonators were wire-bonded in a package that was mounted on a custom printed circuit board (PCB) designed to hold up to four oscillator circuits, as shown in Figure 3-4. Different temperature-compensated resonators are connected to their respective circuit on the board.

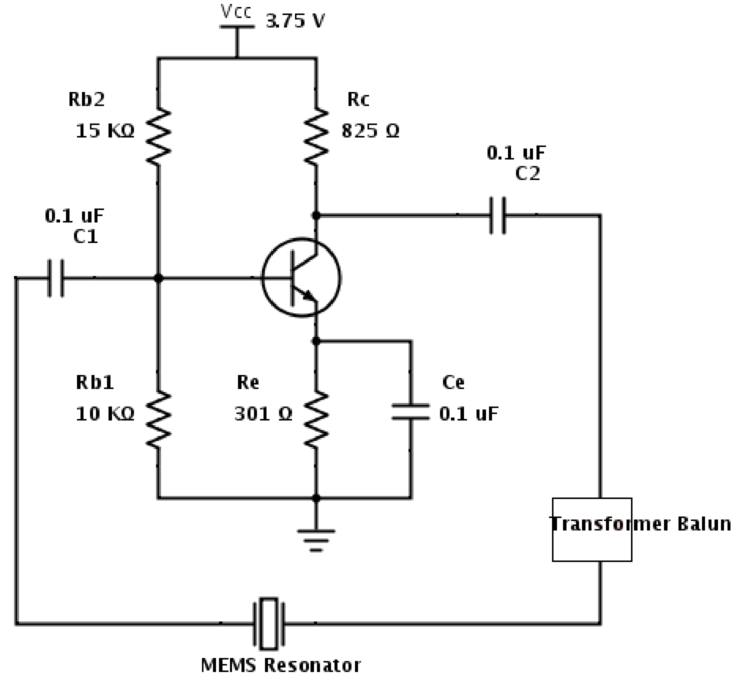

Figure 3-3: Circuit diagram of the oscillator implementation using the pierce configuration. The same design is suitable for all the temperature compensated oscillators needed in the proposed multi-resonator system.

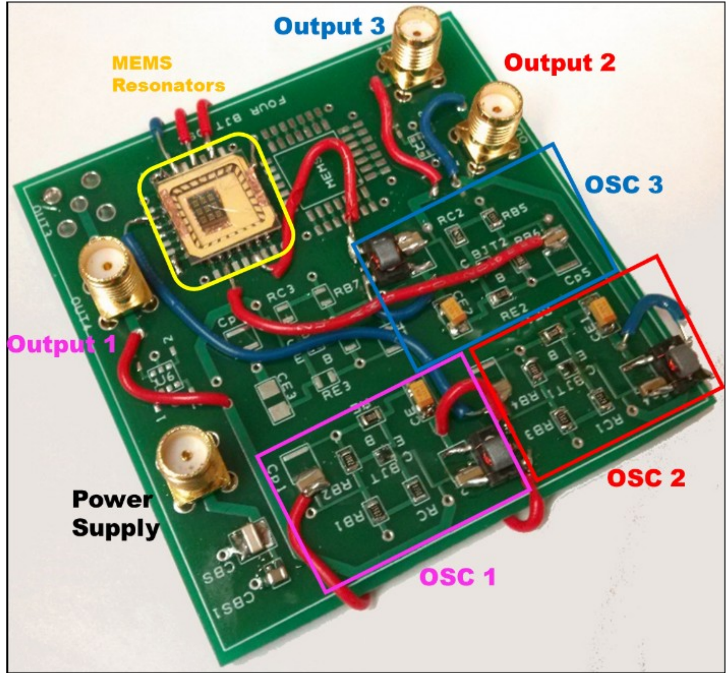

Figure 3-4: PCB with three out of four oscillator circuits connected. The MEMS chip (resonators) is fixed and wire-bonded to a package for making the circuit connections.

3.5.2 Oscillator Measurements

Figure 3-5 shows the output waveform for three oscillators on the PCB shown in Figure 3-4. From the waveforms, we can see that the output signal includes higher order harmonics on account of the highly non-linear nature of the BJT used in the circuit. The high frequency signal content can be eliminated either by incorporating a low-pass filter or by replacing the BJT with a more linear CMOS operational amplifier [46].

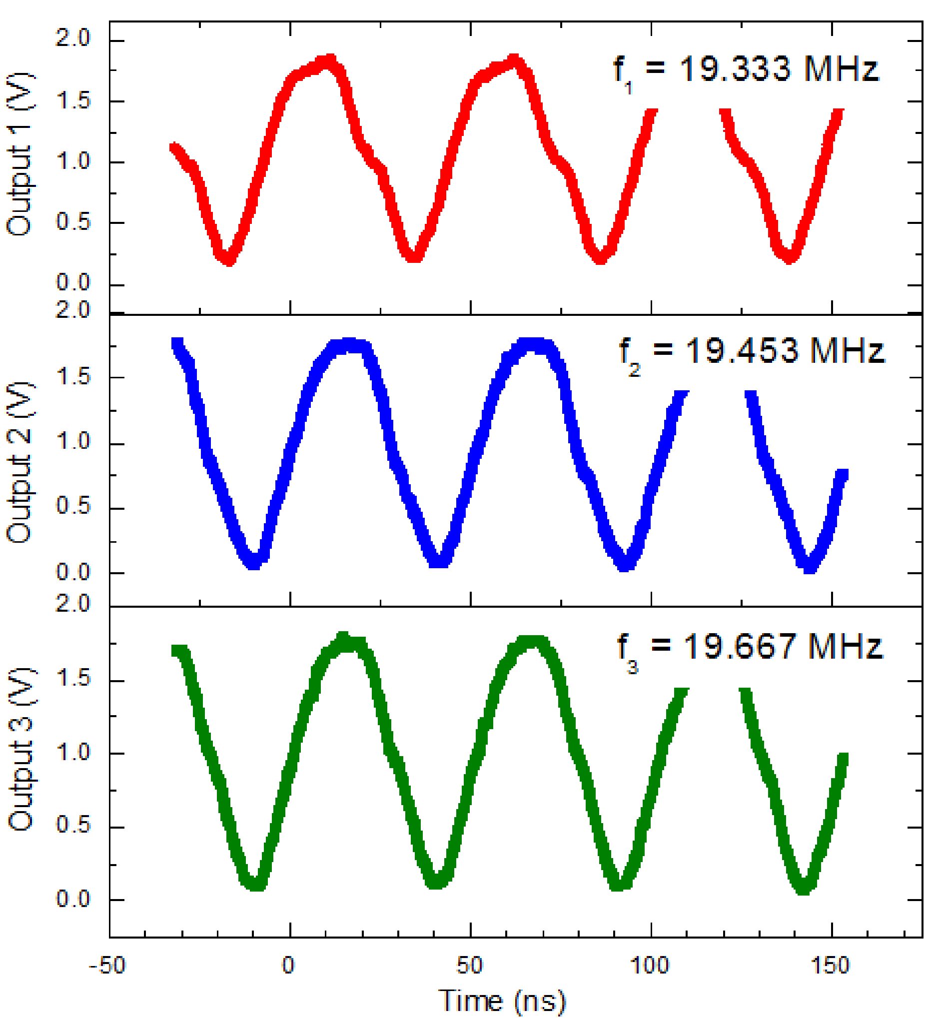

Figure 3-5: Output of the three oscillators on the PCB having three different temperature-compensated resonators.

The phase noise of the oscillator is an important metric for timing references as it translates directly into the timing jitter *i.e.* timing uncertainty. The phase noise of the presented oscillators is measured using an Agilent E5500 phase noise measurement system and the result is shown in Figure 3-6.

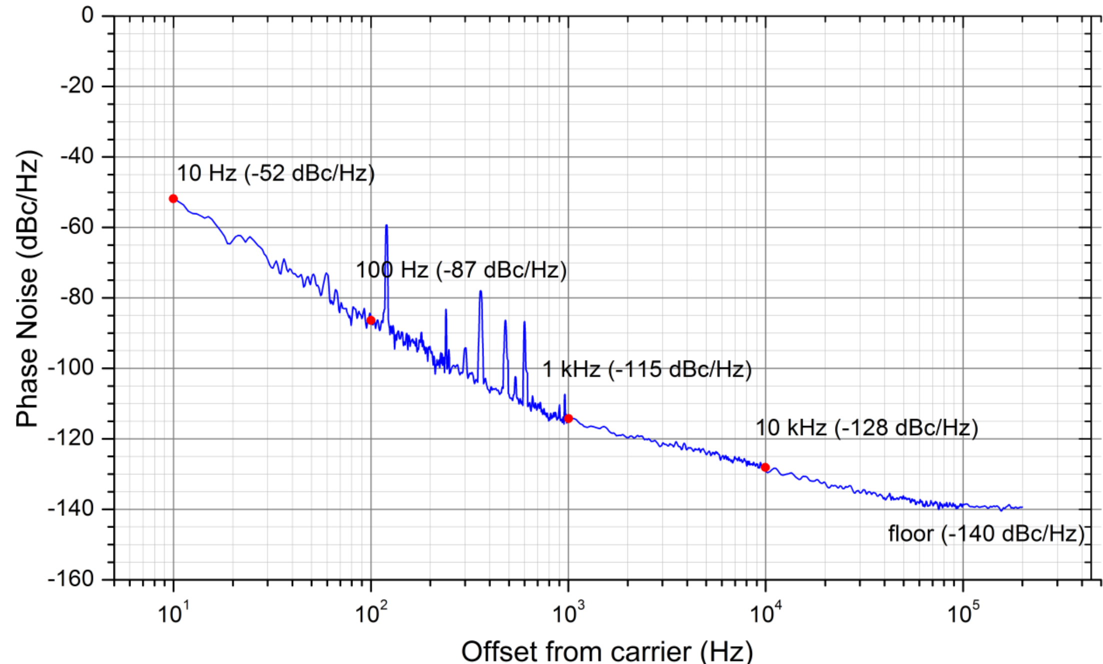

Figure 3-6: Measured phase noise plot for a typical pierce oscillator implemented using the presented temperature-compensated ring resonators.

Table 3-1 summarizes the measured phase noise results for different temperature-compensated MEMS oscillators in the frequency range of 6-100 MHz published in literature. A comparison reveals a significant improvement in the close-in phase noise of the presented MEMS oscillators built using the coupled ring resonators compared to their temperature compensated counterparts on account of higher resonator Q with a lower motional impedance. This is achieved due to the optimized placement of the oxide within the resonator volume. However, the noise

floor of the measured MEMS ring oscillators is slightly degraded as compared with [50], most likely due to the lower drive power used.

Table 3-1: Comparison of measured phase noise (PN) for temperature-compensated oscillators operating between 1 to 100 MHz in literature.

Ref	**Actuation (Resonator frequency)**	**Compensation Strategy**	**Measured frequency shift (ppm)**	**PN @ 1KHz (normalized to 10 MHz)**	**PN (floor)**
[51]	Electrostatic (6 MHz)	Temp sensor (parabolic)	39 ppm (25 to 125 °C)	-112 (-107.5)	-135
[52]	Piezoelectric (81 MHz)	Passive using oxide	120 ppm (20 to 70 °C)	-72 (-90.2)	-135
[50]	Piezoelectric (26.7 MHz)	Passive using oxide	83 ppm (-20 to 100 °C)	-101 (-109.5)	-150
This work	Piezoelectric (19.5 MHz)	Passive using oxide	100 ppm (-40 to 85 °C)	**-115 (-120.8)**	-140

The timing jitter or the relative perturbation of the period of the output can be directly correlated with the phase noise measurement [1]. From the data in Figure 3-6, we can estimate the timing jitter to be 58.26 ps RMS taking a full bandwidth of 20 MHz. Between 20 kHz to 20 MHz, the timing jitter is reduced to 5.17 ps RMS and shows that the timing uncertainty is dominated by the relatively large close-in phase noise of the oscillator, dominated by the low Q of this particular resonator. Improving the resonator Q, while ensuring a large driving power, can enable a significant reduction in the oscillator phase noise and thus enable precision timing references.

3.6 System Implementation

3.6.1 Oscillator Temperature Dependence

In order to estimate the values of the *k* multipliers, it is essential to characterize the temperature dependence of three compensated oscillators. The oscillators shown in Figure 3-4 and Figure 3-5 are characterized for their temperature dependence across -15 °C to +55 °C and the result is presented in Figure 3-7.

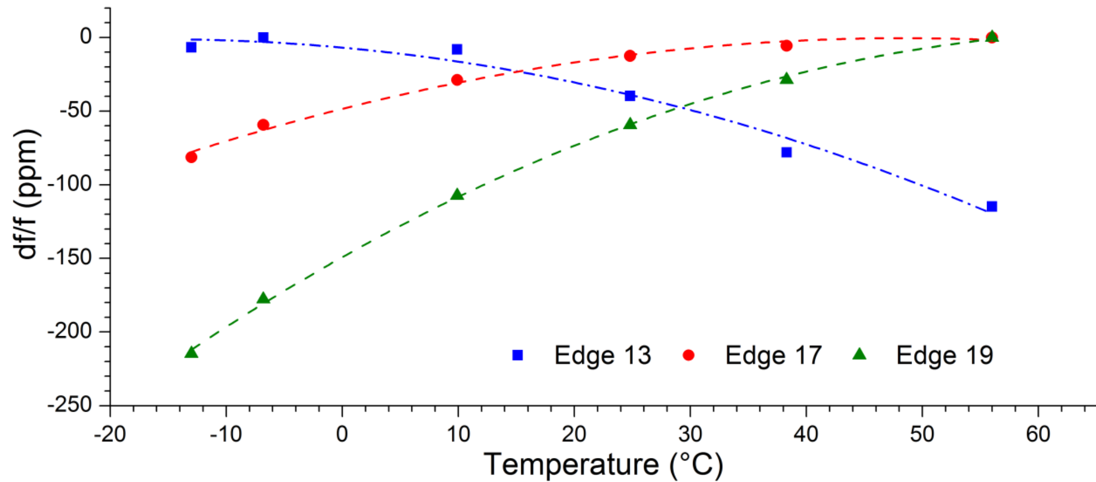

Figure 3-7: Measured relative frequency shift (df/f) as a function of temperature for the three oscillators shown in Figure 3-5. Solid symbols are used to represent the measured data points and the dashed lines represent the least squares fit to the measured data, the equations of which are used in the calculation of the *k* multipliers.

The measured result in Figure 3-7 includes the temperature induced fluctuations in the oscillator circuit (amplifier and passive components) in addition to the resonator TCF. The solid symbols in Figure 3-7 represent the measured data points while the dashed lines represent the second-order least squares fit to measurement. In the system, the three oscillators will provide the three frequency sources which will be manipulated in accordance with the proposed algorithm to generate the final output.

3.6.2 Estimation of system multipliers

From the measured temperature induced frequency shift of the oscillators, we can extract their coefficients a, b and c using best fit to Equation 3-1. Table 3-2 summarizes these numbers for the oscillators presented in Figure 3-5 and Figure 3-7. From the extracted coefficients in Table 3-2, and using Equation 3-3 and Equation 3-4, we can calculate k_1 to be 1.8139, k_3 as 1.6284 and k_{12} as 4.9974.

Table 3-2: Extracted coefficients $a, b,$ and c for the three oscillators shown in Figure 3-5 and Figure 3-7.

Edge (μm)	**Measured Turnover Temperature (K)**	**Fitted Coefficients**		
		a	**b**	**c**
13	363	-0.451535	232.430428	19,548,962
17	335	-0.399286	256.636615	19,425,565
19	273	-0.615163	421.611049	19,337,542

3.6.3 Clock Measurement Results

In order to obtain a measurement of the clock output, we need to enable both frequency multipliers and mixers and set their parameters for the given k numbers. In this proof-of-concept demonstration, the frequency multiplication is performed using an Analog Devices fractional phase locked loop (n-PLL) AD 9552 evaluation board (Analog Devices, *inc.*, Cambridge, MA). This evaluation board allows us to obtain fractional frequency multiplication with sufficient accuracy for the current clock requirements. Frequency mixing is obtained using another evaluation board from Analog Devices incorporating the AD 0831 low-frequency mixer chipset. Figure 3.8

shows a schematic depiction of the complete system. In the complete system, three sets of PLLs and mixers are required to generate the Stage I and Stage II outputs.

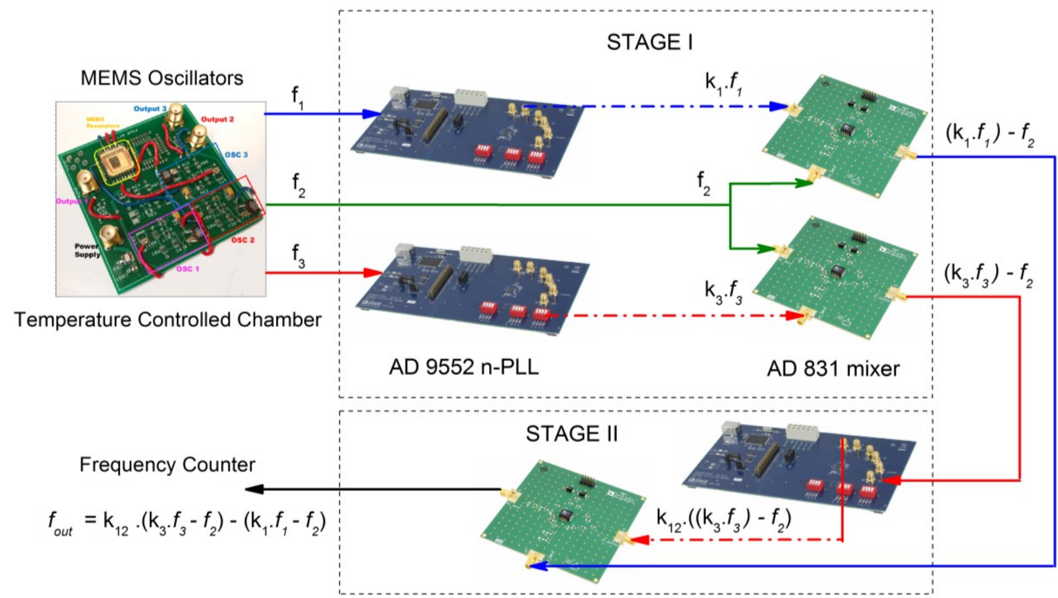

Figure 3-8: Schematic of the full clock system implemented using discrete circuit boards.

In order to obtain a measurement of the system output, the components are connected in accordance with the schematic shown in Figure 3-8. The frequency multipliers are set using the Analog Devices software for the PLLs, and the mixer output is filtered using low pass RC filters. With this, the clock frequency is measured using an Agilent 53181A frequency counter as the system temperature is varied from -20℃ to +50℃. The final frequency of the clock with temperature is plotted in Figure 3-9. The total integration time for the measurement is 0.3 seconds, which translates into a counter measurement uncertainty of ~ 0.4 ppm. Figure 3-10 plots the temperature dependence of the individual oscillators along with that of the final system for comparison.

From the measured result, we notice that the output has some non-idealities and we have a total temperature induced frequency shift of ~8 ppm across -20℃ to +50℃. Nevertheless, this system implementation demonstrates more than 10× improvement in the clock temperature stability as compared to the individual temperature-compensated oscillators (Figure 3-10).

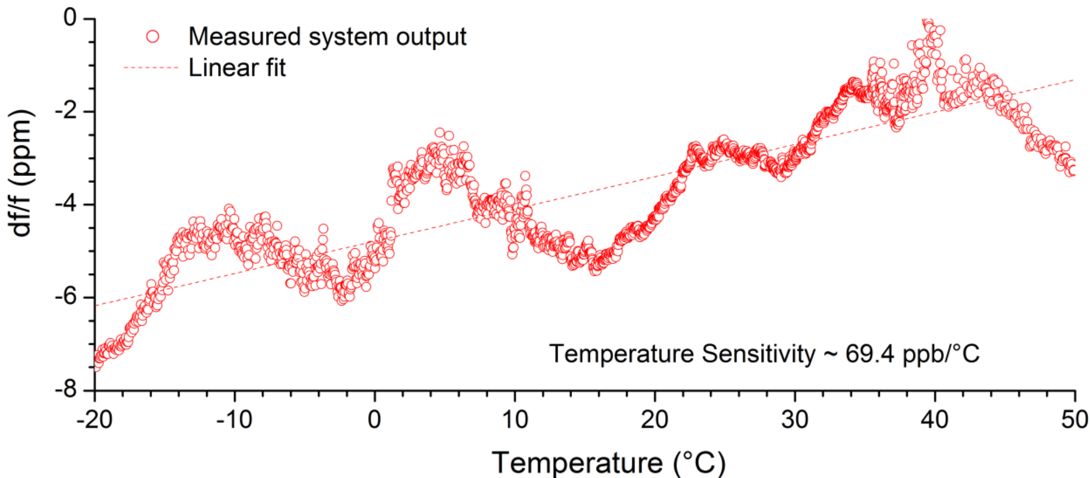

Figure 3-9: Measured clock output using the oscillators shown in Figure 3-7 and the system shown in Figure 3-8. The uncertainty in the counter frequency measurement is ~ 0.4 ppm.

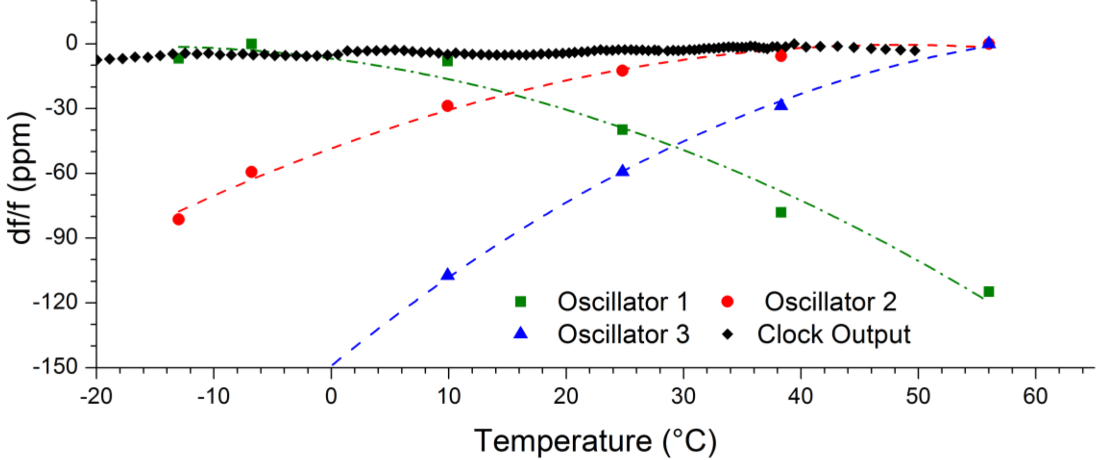

Figure 3-10: Measured temperature dependence of the individual oscillators along with that of the final system for comparison.

From the presented analysis in Section 3.3 we recall that the clock output may show some temperature dependence of frequency due to measurement errors during

the calibration run. Since the measured result in Figure 3-9 shows a small linear frequency dependence on temperature, we can say that this non-ideal response is primarily due to the erroneous measurement of the oscillator temperature. In the present setup we note that the oscillators are suspended in a vacuum chamber where the temperature is controlled to be within ± 0.1 °C of the set temperature. However, due to low-vacuum operation, the suspended oscillator circuit has a large thermal resistance to the temperature controlled chuck in the chamber, and thus we have a large temperature difference between the oscillators and the chuck. In order to allow for a reasonable estimate of the oscillator temperature during the calibration run, an external thermistor was mounted on the PCB close to the resonator die. From the measured non-ideal clock output, it seems that the thermal coupling between the thermistor and the resonator needs further improvement in order to improve the clock thermal stability. A potential solution could be to utilize an uncompensated resonator on the same die as a temperature sensor to better extract each oscillator temperature response.

From the results in Figure 3-9, a second and potentially critical challenge of frequency drift is noted. The final system output shows a ±1 ppm drift in addition to the small linear frequency dependence. The likely causes could be drift of the individual oscillators apart from temperature fluctuations in the system, or higher order TCF values of the oscillators, which are not accounted for in the three-resonator system. More measurements and analysis will be required before determining the primary cause of these frequency fluctuations.

3.7 Discussion

Due to their relatively large surface to volume ratios, micromachined resonators are prone to surface contamination which makes unpackaged resonators susceptible to hysteresis and frequency fluctuations [53]. Such effects can be mitigated through the use of appropriate packaging technologies. MEMS packaging techniques to achieve hermetic sealing has been widely investigated in literature and commercially available MEMS resonators have been packaged either through the use of capping wafers [54] or by using epitaxially grown poly-silicon [33]. Given the materials used for the AlN-on-silicon resonators presented in this thesis, a wafer capping technique using a low temperature Au-Si eutectic bond is most suitable [55]. Resonator burn-in may also be necessary to achieve stable device performance with improved long term frequency stability [56].

From the measured phase noise of the oscillator seen in Figure 3-6 and its calculated jitter, we note the need to implement the clock using resonators having a higher resonator Q. While the noise floor can be improved through the use of low noise circuit components and increasing the drive power, improvement in the close-in phase noise will require higher device-Qs [8]. From the measured results of multiple ring resonators (Figure 3-11), we note that the resonator Q remains relatively unchanged as a function of the temperature compensation design. These results along with a very high estimation of the intrinsic Q and a large simulated anchor Q (> 700,000) point towards interface loss being the primary cause of the measured Q degradation. While there has been some theoretical analysis of interface losses [31], no experimental data exists to verify their conclusions. A careful experimental study

of the interface loss mechanism is necessary to understand the nuances to enable piezoelectric resonators with improved Q.

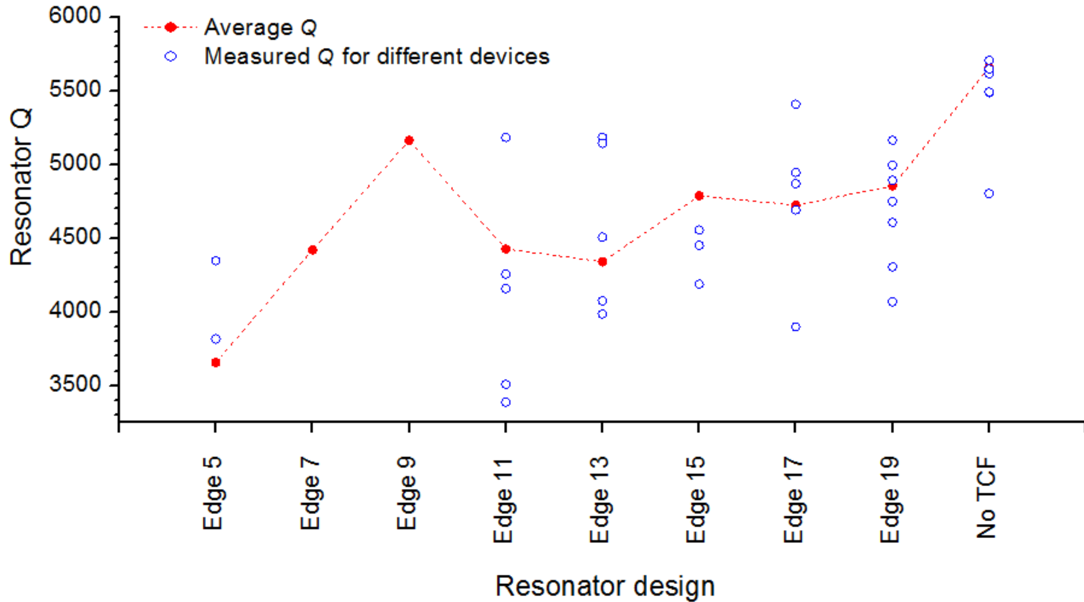

Figure 3-11: Measured Q for different ring resonators as a function of its temperature compensation design. The 'edge' labels indicate the distance of the oxide from the resonator edge. The 'No TCF' label indicates the uncompensated device without any oxide rings.

In summary, this chapter includes the following research contributions:

- Demonstration of a novel temperature-insensitive clock utilizing multiple resonators with unique temperature-frequency response.
- Analysis of the clock algorithm for potential errors arising from calibration errors and resonator drift.
- Demonstration of a proof-of-concept system with temperature drift of less than 8 ppm across -20 °C to +50 °C.

Chapter 4 EXPERIMENTAL INVESTIGATION OF LOSS MECHANISMS IN LAMÉ-MODE RESONATORS

The $f\times Q$ for a material, which is set by the dynamics and interactions of phonons is believed to set an upper limit on the Q of the micromechanical resonators made out of that material [24], [25]. Experimental investigation of resonators made from single material systems seem to agree well with the published material $f\times Q$ limit [24]. However, inclusion of secondary materials, either metal layers for piezoelectric actuation or silicon dioxide for temperature compensation has shown to cause a significant degradation in the resonator Q [31], [34]. As a case in point, the measured Q in Chapter 2 for the coupled-ring resonators is far from the $f\times Q$ limit for both silicon and AlN. Even in published literature, data on piezoelectrically-actuated AlN-on-silicon [34], AlN [57], GaN-on-silicon [58] and GaN [18] resonators suggest that the upper limit on the resonator Q is much less than 20,000 and is seen to be independent of the resonator operating frequency, favoring operation at higher frequencies for increased f×Q value. As a consequence, piezoelectric and piezo-on-substrate resonators achieving $f\times Q$ product close to the theoretical limit tend to operate at very high frequencies, typically greater than 1 GHz [20], [59]. In contrast to quartz-based resonators, these piezoelectric resonators have metal thickness on the order of the thickness of the piezoelectric layer. This has led to the hypothesis of interface losses setting the limit on the resonator Q in such thin-film piezoelectric devices.

In order to study the effect of interfaces on resonator performance, a careful study utilizing Lamé-mode resonators is implemented. The choice of Lamé-mode is made as these resonators have been shown to provide very high $f{\times}Q$s at low operating frequencies [60], [61], [62]. Lamé-mode is isochoric *i.e.* has no change in volume during resonance and is thus immune to thermoelastic damping, which is known to limit the Q of silicon resonators at low frequencies (less than 5 MHz) [25]. Table 4-1 summarizes the reported Q of silicon Lamé-mode resonators.

Table 4-1: Published measured data for electrostatically-actuated Lamé-mode resonators. The $f{\times}Q$ limit in silicon is estimated to be 2.2×10^{13} [24].

Ref.	**Image**	**Size (μm^2)**	***f*** **(MHz)**	***Q*** **(millions)**	***f×Q (×10^13)***
[60]		800 × 800	5.16	2.24	1.155
[61]		650 × 650	6.35	1.58	1.0
[62]		320 × 320	12.9	0.76	0.98
This work		600 × 600	6.36	1.4	0.89

This experiment attempts to study the effect of interfaces on the performance of Lamé-mode resonators. Silicon only electrostatically-actuated Lamé-mode resonators are used to establish the base device performance. They are also used to validate the anchor loss simulation method through experimental demonstration of resonator Q as a function of tether geometry. The electrostatic Lamé-mode resonators are subsequently temperature-compensated through the inclusion of silicon dioxide in the structure. Characterization of these resonators allows us to study the effect of lateral (oxide-silicon) interface on the resonator performance. In the final step, temperature-compensated piezoelectrically-actuated resonators are fabricated to study the effect of vertical interfaces (metal-AlN-metal-silicon) on the resonator Q.

4.1 Electrostatically Actuated Lamé-Mode Resonators

4.1.1 Device structure

The device is designed using a 100 µm × 100 µm silicon plate. Straight tethers are used to support the plate resonator. Figure 4-1 shows an SEM image and close-in schematic of the Lamé-mode resonator used in this demonstration [12].

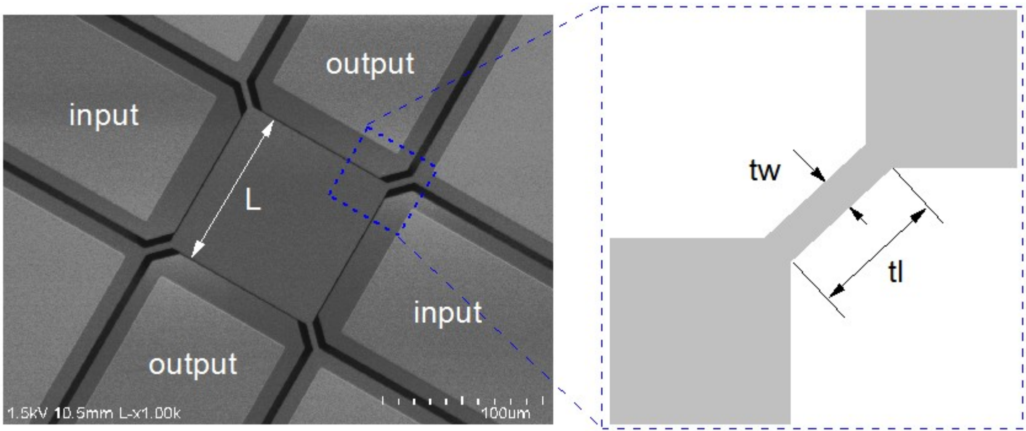

Figure 4-1: A SEM image of a fabricated electrostatically-actuated Lamé-mode resonator. The close-in schematic on the right identifies the tether geometry variables.

The fundamental Lamé-mode frequency is determined by the velocity of the shear wave in the device and the plate geometry through,

$$f_{Lamé} = \frac{1}{\sqrt{2}\,L}\sqrt{\frac{G}{\rho}}, \qquad \text{Equation 4-1}$$

where L is the length of the square plate, G is the shear modulus of elasticity and ρ is the density of the resonating plate.

4.1.2 Estimation of anchor loss

Anchor loss, also known as clamping loss, has been widely investigated in a variety of resonator geometries due to its significant effect on the resonator performance [30], [63]. Since anchor loss is geometry dependent, it can be minimized

through appropriate design choices and hence it is critical to eliminate for the realization of high-Q resonators.

Analytical models estimating the clamping loss in simple beam geometries have been presented in literature [30]. Recently, more exotic ring resonators have also been analyzed for their substrate damping effects [63]. Unfortunately, most of these analytical estimates require precise knowledge of the stress profile at the anchoring area, which is difficult in the case of complex resonator geometries. In addition, they involve the use of fitting parameters, which need to be extracted from measured results. Recognizing this limitation, a significant effort has been put towards the estimation of anchor Q using finite element methods. Bindel *et al.* applied the method of perfectly matched layers (PML) to the problem of anchor dissipation in stem-supported disk resonators [32], motivated by their utility in electromagnetic analysis [64]. Since then, there has been additional work validating the PML-based approach for anchor Q estimation [65]. In both these works, the finite element analysis has been implemented using custom built codes, making it difficult to generically adopt. In this work, COMSOL® [66], a commercial software package, is utilized to model the anchor loss in resonators.

In order to perform a preliminary verification of this approach, the simulation parameters in COMSOL® are chosen such that the simulated anchor Qs match reported analytical estimates of anchor Q for different beam modes presented in [30]. Figure 4-2 shows the finite element model of a beam using a PML to model the substrate as a semi-infinite layer. The material parameters for the PML are the same as those for the substrate layer, which are typically the same as that for the beam. It

should be noted that the parameters of the PML are critical in achieving accurate anchor Q estimates. Similar to the observations in [65], the choice of alpha, *i.e.* the PML scaling factor, determines the magnitude of the simulated anchor Q and should be optimized for the resonator frequency and hence the geometry that is analyzed. This idea is elaborated in Figure 4-3, which shows a large variation in the simulated Q as a function of alpha.

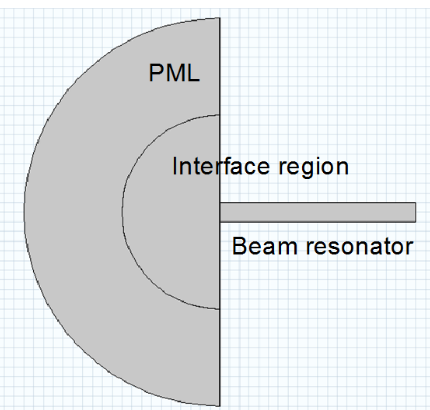

Figure 4-2: Model of a beam resonator for anchor loss estimation. The interface region ensures a smooth transition from the beam to the highly attenuating PML region.

From Figure 4-3, we can clearly see that the minimum value of the estimated anchor Q converges to the analytical estimate from [30]. A similar study is performed for all the beam geometries and modes analyzed in [30]. The results are summarized in Table 2-2, demonstrating an excellent agreement between the analytical and the FEM estimates of the anchor Q. Having verified the applicability of the simulation model with data from literature, we can use the same approach to predict the anchor loss in Lamé-mode resonators.

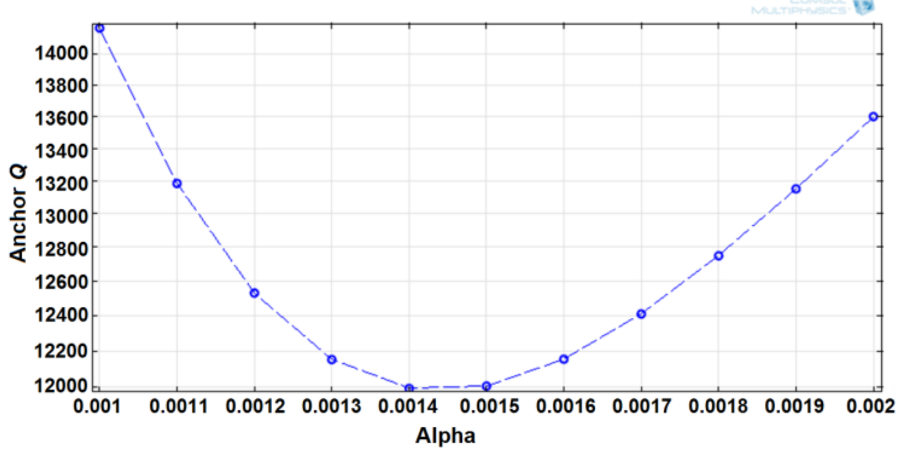

Figure 4-3: Simulated anchor Q for a silicon beam resonator as a function of alpha. The silicon beam is 500 µm long and 7.2 µm wide. The analytical estimate of anchor Q for the third-order flexural mode (clamped-clamped boundary) is calculated to be 11,177 [30].

4.1.3 Optimization of tether geometry for Lamé-mode resonators

In order to optimize the tether geometry for reduced anchor loss, the PML based model is used to estimate the anchor Q as a function of the tether length keeping the tether width fixed. Figure 4-4 shows the simulated anchor Q for tether lengths ranging from 2.5 µm to 20 µm for a 2 µm tether width.

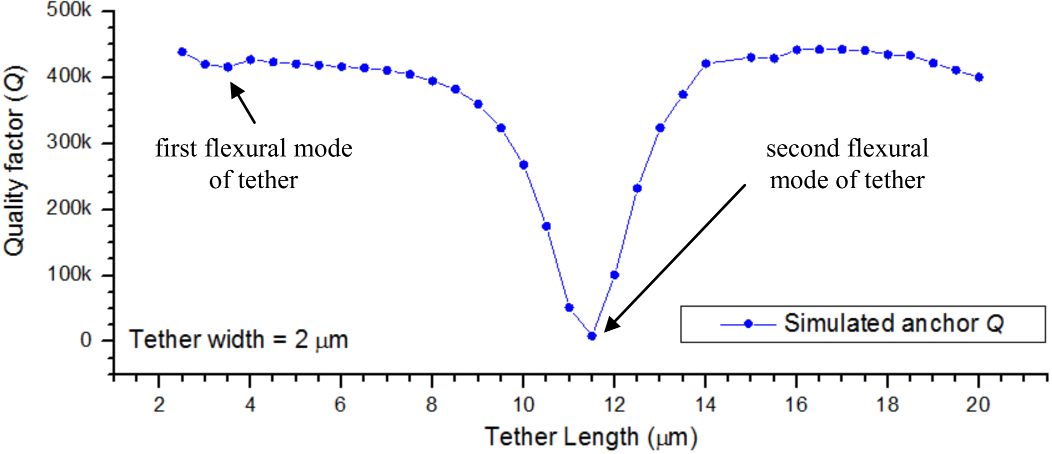

Figure 4-4: Simulated anchor Q as a function of the tether length for a 100 µm × 100 µm Lamé-mode resonator. The total simulated Q is calculated using the simulated anchor Q and the phonon-phonon $f \times Q$ limit in silicon as 2.2×10^{13} [24]. The simulated frequency for these designs is ~ 41.5 MHz. The two local Q minima's in the plot correspond with the first two flexural modes of the supporting tether equaling the Lamé-mode frequency.

Table 4-2: Comparison of the simulated anchor Q with analytically calculated estimates for flexural modes of a silicon beam resonator [30].

Length (µm)	**Width (µm)**	**Frequency (kHz)**	**Anchor Q** *Analytical*	*Simulated*	**Error (%)**
			Fixed Free Cantilever (first-order flexure)		
700	6.45	15.94	2.6626×10^6	2.65×10^6	0.47
500	4	19	4.0684×10^6	4.1×10^6	-0.98
500	5	24.59	2.083×10^6	2.1×10^6	-0.96
500	6.2	30.14	1.0925×10^6	1.1×10^6	-0.91
			Fixed- Fixed Beam (first-order flexure)		
900	7.9	74.8	248,470	247,612	0.34
700	5.15	80.3	421,980	419,165	0.47
500	3.8	117	382,800	380,418	0.52
300	3.4	288.4	115,440	115700	-0.26
			Fixed- Fixed Beam (third-order flexure)		
700	8.7	740	17,365	18,940	-9.07
500	6.1	1030	18,357	20,061	-9.28
500	7.2	1210	11,177	11,976	-7.15

4.1.4 Origin of anchor loss in Lamé-mode resonators

In order to support the Lamé-mode resonance, the tethers are required to undergo forced flexural vibrations. As a consequence, the anchor loss in such resonators is strongly dictated by the in-plane flexural resonance frequency of the tether, which can be expressed as

$$f_n = \frac{1}{2\pi} \beta_n^2 \frac{t_w}{t_l^2} \sqrt{\frac{EI}{\rho A}}, \qquad \text{Equation 4-2}$$

where f_n is the resonance frequency of the nth order resonance mode, β_n is the mode constant, t_w is the tether width (µm), t_l is the tether length (µm), E is the Young's

modulus (Pa), I is the area moment of inertia for the tether cross-section (m^4) and A is the cross-section area of the tether (m^2).

For a cantilever attached with a mass at its free-end, the resonance frequency is known to be loaded and can be estimated using the formulation in [67]. The effect of mass loading is accounted for by lowering of the mode constants, which affects the resonance frequency through Equation 4-2. Table 4-3 lists the mode constants and the critical tether length at which the flexural resonance frequency for the tether equals the frequency of the fundamental Lamé-mode of a 100 μm × 100 μm square plate, when the tether width is fixed at 2 μm.

While the results agree well for longer tether lengths, at shorter tether lengths, the tether aspect ratio is much smaller than 10:1 and the Euler-Bernoulli approximation introduces significant inaccuracies. The FEM simulation results for the Lamé-mode and the first two flexural modes of the tether along with the associated tether lengths are shown in Figure 4-5.

Table 4-3: Analytically estimated critical tether length for a 100 μm × 100 μm Lamé-mode resonator.

	β	**Critical tether length (μm)**	
		Analytical	**Simulated**
Mode 1	0.425	1.44	3.5
Mode 2	3.925	13.34	11.5
Mode 3	7.065	24.01	23
Mode 4	10.215	34.72	34

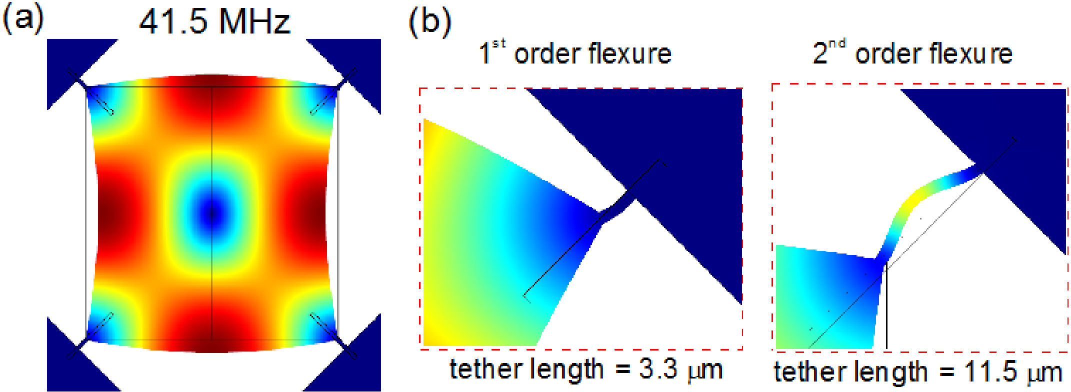

Figure 4-5: (a) Simulated Lamé-mode for a 100 μm square plate. (b) First two flexural modes of the supporting tether equaling the frequency of the Lamé-mode, at tether lengths of 3.3 μm and 11.5 μm. These two tether lengths correspond with the two minima's in the simulated anchor Q plot in Figure 4-4.

4.1.5 Experimental Verification

In order to experimentally verify the predictions in Figure 4-4, capacitively-actuated Lamé-mode resonators having a characteristic length of 100 μm are fabricated using the process flow shown in Figure 4-6. As has been discussed in the beginning, the choice of capacitive actuation was made to ensure that the resonator Q is not affected due to interface losses and/or metal loading.

The fabricated devices are measured in a Lakeshore vacuum probe station for their performance characterization. Figure 4-7 shows the comparison between measured and simulated Q for three different dies. An excellent agreement is seen between the two, which serves to validate the anchor loss simulation method.

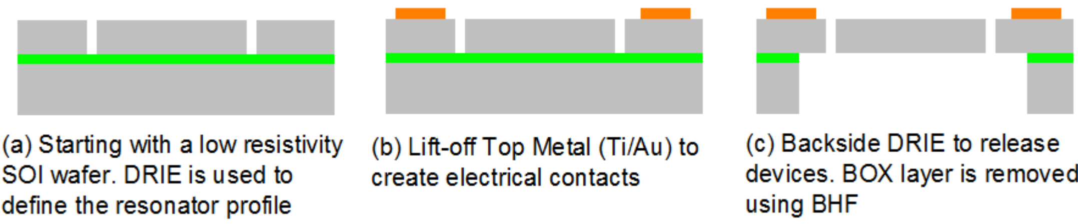

Figure 4-6: Process flow used to fabricate the capacitively transduced Lamé-mode resonators.

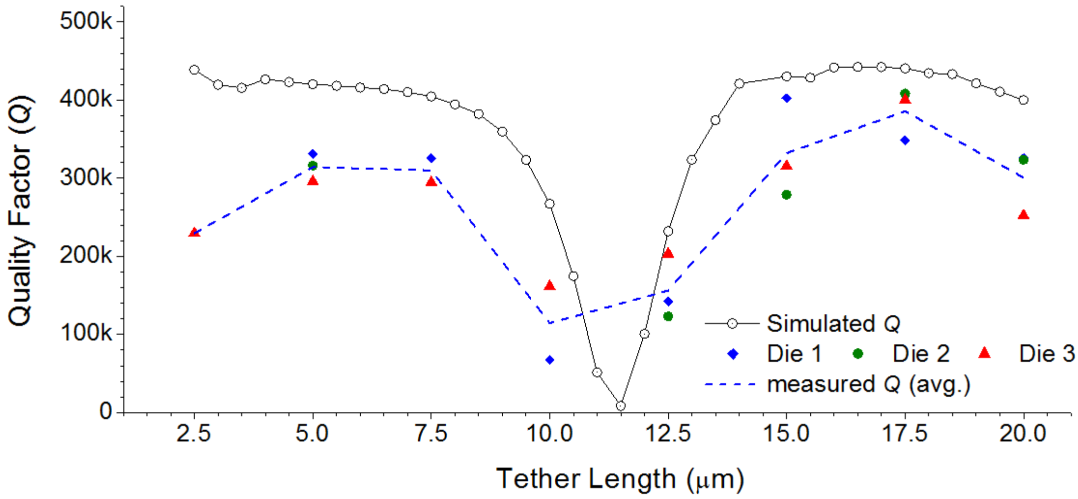

Figure 4-7: Comparison of the measured resonator Q for three different dies with the simulated Q for the 100 μm × 100 μm Lamé-mode resonators.

Figure 4-8 shows the measured frequency response of a high-Q Lamé-mode resonator. This device shows a Q of 302,120 at a center frequency of 41.5 MHz with an $f{\times}Q$ of 1.25×10^{13}, one of the highest reported to date with silicon [24]. As can be expected from Figure 4-4, this resonator has a tether length of 17.5 μm with a tether width of 2 μm. The frequency response measurement using a network analyzer gives the loaded Q of the resonator and using the extraction method in [68], the unloaded Q of the resonator can be calculated to be 408,270. This yields an even higher $f{\times}Q$ of 1.7×10^{13} for the device shown in Figure 4-8. This device serves as the reference to estimate the Q loading from the various interfaces, arising from temperature compensation and piezoelectric actuation.

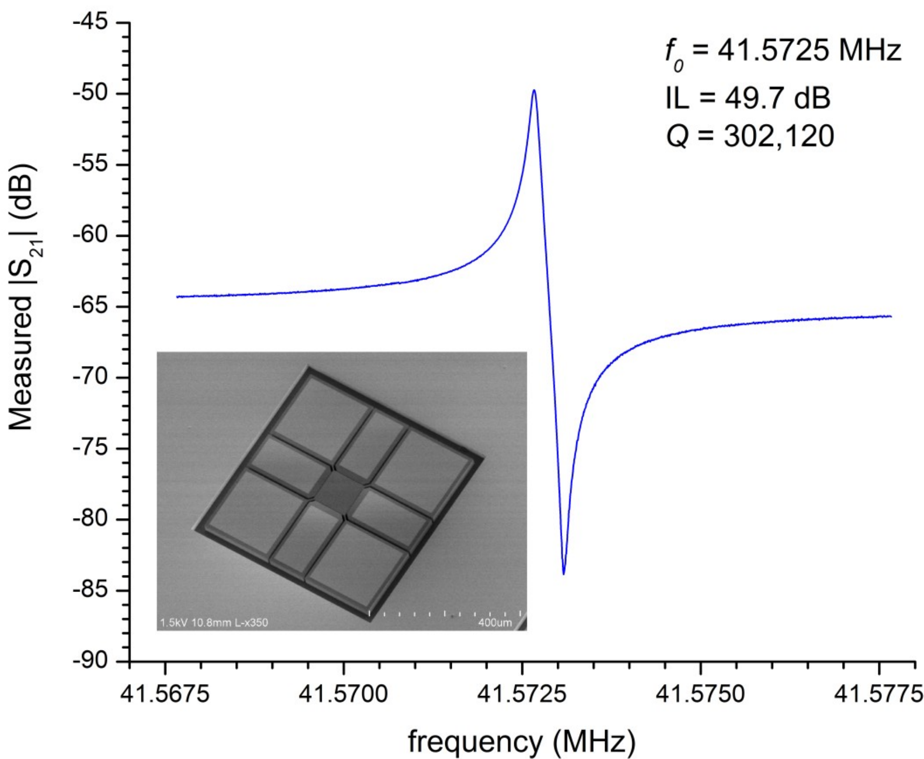

Figure 4-8: Measured response of a high-*Q* Lamé-mode resonator with tether length of 17.5 μm and tether width of 2 μm. A DC bias of 250 V was applied during measurement. (Inset) A SEM image of the resonator.

4.2 Temperature Compensation of Lamé-Mode Resonators

In Chapter 2, we described our passive compensation technique and applied it to both flexural-mode and coupled ring resonators. It was shown that the location of oxide-refilled trenches was important for the efficient temperature compensation of silicon resonators. A similar approach has been used for the compensation of the Lamé-mode resonators. Figure 4-9 shows a model of the proposed temperature-compensated structure identifying the location of the oxide-refilled regions within the resonator body. While, the Lamé-mode of a pure material does not suffer from thermoelastic damping, the inclusion of material interfaces due to the oxide-refilled trenches creates asymmetries leading to thermoelastic damping in the structure [17], [42].

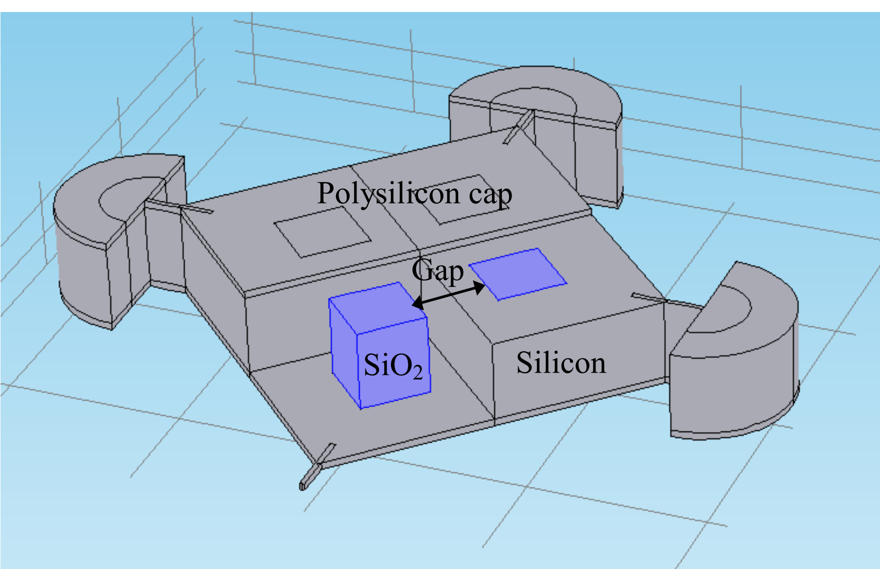

Figure 4-9: Representative schematic showing the location of the oxide-refilled trenches embedded within the silicon Lamé-mode resonator. The simulated thermoelastic damping dependent *Q* and anchor *Q* for this design are 2.37×10^6 and 0.71×10^6, respectively.

From the origin of anchor loss in Lamé-mode resonators discussed in Section 4.1.4, it is expected that the optimum tether geometry will be changed depending on

the location of the oxide islands. Due to presence of silicon dioxide in the resonator, the center frequency reduces due to the lower shear wave velocity in the silicon-silicon dioxide composite structure. As a consequence, the tether length for optimized anchor loss is shorter. Using the validated FEA models, the passively compensated Lamé-mode structures are optimized for reduced anchor loss and thermoelastic damping. The optimized designs consist of four oxide-refilled islands each 20 µm × 20 µm in size with tether length of 10 µm, optimized for maximum anchor *Q*. The distance between the trenches, denoted with 'gap' in Figure 4-9 determines the turnover temperature for the compensated resonator. Figure 4-10 plots the simulated temperature-induced frequency shift in ppm for four different gap sizes.

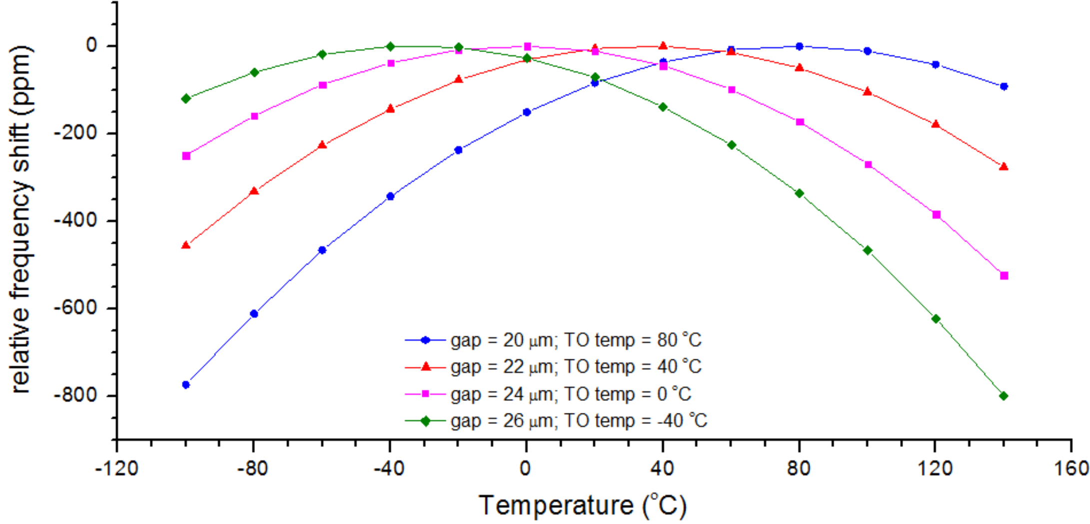

Figure 4-10: Temperature dependence of frequency for four designs with different spacing (gap) between the oxide-refilled trenches. The four designs have turnover (TO) temperatures of -40 °C, 0 °C, 40 °C and 80 °C, respectively. Thus, it is clear that by changing the gap, we can change the turnover temperature, without modifying the process parameters.

4.2.1 Fabrication process of temperature-compensated capacitive Lamé-mode resonators

To enable electrostatic actuation of the resonators, the device is made from a low-resistivity (0.01-0.02 Ω-cm) device layer of an SOI wafer. In the first step, a number of trenches for oxide islands are defined in the device layer using DRIE (Figure 4-11(a)). Care is taken to ensure that the trenches do not go all the way to the BOX layer. The number of trenches (n=10), the trench width (~ 1.2 μm) and the trench spacing (~ 0.8 μm) determine the required thermal oxidation thickness (~ 2 μm) and also sets the final width of the oxide-refilled region (~ 20 μm). Using wet thermal oxidation, the free standing silicon beams (between the trenches) are converted into silicon dioxide. It is very likely that the trenches are not completely filled at the end of the oxidation step. Low Pressure Chemical Vapor Deposition (LPCVD) of oxide (~300 nm) can be used to fill any remaining gaps in the trench region (Figure 4-11(b)). The wafer is subsequently polished using CMP to remove the surface oxide and to planarize the area over the trenches. A thin layer of polysilicon (1 μm) is deposited using LPCVD to enclose the oxide-refilled trenches within the body of the silicon resonator (Figure 4-11(c)). Using DRIE, the resonator contour is defined and this also sets the capacitive actuation gap (~ 1.3 μm) (Figure 4-11(d)). If required a thin layer of thermal oxide can be grown and removed using BHF to smoothen the sidewall scalloping obtained as a consequence of DRIE. A 100 nm thick metal layer (Cr/Au) is lift-off patterned to create the contact pads. Before depositing the metal layer, the high resistivity polysilicon layer is etched using DRIE (Figure 4-11(e)). Finally, the devices are released from the back using DRIE. The BOX layer can be

removed using either BHF or plasma etching (Figure 4-11(f)). Figure 4-12 shows a microscope image of a temperature-compensated Lamé-mode resonator. Note that, since the trenches are enclosed under the polysilicon layer, SEM images do not show the presence of trenches.

Figure 4-11: Fabrication process flow for the temperature-compensated Lamé-mode resonators.

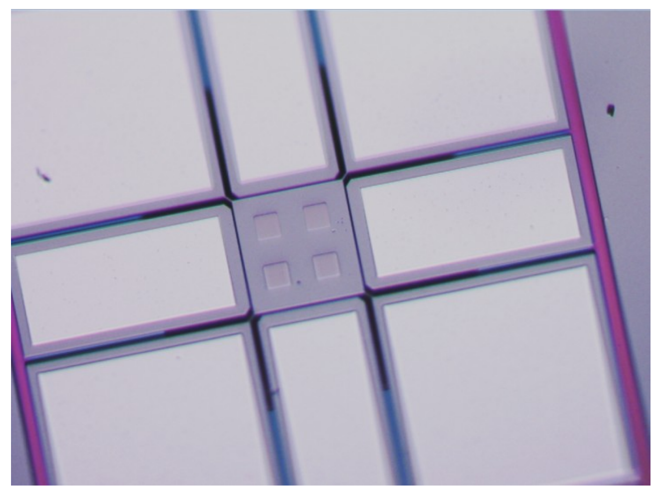

Figure 4-12: A microscope image of a temperature-compensated Lamé-mode resonator. The four oxide-refilled square trenches can be clearly seen through the polysilicon cap layer.

4.2.2 Measured Results

Figure 4-13 shows the measured frequency response of a temperature-compensated Lamé-mode resonator. This resonator demonstrates a Q of 96,600 at a center frequency of ~38.4 MHz. The resonator is connected to the anchors via tethers that are 2 μm wide and 10 μm long. Apart from the inclusion of the oxide islands, these resonators have another modification from the first run: a 1 μm polysilicon on top of the resonator to form a protective cap on the oxide islands. As a comparison, the measured result of the optimum uncompensated resonator with the 1 μm polysilicon layer is shown in Figure 4-14.

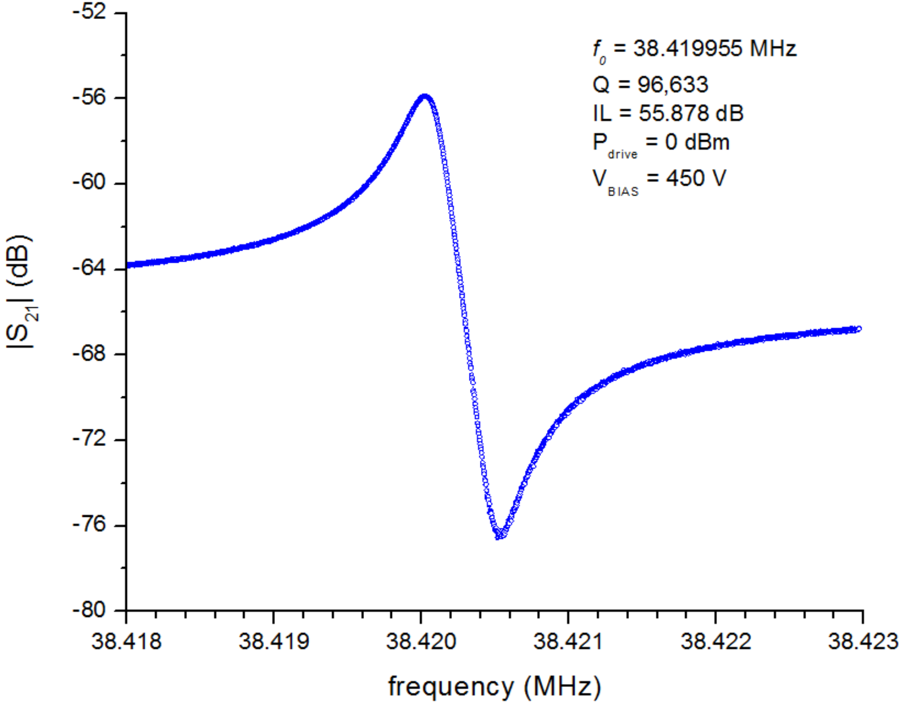

Figure 4-13: Measured frequency response of a temperature-compensated Lamé-mode resonator. This resonator has a tether length of 10 μm and a tether width of 2 μm.

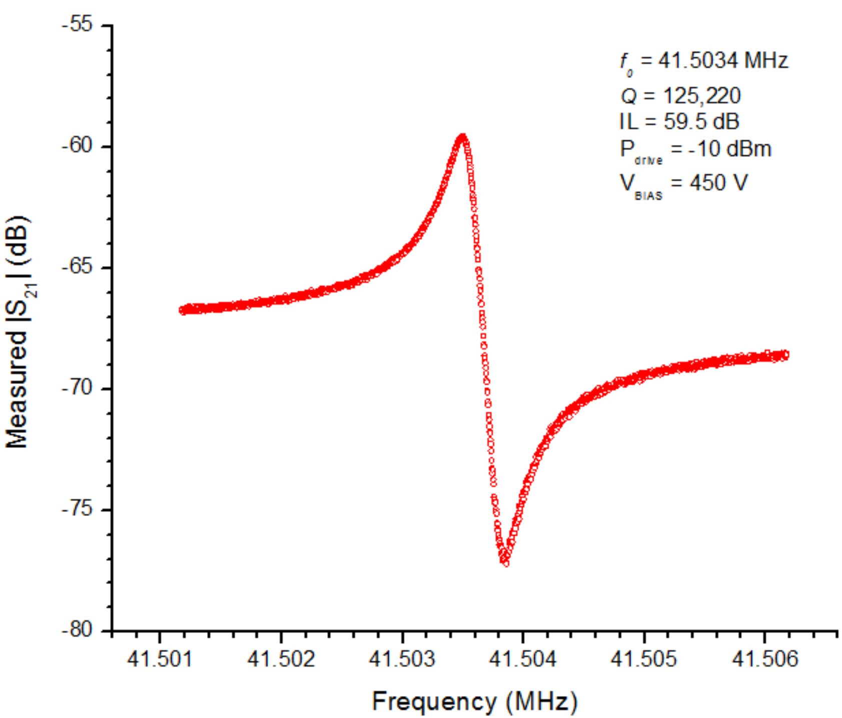

Figure 4-14: Measured frequency response of an uncompensated Lamé-mode resonator. This resonator has a tether length of 17.5 μm and a tether width of 2 μm. While the planar geometry is same as for the result presented in Figure 4-8, this device includes a 1μm polysilicon layer over the low-resistivity silicon device layer. The reduced Q as compared to Figure 4-8 may be due to the inclusion of a 1 μm polysilicon capping layer, amongst other factors.

The temperature dependence of center frequency for these resonators is characterized using a Lakeshore cryogenic vacuum probe station. Figure 4-15 plots the measured frequency shift as a function of temperature for four compensated resonators with varying 'gap' between the oxide-refilled trenches. From Figure 4-15, it can be clearly seen that by changing the 'gap' between the oxide-refilled trenches the turnover temperature can be tuned across a wide range. However, it is also seen that the turnover temperatures are much lower than the designed values shown in Figure 4-10. In order to understand the cause of this discrepancy, cross-section SEM images were taken. Figure 4-16 (a) shows a SEM image of a temperature-compensated

resonator. The depth of the oxide-refilled trenches is ~ 20 μm as compared to the designed 24 μm. This implies that the volume of oxide is ~ 17% lower than the designed volume and can explain this shift in the turnover temperatures. Figure 4-16 (b) shows a close-in view of the refilled trenches.

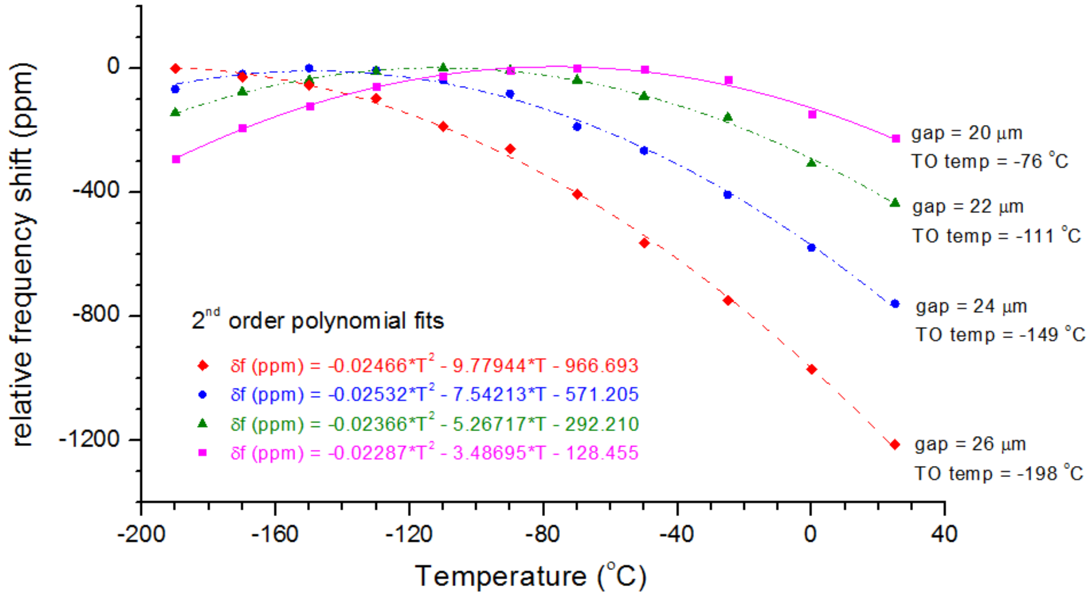

Figure 4-15: Measured temperature dependence of frequency for four different temperature-compensated Lamé-mode resonators each having a different 'gap' between oxide-refilled trenches. Thus, we can tune the turnover temperature by varying the 'gap' between the oxide-refilled trenches.

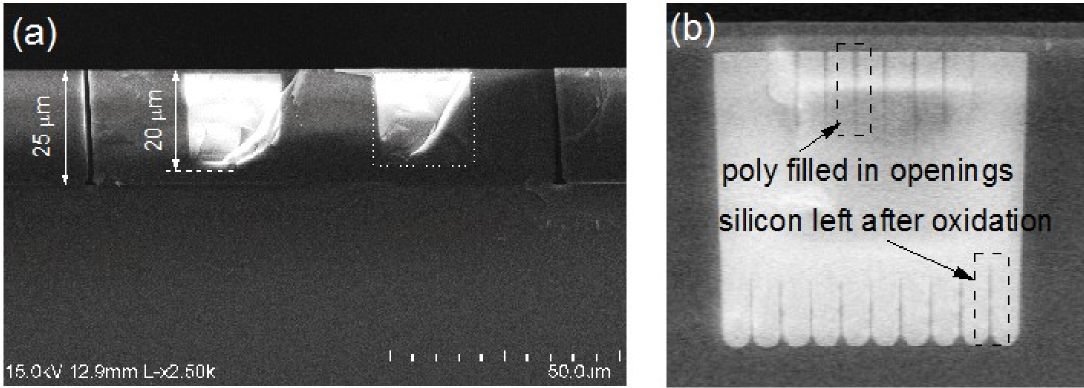

Figure 4-16: (a) A cross-section SEM image of a temperature-compensated Lamé-mode resonator. The depth of the oxide-refilled trenches (~ 20 μm) can be clearly seen in this image. (b) Close-in SEM view of the oxide-refilled trench. Small silicon regions are visible in between the refilled oxide.

To study the effect of silicon dioxide on the resonator Q, multiple devices are measured with varying amount of temperature compensation and the results are shown in Figure 4-17. As the effect of silicon dioxide in the resonator is increased through a reduced 'gap', its center frequency is expected to decrease due to the increasing contribution of oxide. From Figure 4-17 we can see an increase in Q loading as the frequency is decreased. All resonators in Figure 4-17 have an optimized tether length of 10 μm with a tether width of 2 μm. One point to note here is that the tether geometry is optimized for fully compensated resonators, having a center frequency between 36 to 37 MHz and not for the devices in Figure 4-17, which show a frequency between 37.4 to 38.6 MHz. As a result, any contributions from anchor loss should be reduced with optimum refilled trench geometry potentially yielding higher device Q.

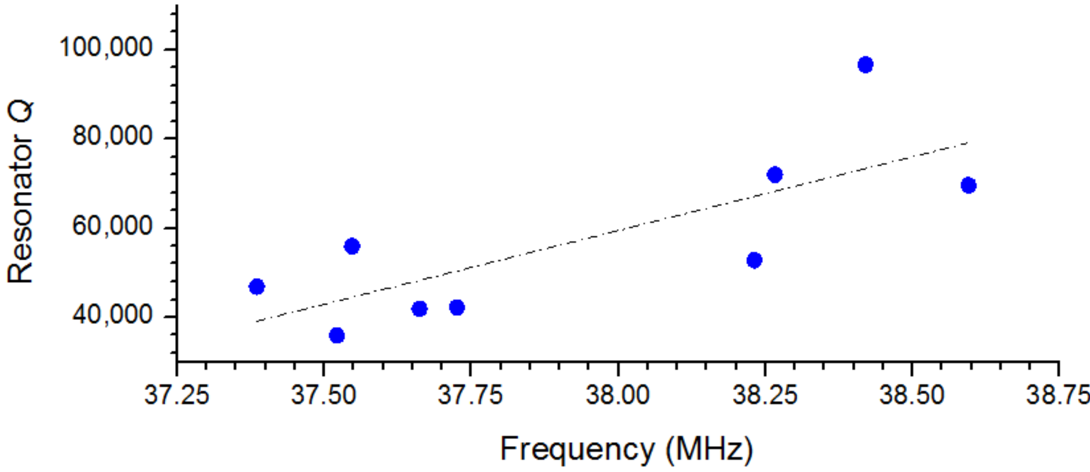

Figure 4-17: Measured resonator Q as a function of its operating frequency. The resonator center frequency has a strong correlation with its temperature compensation. Black line (dotted) represents the least squares linear fit to the measured data.

4.3 Piezoelectrically Actuated Temperature-Compensated Lamé Resonators

Lamé-mode resonators actuated piezoelectrically with Wurtzite materials such as AlN are susceptible to charge cancellation due to the nature of the Lamé-mode resonance. Each point within the resonator undergoes simultaneous expansion and contraction in the two in-plane orthogonal directions. As the d_{31} and d_{32} piezoelectric coefficients of AlN have the same magnitude and polarity [69], the net piezoelectric charge pick up is ideally close to zero and practically very small due to the asymmetry of the piezoelectric stack. As will be discussed, the oxide islands used for temperature compensation can also be used effectively to enable piezoelectric actuation of the Lamé-mode [39].

4.3.1 Resonator Design

Figure 4-18 shows a schematic view of the Lamé-mode with the position of the oxide islands and the top electrode geometry marked for clarity. The layout of the top electrode is critical for piezoelectric actuation and the shape is optimized based on the strain profile across the resonator. The design strategies implemented in the case of the electrostatically actuated Lamé-mode resonators are used to minimize anchor loss in the device. Similar oxide-refilled islands as described in Section 4.2 are used to achieve temperature compensation of the piezoelectrically actuated resonators. The simulated turnover temperature as a function of 'gap' *i.e.* the distance between the oxide islands is plotted in Figure 4-19. As has been discussed earlier, due to the frequency loading from the oxide islands, the support tethers are optimized to have a tether length of 10.5 μm and tether width of 2 μm.

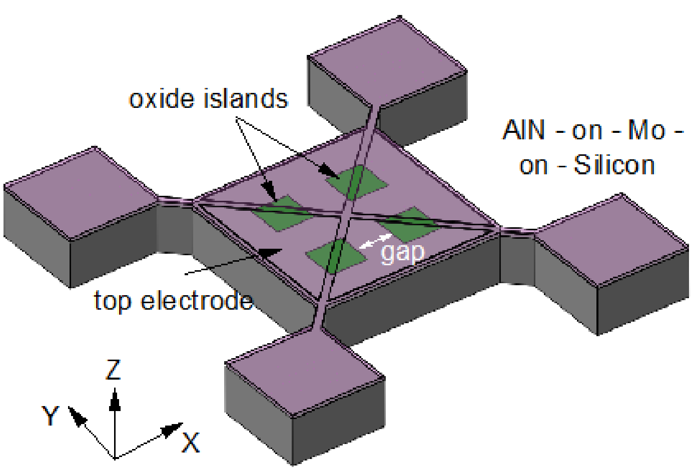

Figure 4-18: Schematic of a temperature-compensated Lamé-mode resonator. The location of the oxide-refilled trenches and the triangle shaped top electrode layout can be clearly seen.

As was pointed out earlier, the crystal symmetry of AlN makes it challenging to actuate the fundamental Lamé mode of resonance. However, the presence of the oxide islands within the resonator volume skews the strain profile in the resonator and consequently the temperature-compensation strategy has an added benefit of improving the total charge pickup and thus helps actuate the Lamé mode.

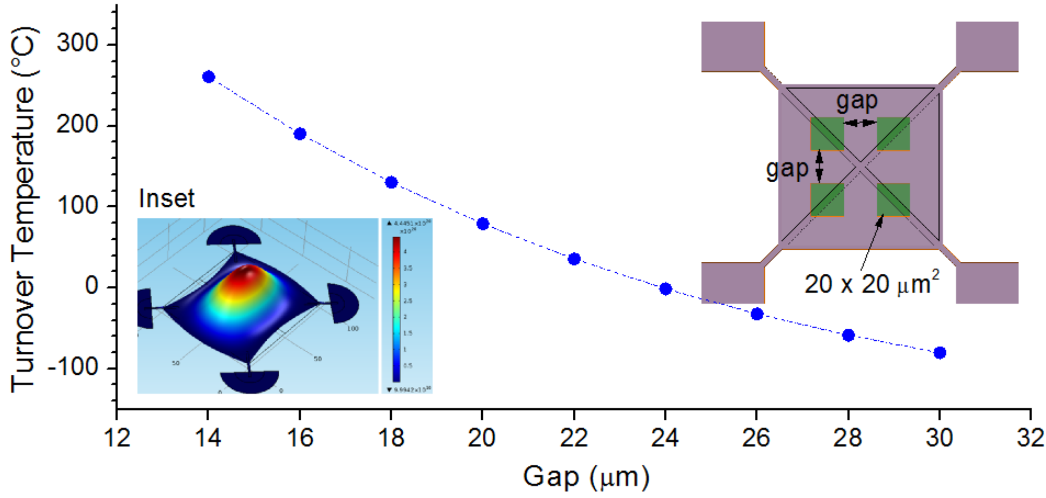

Figure 4-19: Simulated turnover temperature for the Lamé-mode resonator as a function of 'gap' between the oxide-refilled islands. The schematic on the right marks the location of the oxide within the resonator. The inset on the left plots the simulated strain energy across the resonator. The large sensitivity of temperature compensation to the 'gap' variable is due to the relatively sharp change in strain energy close to the resonator center.

Figure 4-20 plots the net strain for (a) an uncompensated and (b) a compensated Lamé-mode resonator across the AlN surface and clearly highlights the effect of including the oxide islands. To estimate the improvement in charge pickup of compensated resonators (compared to the uncompensated one), the strain gradient is integrated across the AlN layer and the results are summarized in Table 4-4. A 20× improvement in the total strain is seen due to the inclusion of oxide islands.

Based on the simulated net strain profile in Figure 4-20, four triangular shaped electrodes with the diametrically opposite electrodes connected together are used to achieve piezoelectric actuation. Figure 4-21 shows the simulated frequency response of a compensated and an uncompensated resonator, which highlights the improvement in insertion loss seen because of the oxide islands.

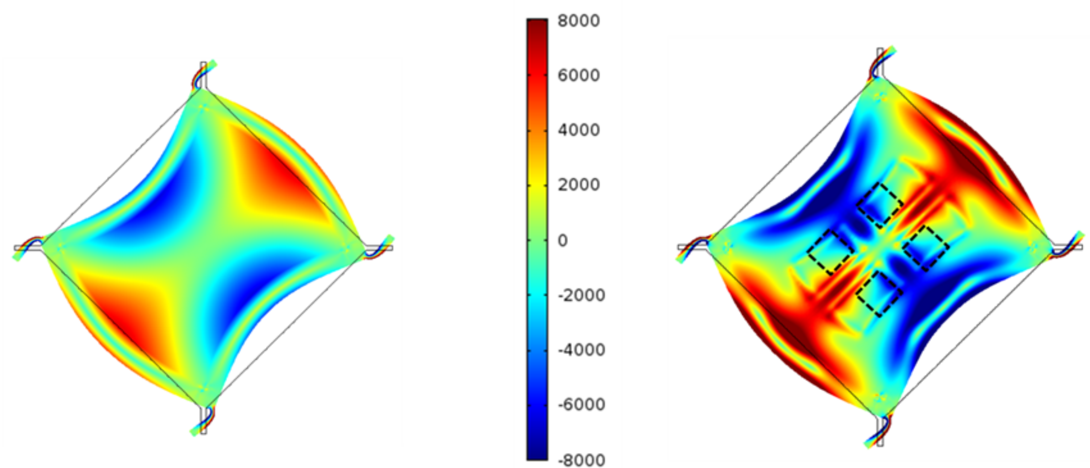

Figure 4-20: Net strain across the AlN surface for (a) uncompensated and (b) compensated Lamé-mode resonator. The presence of the oxide islands is seen to skew the strain profile. The color gradient plots the change in net strain across the surface, with red and blue representing positive and negative strains respectively.

Table 4-4: Estimated volume integral of strain in the AlN layer along the resonator in-plane axes showing the effect of silicon and oxide-refilled trenches on the effective charge pick-up.

Resonator	**Strain in X (ε_X) (m^3)**	**Strain in Y (ε_Y) (m^3)**	**ε_X -ε_Y (m^3)**
AlN	3.95×10^{-15}	3.96×10^{-15}	2.51×10^{-18}
AlN-on-Si	4.03×10^{-15}	4.10×10^{-15}	6.74×10^{-17}
AlN-on-Si with oxide	2.03×10^{-15}	0.662×10^{-15}	1.37×10^{-15}

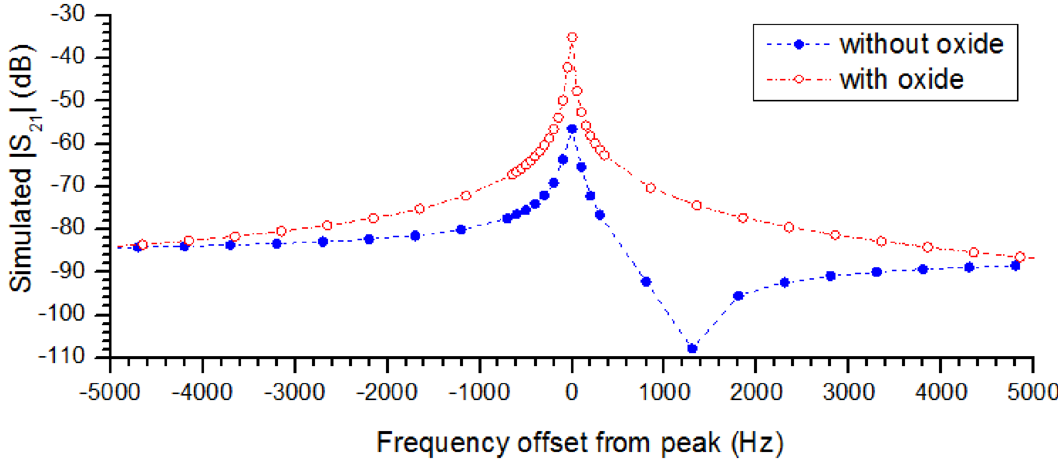

Figure 4-21: Simulated $|S_{21}|$ for a temperature-compensated (with oxide) and uncompensated (without oxide) Lamé-mode resonator. Simulated response assumes a resonator *Q* of 100,000.

4.3.2 Fabrication process of temperature-compensated piezoelectrically actuated Lamé resonators

Devices are fabricated on a SOI wafer with a 25 µm thick high-resistivity (>1000 Ω.cm) device layer (as opposed to low-resistivity device layer used for electrostatic resonators). Figure 4-22 shows the schematic of the fabrication process and is similar to the one described in Chapter 2 Section 2.1.3 and Section 2.2.4. In order to obtain completely refilled trenches, the trench DRIE is optimized to provide a straight sidewall with an opening of 1.2 µm. The spacing between the trenches is set to be 0.8 µm. From the cross-section images of the electrostatic batch, a fairly large sidewall taper was identified for the refilled trenches. In this run, the trench DRIE

was optimized to provide straighter sidewalls. Figure 4-23 shows cross-section SEM images of the DRIE trenches and the oxide-refilled islands and reveal the improvement in the trench-refill process. Figure 4-24 shows a SEM image of a fabricated Lamé-mode resonator.

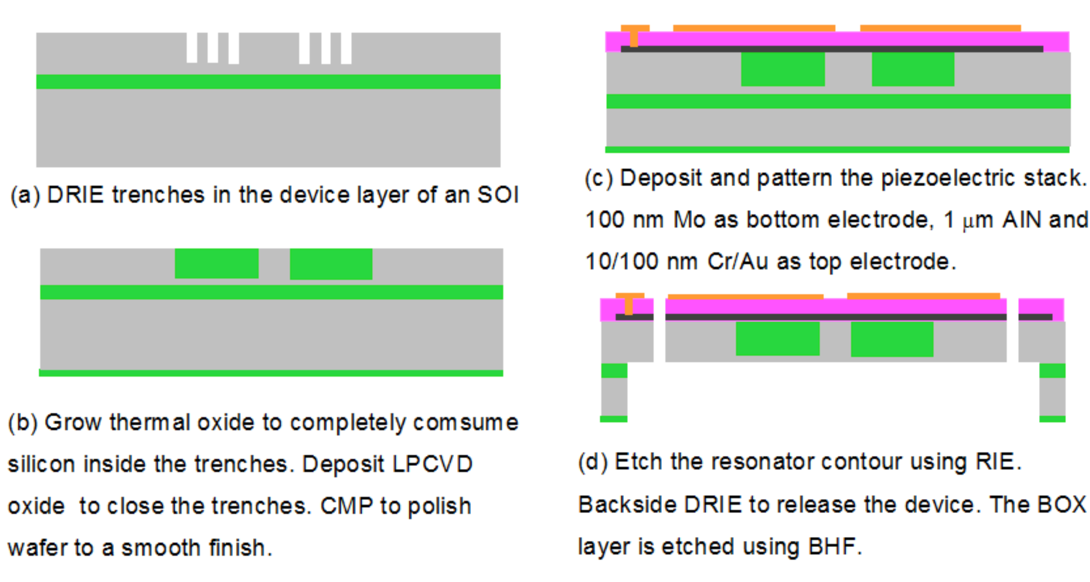

Figure 4-22: Process flow used for the fabrication of temperature-compensated piezoelectrically-actuated Lamé-mode resonators.

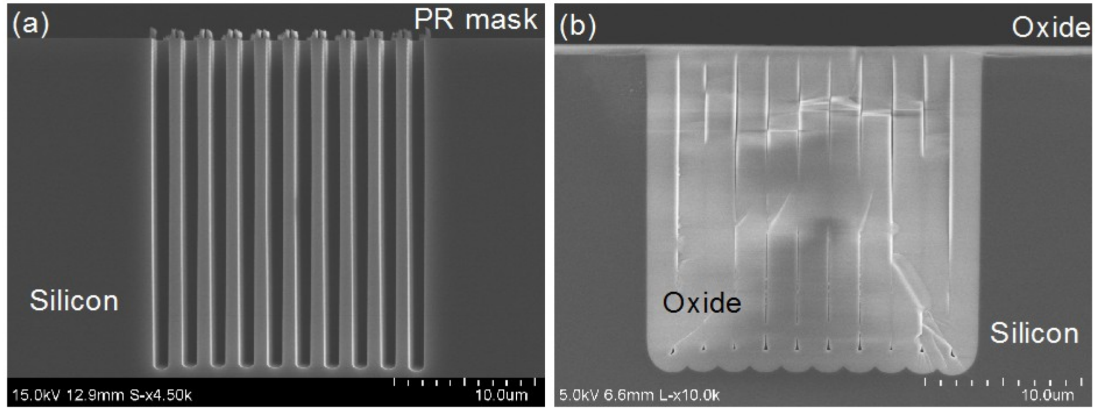

Figure 4-23: Cross-section SEM images of (a) the DRIE trenches to be oxidized, (b) a single oxide-refilled island.

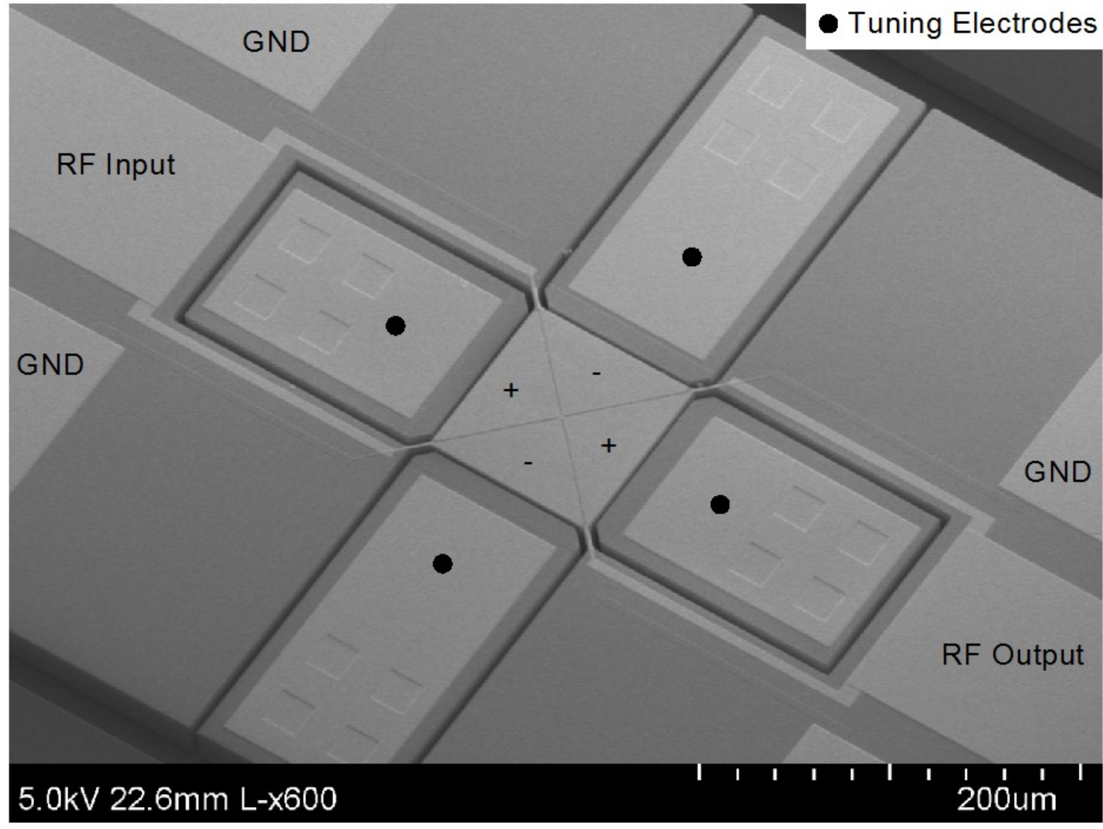

Figure 4-24: A SEM image of a fabricated Lamé-mode resonator. The top input and output ports are labeled with '+' and '-' respectively and resembles the net strain profile seen in Figure 4-20. The oxide-refilled trenches are embedded within the silicon body and are not visible through the top metal layer.

4.3.3 Measured Results

In order to characterize the performance of the resonators, on-wafer measurements are carried out in a temperature-controlled probe station at a pressure of ~100 μTorr. Figure 4-25 (a) and (b) plot the measured frequency response of a temperature-compensated and an uncompensated piezoelectrically-actuated Lamé-mode resonator, respectively. As predicted, both the insertion loss and the signal to noise ratio of the compensated resonator are improved as compared with the resonator without the compensating trenches. Figure 4-26 shows the measured frequency shift with temperature for three temperature-compensated Lamé-mode resonators. The

three resonators have the same volume of oxide but different 'gap' between the oxide islands. The measured results in Figure 4-26 compare well with the estimated turnover temperature presented in Figure 4-19. There is a nominal turnover temperature shift of approximately -80 °C for all designs, which can be attributed to the presence of the piezoelectric stack that was ignored in the simulations.

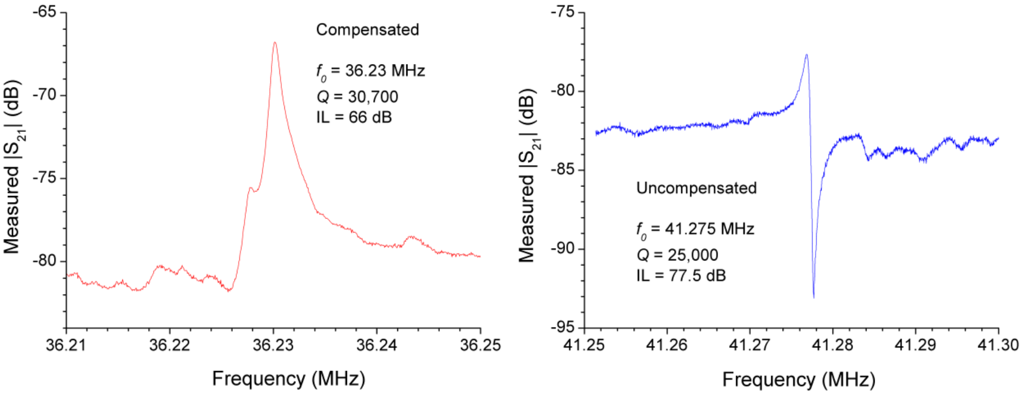

Figure 4-25: Measured frequency response of a (left) temperature-compensated and (right) uncompensated piezoelectrically-actuated Lamé-mode resonator, measured at room temperature and in vacuum.

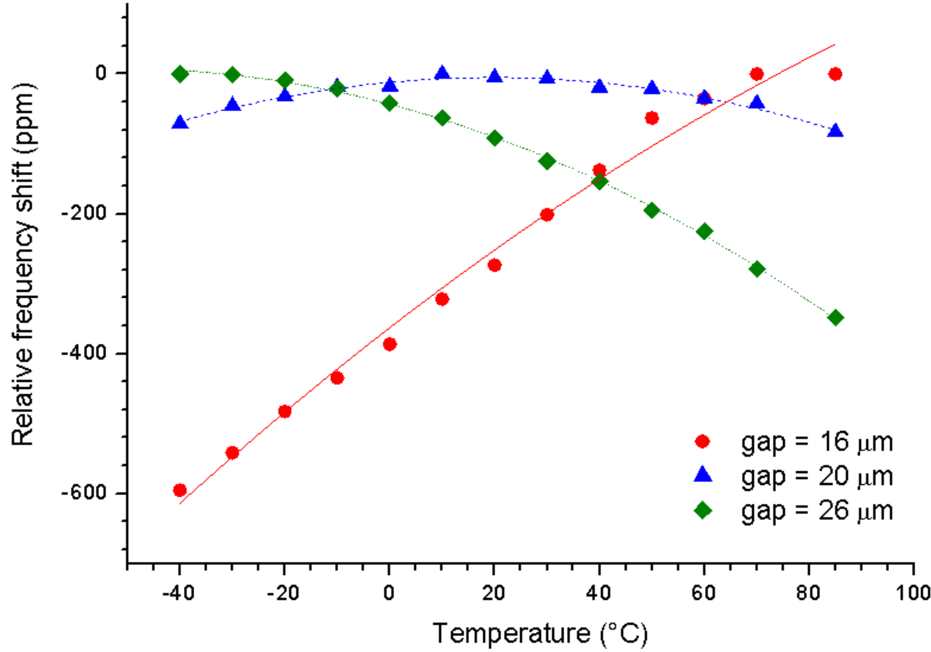

Figure 4-26: Measured peak frequency shift as a function of temperature for three different 'gap' between the oxide islands.

In order to study the effect of the piezoelectric interface on the resonator *Q*, multiple devices were measured in air. The measured resonator *Q* as a function of its frequency is plotted in Figure 4-27. Figure 4-28 summarizes the measured results of the Lamé-mode resonators as a function of 'gap' between the oxide islands. Both resonator *Q* and insertion loss reveal no clear trend and show a large spread in the measured data. This result along with the data in Figure 4-27 suggests that unlike their electrostatic counterparts, the *Q* of piezoelectrically-actuated resonators is not limited by the refilled oxide-islands. The random nature of the *Q* data strongly points to interface losses arising from the metal-piezoelectric stack to be the dominant loss mechanism in the resonators.

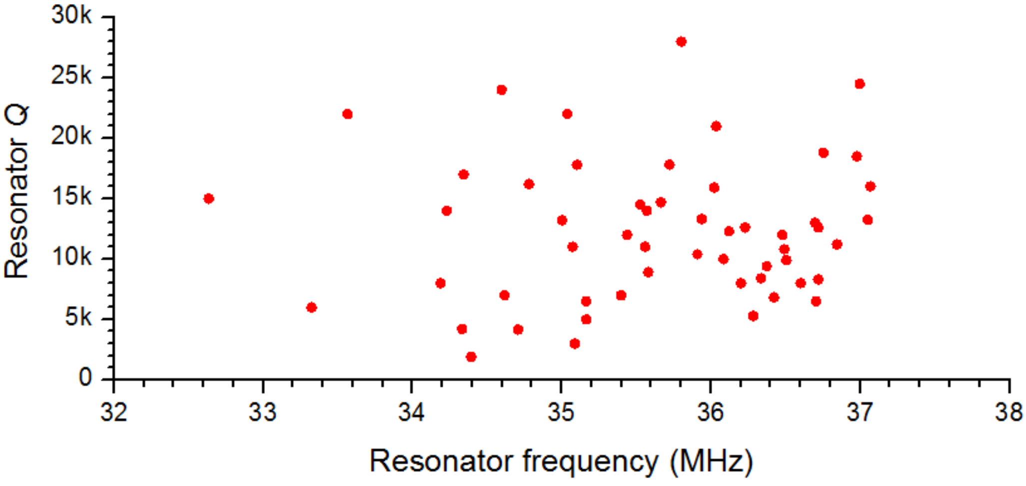

Figure 4-27: Measured resonator *Q* as a function of its center frequency.

On the other hand, the resonator insertion loss correlates very well with the measured resonator *Q* as can be seen from Figure 4-29. This is expected as the increase in resonator *Q* will increase the magnitude of the net strain leading to an improvement in the resonator insertion loss.

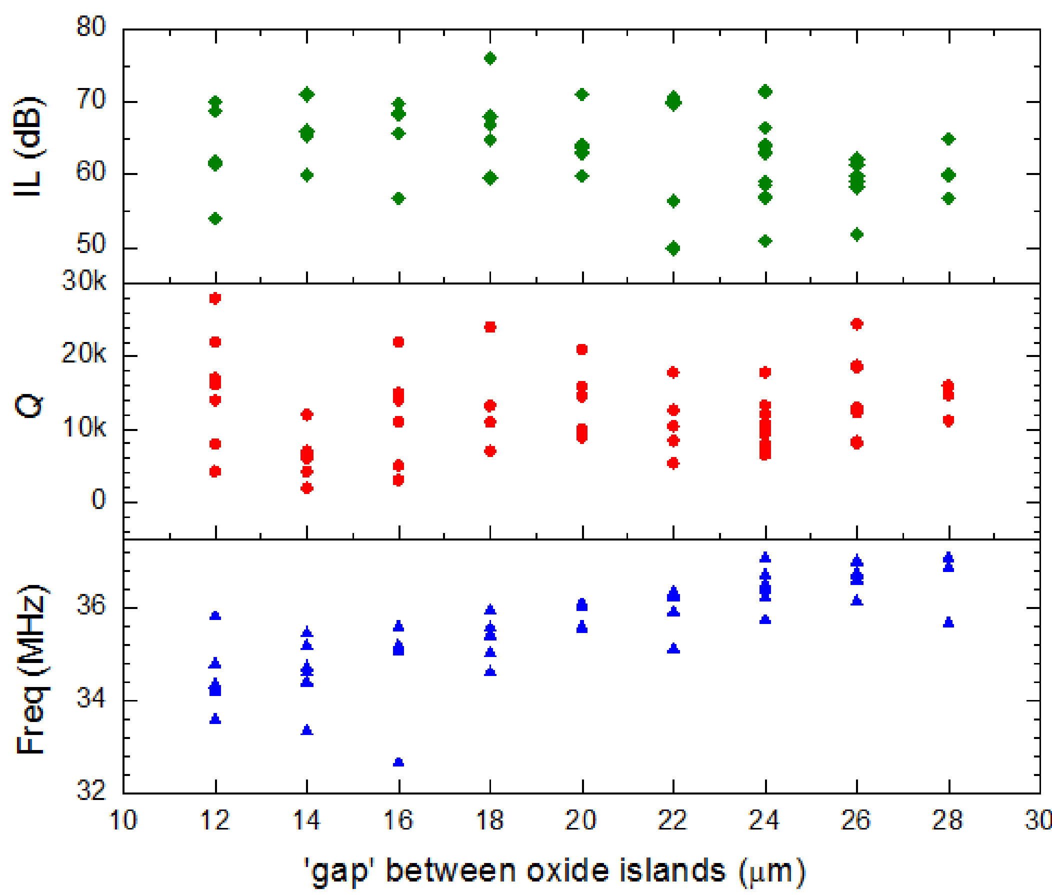

Figure 4-28: Measured resonator frequency, resonator Q and resonator insertion loss as a function of the temperature compensation of the resonator. As can be expected, for smaller 'gap' between the oxide islands, we have a higher resonator frequency. Note the lack of correlation between resonator Q and the 'gap' between the oxide islands.

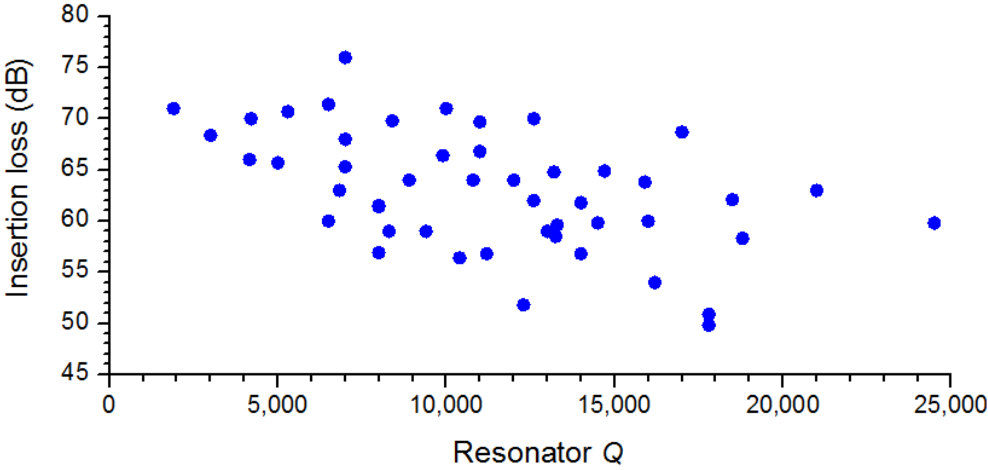

Figure 4-29: Measured resonator insertion loss as a function of its quality factor. In order to achieve the simulated insertion loss of 35 dB, resonators with much higher Q will be essential.

4.4 Conclusions

This chapter described results of the effect of silicon dioxide temperature compensation layer and the piezoelectric stack on the *Q* of micromechanical resonators using both capacitive and piezoelectric uncompensated as well as compensated Lamé-mode resonators as test vehicle. A silicon only Lamé-mode resonator operating at 41.5 MHz is shown with a *Q* of 302,120 and an $f \times Q$ of 1.25×10^{13}. With the inclusion of a 1 μm polysilicon capping layer, the *Q* of a similar resonator dropped to 125,220. The same electrostatically actuated structure but with temperature-compensated oxide islands shows *Q* values in the range of 40,000 to 96,000 around a center frequency of ~ 38 MHz. The decrease in the resonator *Q* as the temperature-compensation (effect of oxide) is increased (Figure 4-17) points to *Q* loading from the refilled silicon dioxide. The inclusion of the oxide-islands provides a lateral interface in the resonator and this along with the stress in the oxide might be contributing to the increased loss in the resonators.

Subsequently, the measured results of piezoelectrically actuated and temperature-compensated resonators were presented in Section 4.3.3. The best measured *Q* is seen to be 30,700 for these resonators with a significantly improved power handling capability [39]. From the measured results of multiple resonators shown in Figure 4-27 and Figure 4-28, we note no correlation between the resonator *Q* and its temperature-compensation. The metal-piezoelectric stack that is included atop the silicon resonator presents a vertical interface which seems to degrade the resonator *Q*, making the oxide induced losses secondary. A preliminary analysis taking the range of *Q* measurements suggests that the oxide islands limit the *Q* to between 60,000 to 400,000 with a large process induced spread. This leads to the

estimate of *Q* limit from the piezoelectric stack to be between 16,000 to 77,000 depending on the assumed *Q* limit of the trench-refill process. These results are summarized in Table 4-5. In the estimation of these *Q* limits, it is assumed that the 1 μm polysilicon layer loads the device *Q* from 300,000 to 125,000. With the different DC bias values used in the two measurements, it is difficult to have a high confidence in this conclusion. However, we can confidently state that the *Q* limit of the polysilicon interface is greater than 213,000.

Table 4-5: Analysis of the *Q* limit due to the inclusion of various interface elements in Lamé-mode resonators.

Interface	*Q* limit	
	Minimum	**Maximum**
None (Base resonator)	302,000	302,000
Oxide islands	60,000	400,000
Piezoelectric stack	16,000	77,000

Given the improved trench-refill process used in the fabrication of the piezoelectrically actuated resonators (Figure 4-23), it is very likely that the oxide induced *Q* limit is closer to the higher end while the piezoelectric stack induced *Q* limit is closer to the lower end of their respective *Q* spectrums in Table 4-5. This would also agree well with published resonator *Qs* in literature with piezoelectric actuation [57], [70].

These results have important consequences in the development of next generation of piezoelectric resonators. Realizing the role of piezoelectric stack in limiting the resonator *Q*, a detailed investigation of the metals to be used will be

useful. CMOS industry has investigated various metal silicides for use as interconnect layers to replace metals [71]. Since the processing of silicides is post-CMOS compatible, a potential alternative to metal electrodes could be to utilize such materials whose mechanical properties could be closer to the underlying silicon resonator. Doped amorphous silicon can be another alternative for the metal electrodes. From the relatively small Q loading from the 1 μm polysilicon cap seen in Figure 4-14, we can predict much improvement in Qs of piezoelectric resonators through the optimization of the piezoelectric stack materials.

In summary, this chapter includes the following research contributions:

- A thorough comparison between electrostatic and piezoelectric actuation of Lamé-mode resonators is presented.
- A new scheme is presented to both compensate for the TCF of silicon and achieve efficient piezoelectric actuation of silicon Lamé-mode resonators using oxide refilled islands selectively positioned in the resonator body.
- A systematic study of the various loss mechanisms arising from interfaces is made to analyze its effects on the resonator Q.

Chapter 5 ACOUSTICALLY COUPLED ALN-ON-SILICON FILTERS

5.1 Introduction and Motivation

In Chapter 3, we demonstrated a new multi-resonator clock that provides a stable frequency output without requiring temperature sensors and feedback control loop. Instead, the temperature sensitivity of the resonators is canceled using a mixing algorithm. After each mixer, we require a bandpass filter to only select the desired frequency component and remove the unwanted frequency products so as to not overwhelm the later signal processing stage. In this chapter, we describe the working principle and experimental characterization of acoustically coupled filters in which the resonating elements are elastically coupled in a single monolithic implementation. The use of the AlN-on-silicon platform ensures their easy integration with the temperature-compensated resonators presented previously in Chapter 2 and Chapter 4. The ability to integrate resonators and filters on the same die not only allows for a significant reduction in the clock footprint but also provides the ability to design for non-standard termination impedances.

Besides their use in the proposed clock system, small-size narrow-band passive filters have numerous other applications. Wireless communication devices require a significant amount of pre-processing of analog signals within the transmitter and receiver sections before any data can be digitally processed. An important function within the RF front-end of wireless transceivers is signal filtering to achieve reduction in the overall power consumption for enhanced battery life. The relatively

small bandwidth requirement along with stringent specifications on the skirt angle requires the use of coupled mechanical resonators, having higher *Q*s than electrical RLC resonators as the filtering element. Figure 5-1 shows the block diagram of the RF front-end of a modern cellular radio and highlights the numerous bandpass filters required at various stages in the transmitter/ receiver section [72].

Traditionally, surface acoustic wave (SAW) filters have been used to achieve the filtering function in cellular transceivers [38]. The working frequency of SAW devices is determined by the lateral pitch of their interdigitated electrodes, which is in turn limited by the lithography resolution. While higher working frequencies have been achieved, the frequency of commercial SAW filters is typically limited to about 2 GHz [73]. In contrast, bulk acoustic wave (BAW) devices are not restricted by the lateral resolution and can reliably work beyond 2 GHz, in their thickness-extension mode.

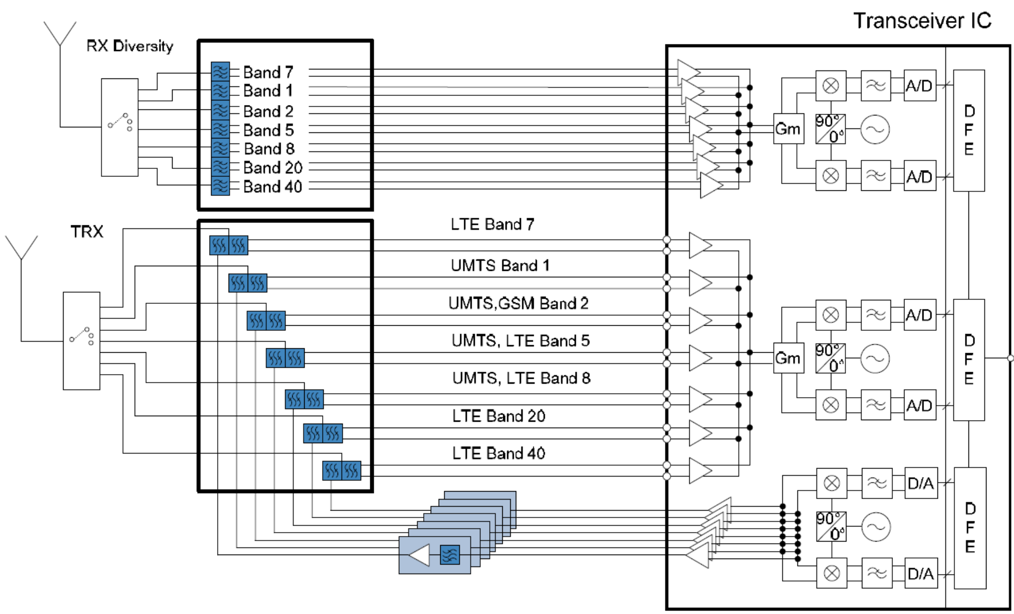

Figure 5-1: RF front-end of a modern cellular radio. Image reproduced from [68].

Typical thickness-mode acoustic filter architectures include electrically-coupled resonator filters [20] (such as ladder-type film bulk acoustic resonator (FBAR) filters) and acoustically coupled resonator filters [38], [40], [74], [75], [76]. FBARs have been successfully commercialized within the duplexer, which has some of the most demanding requirements on the out-of-band rejection and skirt angles. Compared to the relatively large (1 mm × 1 mm) ladder-type FBAR filters, which usually need several stages of resonators with tight control over each individual device [77], acoustically coupled filters eliminate the large feed-through capacitance from the input to the output and provide good out-of-band rejection within a compact microstructure. Micromachined laterally coupled thin-film piezoelectric-on-substrate (TPoS) filters such as AlN-on-silicon filters were thus proposed as a viable alternative to FBAR and SAW based filters in communication applications [78] and are chosen in this work to implement bandpass filters.

In the first section, a detailed description of the working principle of acoustically coupled filters is presented. Subsequently, a proof-of-concept thickness-mode filter is presented and characterized. Finite element analysis is utilized to model the filter characteristics using which, guidelines for achieving specific filter bandwidth and insertion loss are presented. Finally, these ideas are applied towards the design of in-plane acoustically coupled filters for use at the mixer output in the clock architecture described in Chapter 3.

5.2 Thickness-Extension Acoustically Coupled Filters

Figure 5-2 shows a schematic of a TPoS filter, in which two or more resonating sections of a low-loss material (*i.e.*, the substrate) are coupled to one another. A thin piezoelectric film laid on the substrate enables electromechanical transduction. The use of a substrate enables reaching lower frequencies, without having to deposit or grow thick piezoelectric layers, and significantly improves the filter power handling [79]. In addition, by adjusting the thickness of the substrate layer (*e.g.*, through oxidation or etching), multiple frequency filters can be implemented on a common substrate while using the same piezoelectric film thickness for all the devices [80], representing a pathway towards filter arrays on-a-chip. By co-integrating the in-plane extensional-modes, discussed later in Section 5.3, filters targeting a very broad frequency range from a few MHz all the way into the GHz range can be enabled along with high-Q resonators within a single AlN-on-silicon platform.

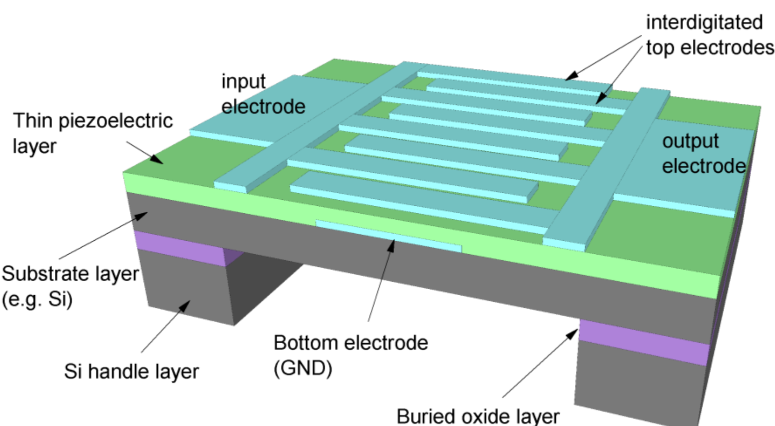

Figure 5-2: Schematic view of an acoustically coupled thickness-mode TPoS filter. The resonating sections are the areas defined by the input and output electrode fingers. The substrate layer is part of the resonating stack and is a 5 μm thick high resistivity (> 1 kΩ·cm) silicon device layer of an SOI wafer. 1 μm thick aluminum nitride is used as the piezoelectric layer and 100 nm molybdenum (Mo) is used as the top and bottom electrode material.

5.2.1 Working Principle

A thickness-mode TPoS filter consists of two interdigitated top electrodes (input and output), a solid bottom ground electrode, and a thin layer of a piezoelectric material deposited on a substrate (Figure 5-2). The two electroded regions are coupled via evanescent acoustic waves in the unelectroded region giving rise to a filter response. Such a design takes advantage of the high electromechanical coupling of the piezoelectric layer and the low mechanical damping in the substrate material to achieve low insertion loss [81]. For a given filter stack, multiple thickness-extensional modes can be excited and the choice of mode order can be made based on the electromechanical coupling factor, which is given by [82]

$$k^2 = \frac{\pi}{2} \cdot \frac{f_s}{f_p} \cdot \tan\left[\frac{\pi}{2} \cdot \frac{(f_p - f_s)}{f_p}\right], \qquad \text{Equation 5-1}$$

where f_s and f_p are the series and parallel thickness-extensional resonance frequencies, respectively. These frequencies can be approximately calculated using the Mason's model [83]. The calculated coupling factors of the first six modes of the electroded stack presented in Figure 5-2 are listed in Table 5-1. It is seen that the fourth- and the fifth-order modes have the largest k^2 and are therefore favorable for filter applications. Here, we choose to focus on the fourth-order mode with a frequency of ~ 2.9 GHz.

Table 5-1: Electromechanical coupling factor of the thickness-extensional modes for the electroded stack presented in Figure 5-2.

Mode	**1st**	**2nd**	**3rd**	**4th**	**5th**	**6th**
k^2	0.12%	0.3%	0.57%	1.28%	1.64%	0.65%
f_s *(MHz)*	615	1331	2077	2772	3347	3987

In order to understand the working principle of acoustically coupled filters, it is important to look at the dispersive characteristics of Lamb waves. For a given stack, the Lamb wave dispersion curves can be computed using the Thomson-Haskell matrix technique [84] (refer Appendix A-1 **DISPERSION CURVES**). Figure 5-3 shows a part of the dispersion curves around the fourth-order thickness-extensional mode for the TPoS filter shown in Figure 5-2.

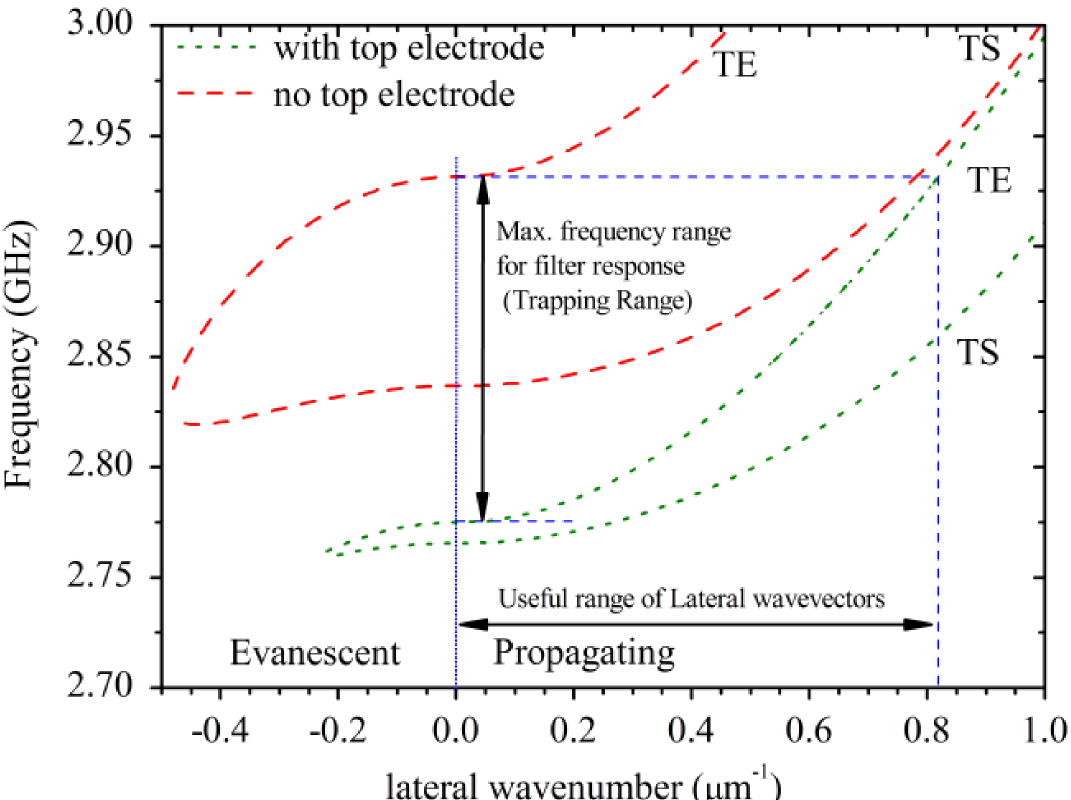

Figure 5-3: Dispersion curves of the fourth-order thickness-extensional (TE) mode and the nearest thickness-shear (TS) mode for the stack shown in Figure 5-2. The curves are computed using the Thomson-Haskell matrix technique with the thickness, Young's modulus, Poisson's ratio, and mass density of the different stack layers as inputs.

The frequency estimated using Mason's model corresponds to the cut-off point in the dispersion curves where the TE lateral wavenumber is zero. All lateral waves emanating from input electrode fingers and supported by the unelectroded

region (via evanescent waves) can be coupled to the output electrode [75]. The overall frequency response of the filter can be obtained by charge summation over the electrodes due to the superposition of all supported lateral waves [75], [76]. Thus, the filter frequency response depends on the dispersion relations, and the insertion loss depends on both the electromechanical coupling in each electroded region and the lateral coupling between the two regions.

As seen from Figure 5-3, for the presented TPoS stack, the frequencies supporting lateral coupling are between 2.77 and 2.93 GHz, corresponding to lateral wavenumbers between 0 and 0.82 μm^{-1}, or lateral wavelengths larger than 7.66 μm in the electroded region. Top electrode geometries allowing constructive interference over this range of wavelengths would provide the maximum bandwidth.

In the passband of the TPoS filter, the two electroded regions vibrate in the thickness-extensional mode, either in-phase or 180° out-of-phase (Figure 5-4). The two modes are acoustically coupled, resulting in a filter response. The corresponding in-phase and out-of-phase modes for an exemplary TPoS filter are simulated using COMSOL®, and are shown in Figure 5-5. The frequency separation between the two modes and hence, the bandwidth of the filter is set by the top electrode geometry. This behavior can be effectively captured using an equivalent circuit model where the two resonators are coupled using an inductive tank to mimic the physical operation of the device [85].

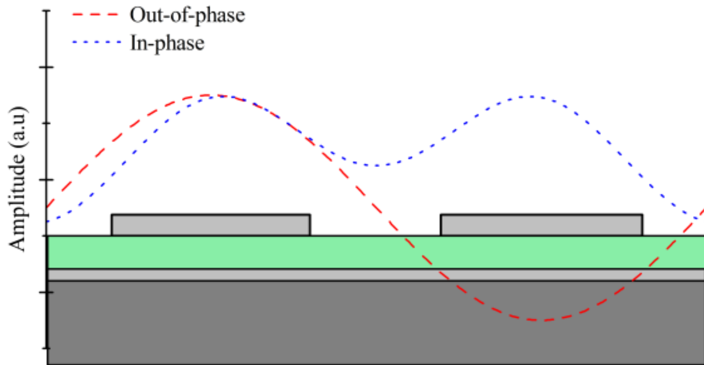

Figure 5-4: Lateral waves coupling input and output electrodes with wavelengths corresponding to in-phase and out-of phase modes, superimposed over a two electrode section for clarity.

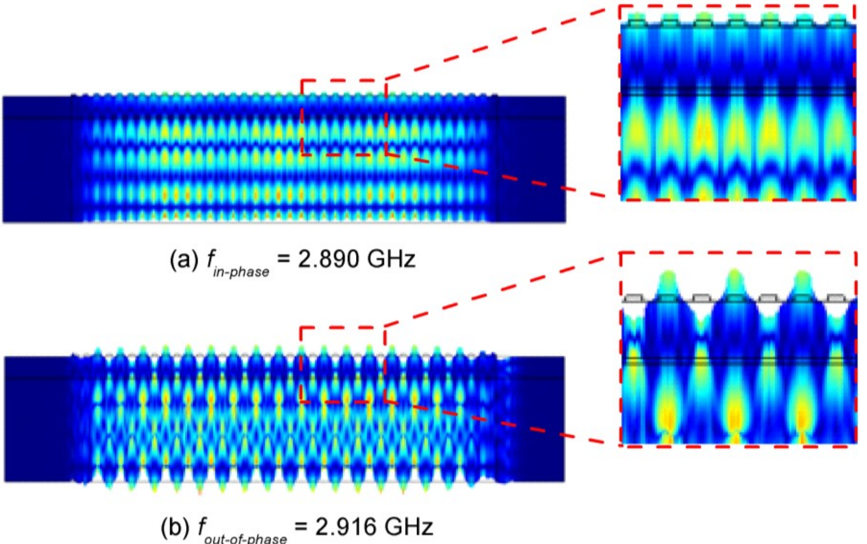

Figure 5-5: In-phase (a) and 180° out-of-phase (b) modes of a thickness-mode TPoS filter simulated using COMSOL®. The color spectrum plots the displacement. The two electroded regions are acoustically coupled and the coupling between them defines the filter bandwidth. The top electrode consists of 38 fingers with electrode width and spacing of 5 µm each.

5.2.2 Equivalent Electrical Model of Acoustically Coupled Filters

Figure 5-6 shows the equivalent electrical circuit conventionally used to model acoustically coupled filters and can be used to extract the equivalent parameters of TPoS filters [85], [86]. To mimic the acoustic coupling, the device is modeled by connecting two resonators with a coupling link. The energy oscillations

in the two resonators (R_m, L_m, C_m) can be either in-phase or out-of-phase, representing the simplified working principle of acoustically coupled filters. The Q and the frequency of the two resonators are modeled to be identical, and the value of the coupling link determines the frequency separation between in-phase and out-of phase modes *i.e.*, the bandwidth of the filter. The capacitive path between the input and output electrodes through the piezoelectric transduction layer sets the signal floor level in these filters and is modeled in the equivalent circuit via feedthrough elements (R_f and C_f). C_p and R_p are used to account for the static capacitance and the resistive leakage between the top electrodes and the ground metal layer, respectively.

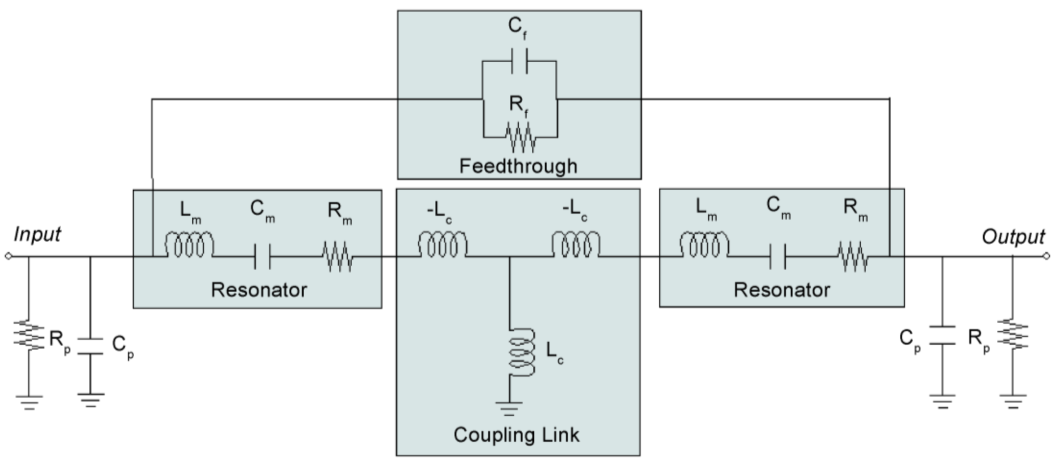

Figure 5-6: Equivalent electrical circuit used to model acoustically coupled TPoS filters.

5.2.3 Fabrication Process

Figure 5-7 shows the fabrication process flow for the thickness-mode TPoS filters. The top input/output electrodes are in interdigitated configuration. Due to their large acoustic impedance, metals such as Mo and platinum (Pt) are usually more favorable for the TPoS structure. The large acoustic impedance of these metals results

in high mechanical stress in the piezoelectric layer and therefore, a higher effective electromechanical coupling [87]. Pt and Mo are both well suited for the reactive sputtering of AlN and help achieve a good c–axis orientation for AlN. Here, we choose Mo over Pt as it is well characterized as a seed layer for AlN deposition. Figure 5-8 shows the top view of a fabricated AlN-on-Si TPoS filter.

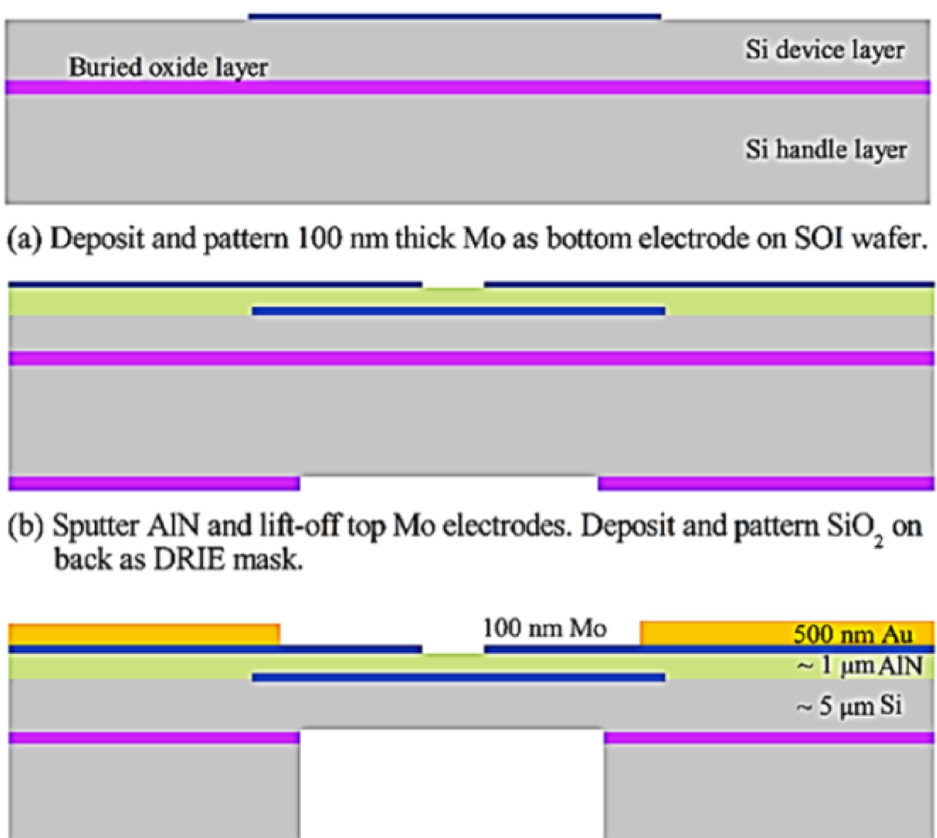

Figure 5-7: Fabrication process flow of a TPoS Filter [38]. The starting substrate is a high resistivity SOI wafer with Si device layer thickness of 5 µm ± 0.5 µm. In order to obtain better device uniformity, commercially available SOI wafers with a tight thickness tolerance (< 0.1 µm) or deposited polysilicon can be used.

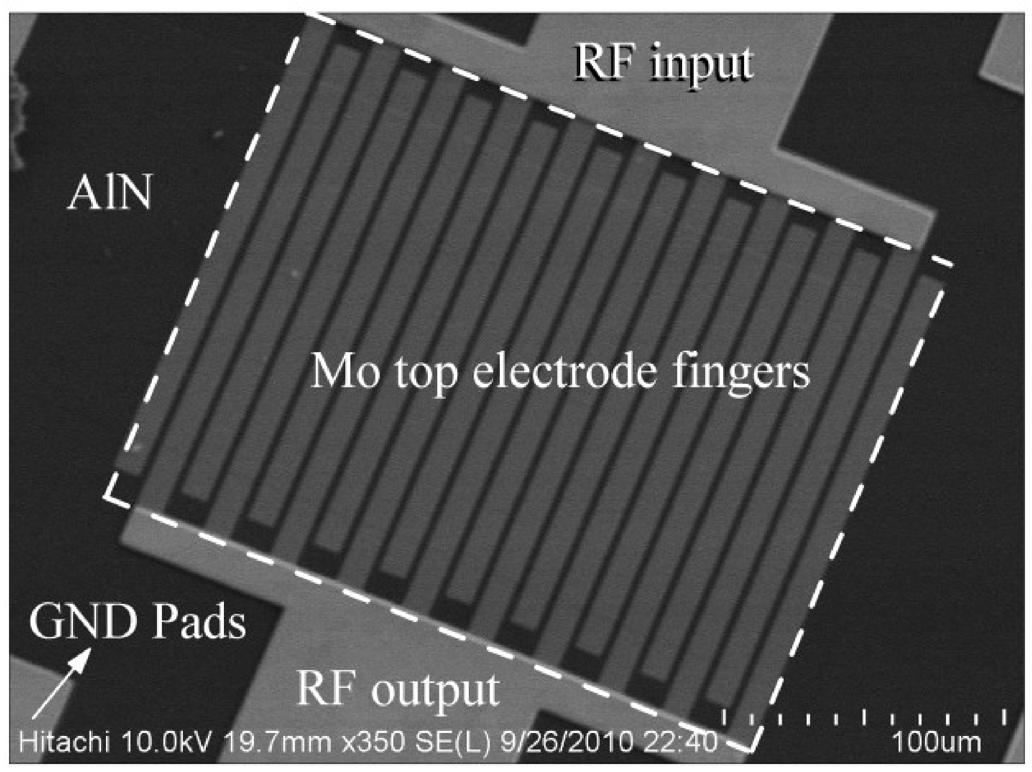

Figure 5-8: A SEM image of an acoustically coupled TPoS Filter. This device has 10 pairs of top electrode fingers with finger length of 150 µm, finger width of 10 µm and finger spacing of 5 µm.

5.2.4 Measurement Results

On-wafer measurement of filters is carried out at atmospheric pressure using an Agilent N5241A network analyzer with 50 Ω termination. The RF input power for all these measurements is -5 dBm unless otherwise stated. Figure 5-9 (a) shows the measured S-parameters of the filter shown in Figure 5-8. The filter stack consists of 5 µm of silicon, 1µm of AlN, and 100 nm of top and bottom Mo (refer Figure 5-2). The top electrode consists of 10 pairs of electrode fingers, each 10 µm wide and separated by an inter-electrode spacing of 5 µm. This filter has an insertion loss of 2.4 dB at 2.877 GHz and a 3 dB bandwidth of 12 MHz. Figure 5-9 (b) shows the measured phase of S_{21} for the same filter.

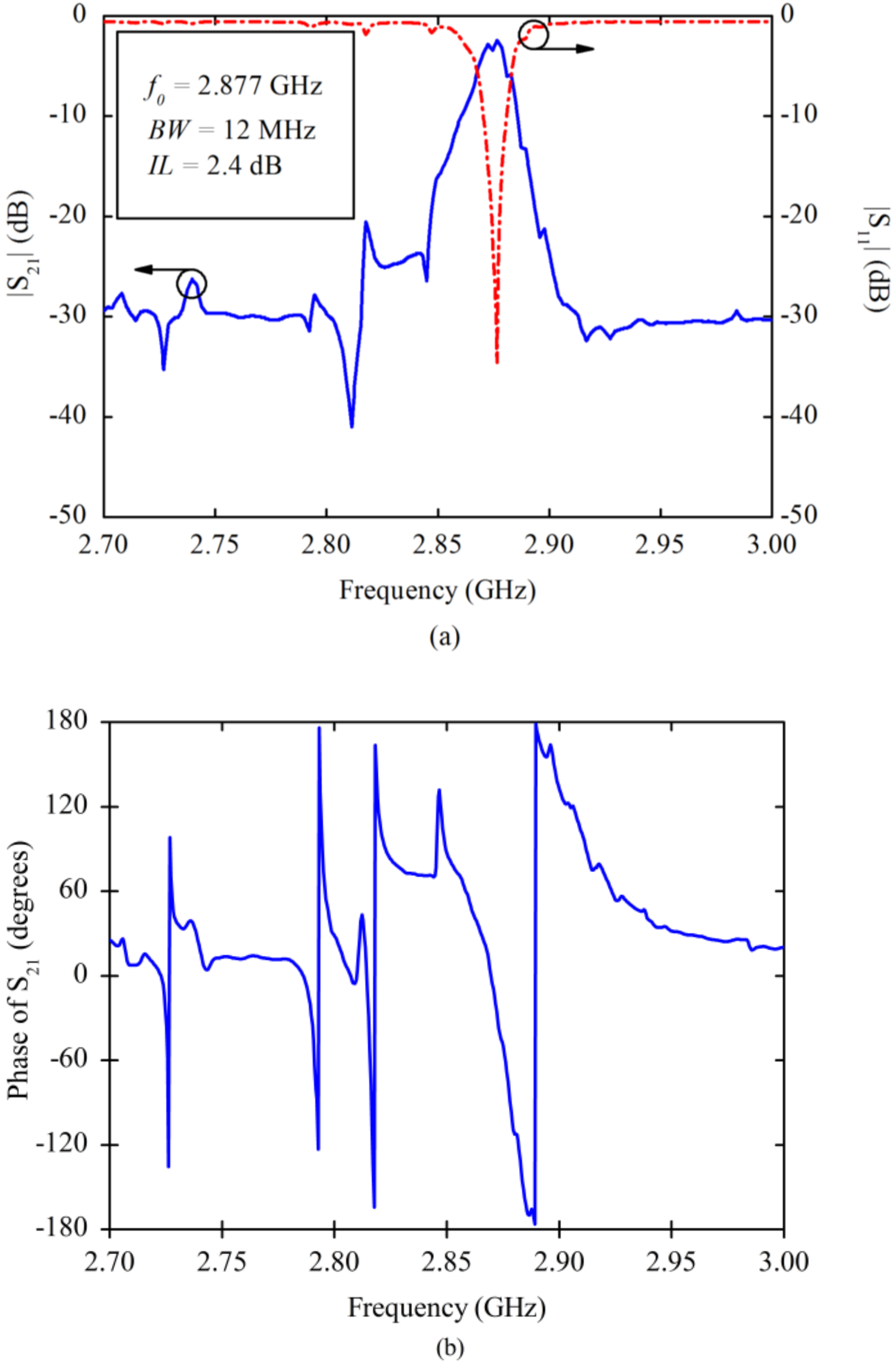

Figure 5-9: Measured (a) magnitude and (b) phase of S_{21} for the AlN-on-Si filter shown in Figure 5-8. The top electrode consists of 10 pairs of electrode fingers each 10 µm wide with 5 µm of inter-electrode spacing.

Figure 5-10 shows the measured filter response superimposed over the dispersion curves for comparison. From this figure one can see that the composite stack can support traveling waves in the electroded region, which are evanescently coupled in the unelectroded region in a frequency range (shaded region) much larger than the bandwidth of this filter. Therefore, larger bandwidth should be achievable through the appropriate design of the top electrode geometry (*e.g.*, electrode spacing and electrode finger width).

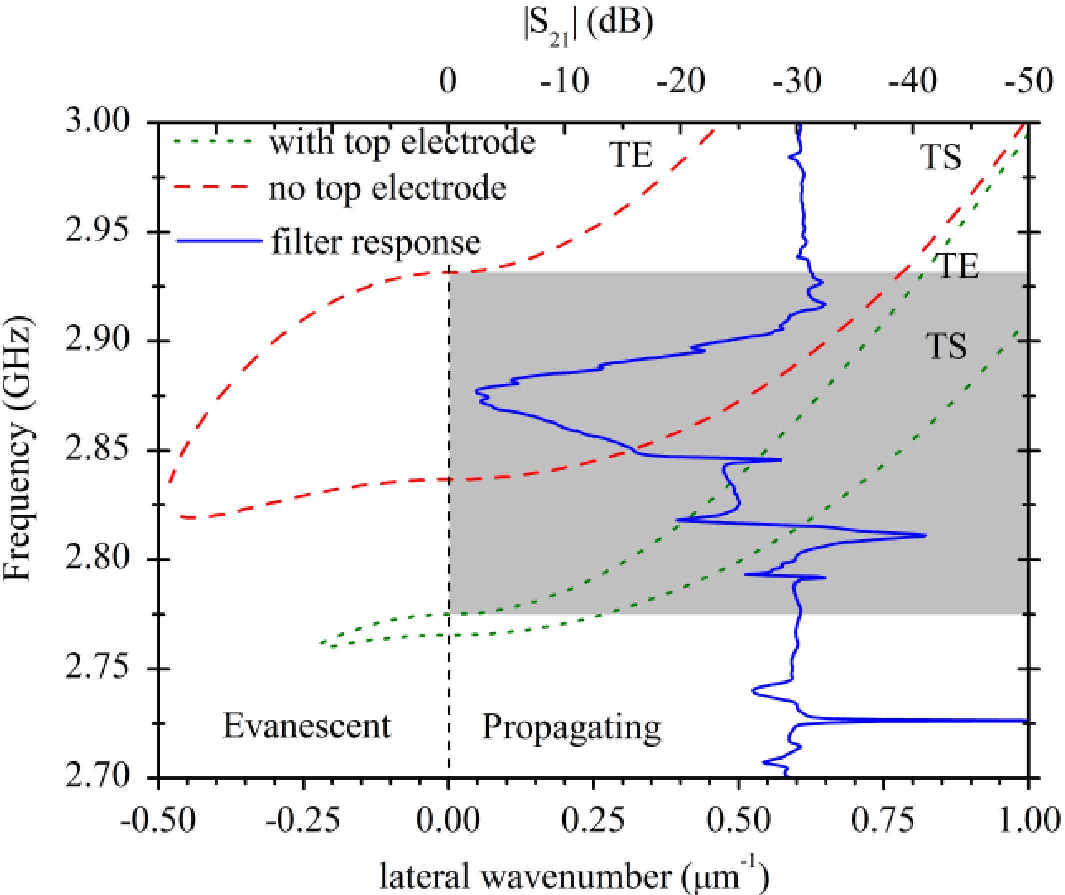

Figure 5-10: The dispersion plot for the TPoS filter stack shown in Figure 5-2. The measured filter response is superimposed for ease of comparison. From the plot, one can see that lateral waves with wavenumbers between 0.59 and 0.706 μm^{-1} in the electroded region contribute to the measured response.

5.2.4.1 Equivalent Electrical Model fit

The AlN-on-Si filter response is modeled using the equivalent circuit shown in Figure 5-6 and the measured and fitted frequency response of the filter near resonance is shown in Figure 5-11.

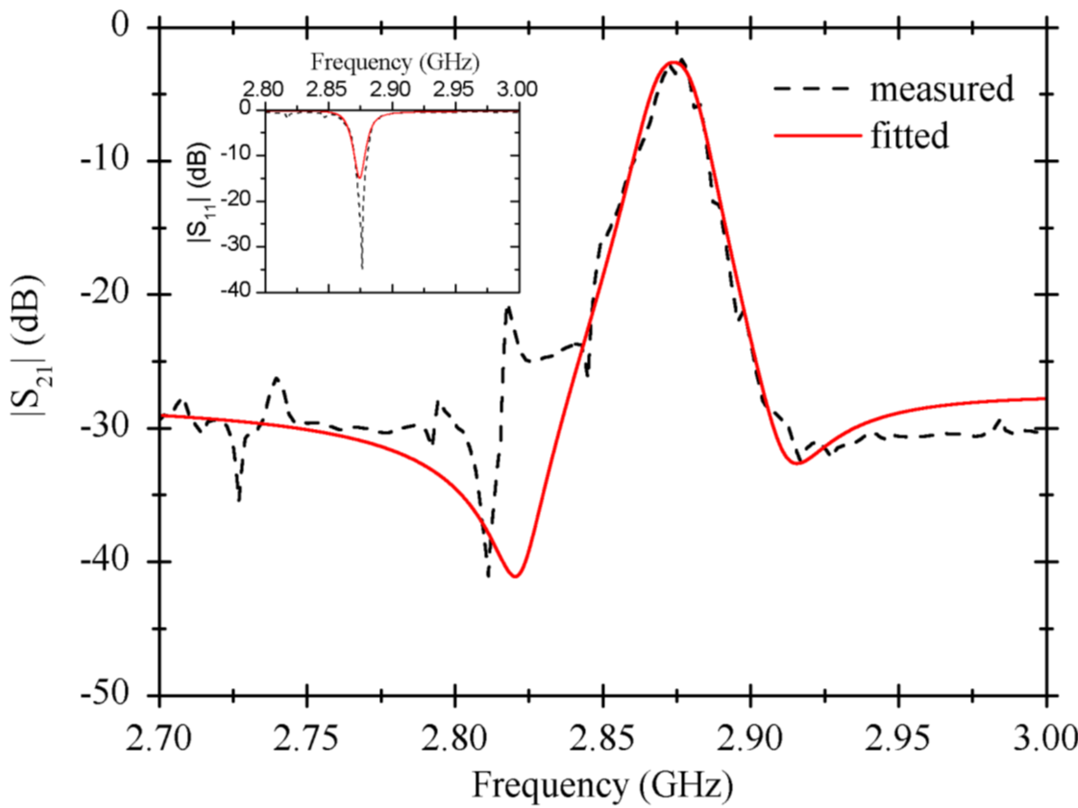

Figure 5-11: Measured and fitted responses for the AlN-on-Si TPoS filter seen in Figure 5-8.

The fitted values for the electrical components are listed in Table 5-2. C_p is the static capacitance at each port to ground and is estimated using the layout of the electrodes and the thickness of the piezoelectric layer. C_m is calculated using the C_p value and the electromechanical coupling for the fourth-order thickness-extensional mode. L_m is then determined from the center frequency. Values of the feedthrough capacitance and the resistive elements are chosen to best fit the measured response.

From the values in Table 5-2, it is seen that the quality factor Q_m of the series resonance is 949, which is lower than that of commercial AlN-based FBARs [20]. This provides a definite window of opportunity to improve the device performance.

Table 5-2: Equivalent circuit element values for the filter response shown in Figure 5-11.

Parameter	AlN-on-Si filter	Parameter	AlN-on-Si filter
R_m (Ω)	4.5	L_m (nH)	237.2
R_f (Ω)	3000	L_c (nH)	1.3
C_m(fF)	13	C_p (pF)	1.2
C_f (fF)	50	R_p (Ω)	2075

5.2.4.2 Power Handling

The frequency response of the TPoS filters at different power levels is also tested. Figure 5-12 shows the frequency response of the AlN-on-Si filter shown in Figure 5-8 at input RF power levels of -10 dBm and +20 dBm. There is no visible change in the frequency response between the two power levels. To verify the power handling of the device, third-order intercept point (IIP_3) measurements are carried out using a N5241A Agilent PNA-X network analyzer in the two-tone source power mode. The measured IIP_3 of the device is better than +30 dBm, which is the measurement tool limit. Such power handling capability is attributed to the very good linearity of the Si substrate layer, as explained in detail in [79].

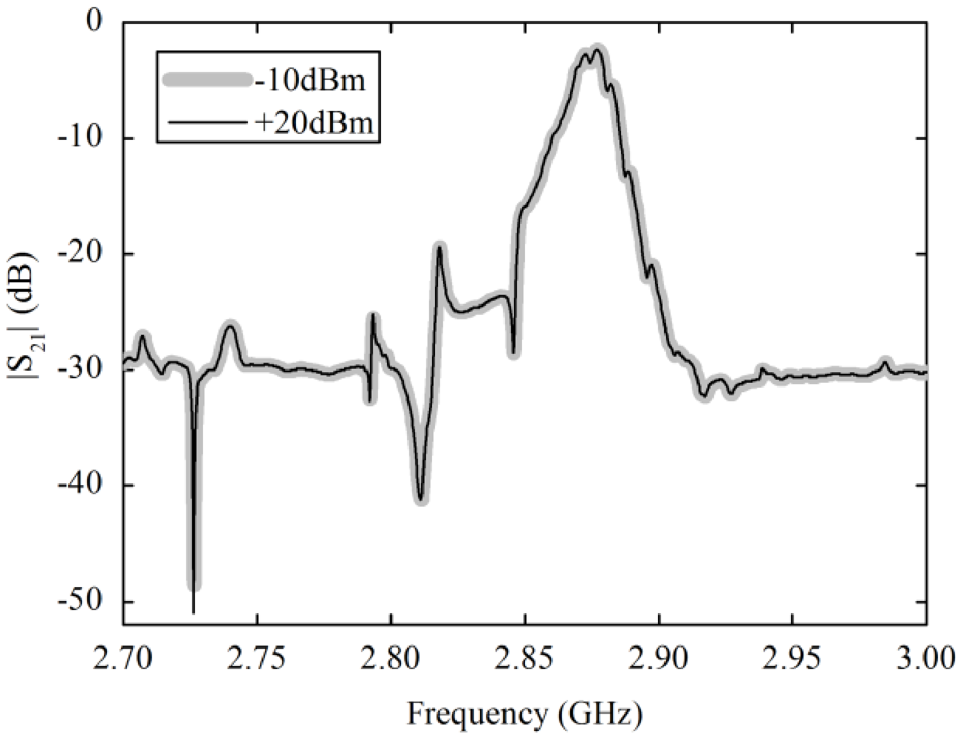

Figure 5-12: The frequency response of the AlN-on-Si filter shown in Figure 5-8 at different RF power levels.

5.2.4.3 Temperature dependence

The temperature dependency of the filter is characterized by measuring the filter response using a Lakeshore cryogenic probe station. The measurement is carried out in a vacuum chamber from -40 °C to +85 °C with calibration performed at each temperature point. The peak frequency versus temperature plot is shown in Figure 5-13 (a). The TCF calculated from the linear fitting of the peak frequency and temperature is about –28.6 ppm/°C, dominated by the TCF of silicon. Figure 5-13 (b) shows the effect of temperature on the insertion loss of the filter. From -40 °C to +85 °C, the insertion loss increases from 2.17 dB to 2.48 dB.

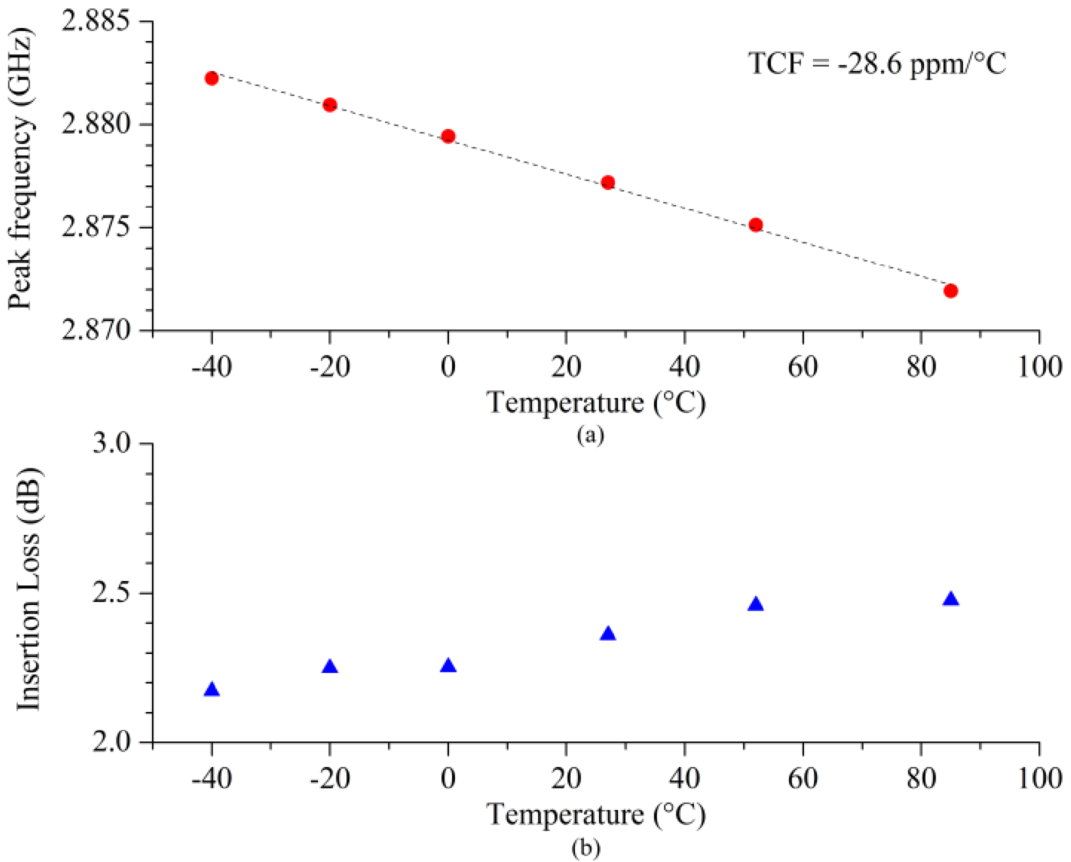

Figure 5-13: (a) The peak frequency and (b) the insertion loss *vs.* temperature plots of the TPoS filter shown in Figure 5-8.

The frequency shift induced by temperature change is comparable to the bandwidth of the filter. A temperature-stable design, achieved through passive compensation or by active tuning, may be desired in many applications. Such compensation can be realized by the introduction of a compensating layer of silicon dioxide in the structure, similar to the approach presented in Chapter 2.

5.2.5 Finite Element Modeling of Acoustically Coupled filters

In an acoustically coupled filter, multiple resonating elements are acoustically coupled through an elastic medium via evanescent waves. The passband

characteristics of these filters depends on the dispersive propagation properties of Lamb waves and is thus much more challenging to accurately predict. Prior experimental work on acoustically coupled filters has shown that the acoustic coupling between the resonators can be tuned by changing the interdigitated top electrode geometry [75], [76], [78], [88]. Careful optimization of the number of interdigitated fingers, electrode width, and pitch is necessary to obtain good passband characteristics with low insertion loss. It thus becomes necessary to perform a detailed analysis of the effect of filter geometry on the filter performance via the application of numerical simulation tools.

5.2.5.1 Simulation Platform

The device shown in Figure 5-2 was simulated with COMSOL® using the model presented in Figure 5-14 and is analyzed using the piezoelectric application mode of the MEMS structural mechanics module. In this module a multiphysics analysis is performed to solve the coupled wave equation which is obtained by considering the piezoelectric constitutive relations (refer to Chapter 1). A harmonic voltage V_{in} (ω) is applied to the input port while the output port is grounded as a necessary condition for the computation of the admittance parameters. To account for the energy radiating into the substrate, a PML boundary is implemented at the device edges [32]. As a rule of thumb, at least 10 mesh elements per unit wavelength are included in all simulations. From the finite element solution, we obtain the nodal current which is integrated over the output electrodes to give the total displacement current. This displacement current can be converted into the admittance parameters, which are finally converted to S-parameters (using 50 Ω termination impedance) for

direct comparison with the measured filter response [89]. Since a linear and passive device is simulated, $S_{21}=S_{12}$. We also take $S_{11}=S_{22}$ as the device is symmetric. In order to facilitate iterative simulations and maintain consistent mesh quality, the COMSOL®-MATLAB® interface is utilized. This setup is labeled as the simulation platform or model for further reference.

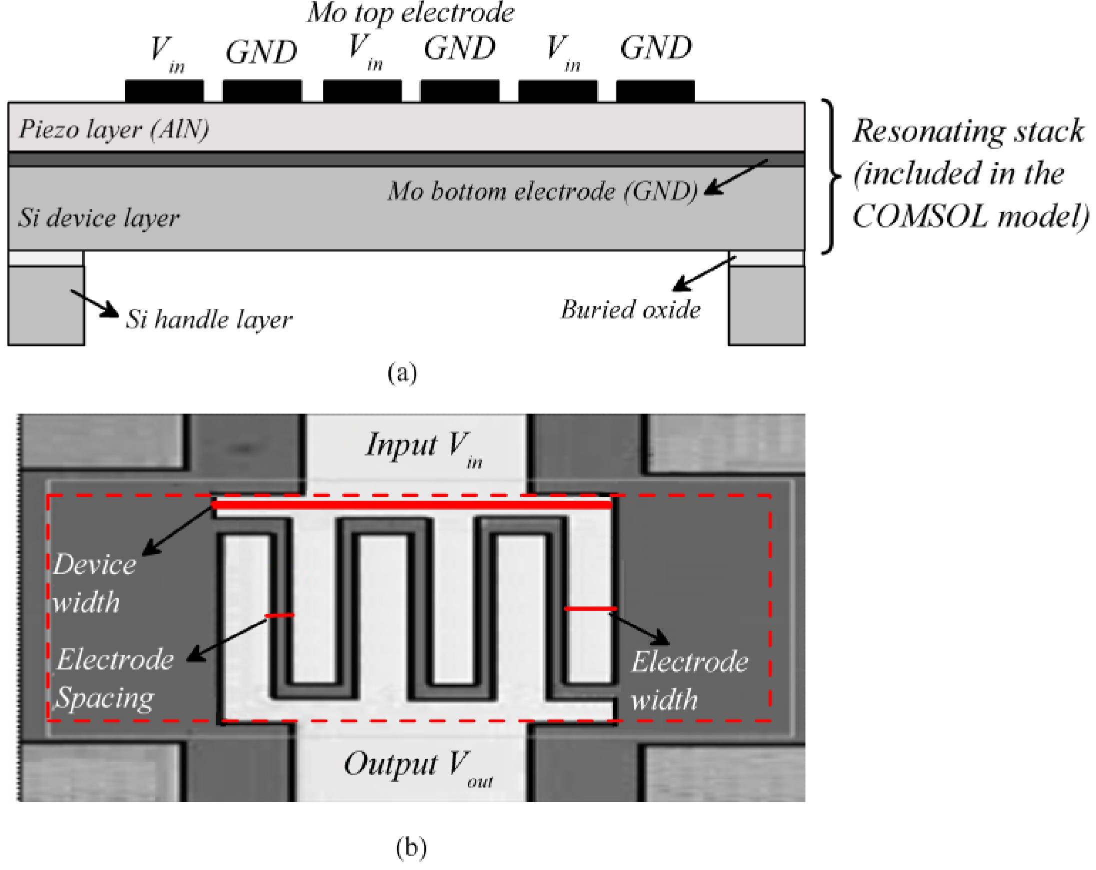

Figure 5-14: (a) A cross-section schematic view of a TPoS filter showing the electrical boundary conditions used in 2D simulations and (b) a top view showing the electrode geometric variables (only the boxed area is modeled).

5.2.5.2 Identification of the Geometric Parameters

A typical acoustically coupled filter as presented in this work has a minimum of six independent geometric design variables. These are the thickness of AlN and Si

layers, thickness of the electrode layers, electrode width, number of electrode fingers and electrode spacing. Varying the materials and material properties will add more variables, making the analysis significantly more complicated. In this analysis we focus on the geometric variables associated with the top electrode layout. Since there is no property variation in the third dimension, *i.e.* the dispersion curves along this direction remain unchanged; a two dimensional (2D) analysis using plain strain approximation is undertaken for reduced simulation time.

5.2.5.3 Model Verification

The simulated results of the thickness-mode TPoS filter shown in Figure 5-8 are presented in this section as a case study. The target stack dimensions for this filter are: Mo (100 nm)/ AlN (1 μm)/ Mo (100 nm)/ Si (5 μm). The top electrode geometry consists of 20 interdigitated fingers each 10 μm wide with a spacing of 5 μm (pitch of 15 μm). However, the actual dimensions of the fabricated filter deviate from the target design values. In particular, film thicknesses are critical and the silicon device layer of the SOI wafer used in this work has a thickness tolerance of ± 0.5 μm. Figure 5-15 shows a cross-section SEM view of the wafer stack at a location near the measured filter, revealing the actual thicknesses of the AlN and Si layers.

The measured film thicknesses for AlN and Si are used for the purpose of fitting the simulation results to the measured response. Initial simulations are performed taking the generally accepted published material properties for Mo, AlN and Si [62]. As will be seen later, the piezoelectric properties of reactively sputtered AlN deviate from bulk values and need to be accounted for in simulations. The actual properties of sputtered AlN are extracted from the fitted simulation response and are

used throughout this work to analyze the characteristics of TPoS filters. The simulated and measured filter response around the fourth-order thickness mode is plotted in Figure 5-16.

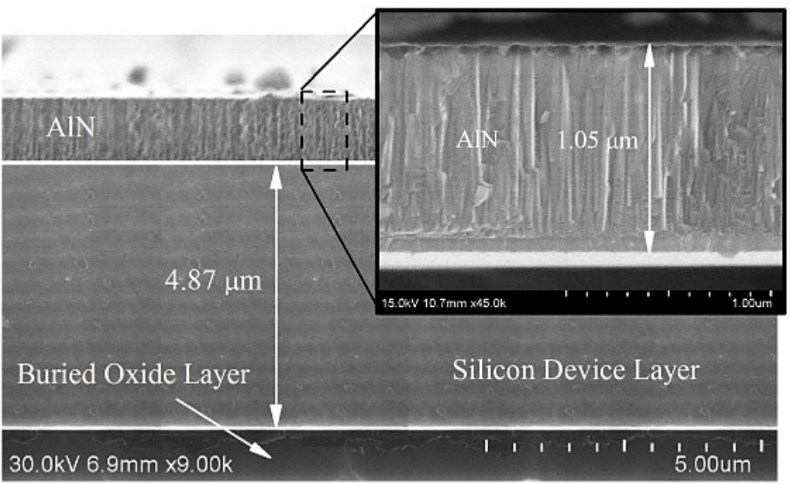

Figure 5-15: A cross-section SEM image of the stack. The measured film thicknesses are used in the fitted simulation. Note that the buried oxide layer and the handle layer are removed from under the filter area. Inset shows a close-up view of the AlN film.

The two simulated curves in Figure 5-16 represent the results obtained using nominal design parameters and the fitted parameters. The fabricated filter response shows a slightly different center frequency and roll-off as compared to the simulated response using nominal design parameters. In addition, the measured bandwidth is narrower than the simulated one using the target design parameters. This can be attributed to variations in the geometric parameters and material properties in the fabricated device as compared to target design values. With the geometric variations accounted for (through accurate SEM measurements), the difference between fitted and measured response can be attributed to variations in material properties only. Figure 5-17 shows the measured and simulated (fitted) phase of S_{21} for the filter shown in Figure 5-8.

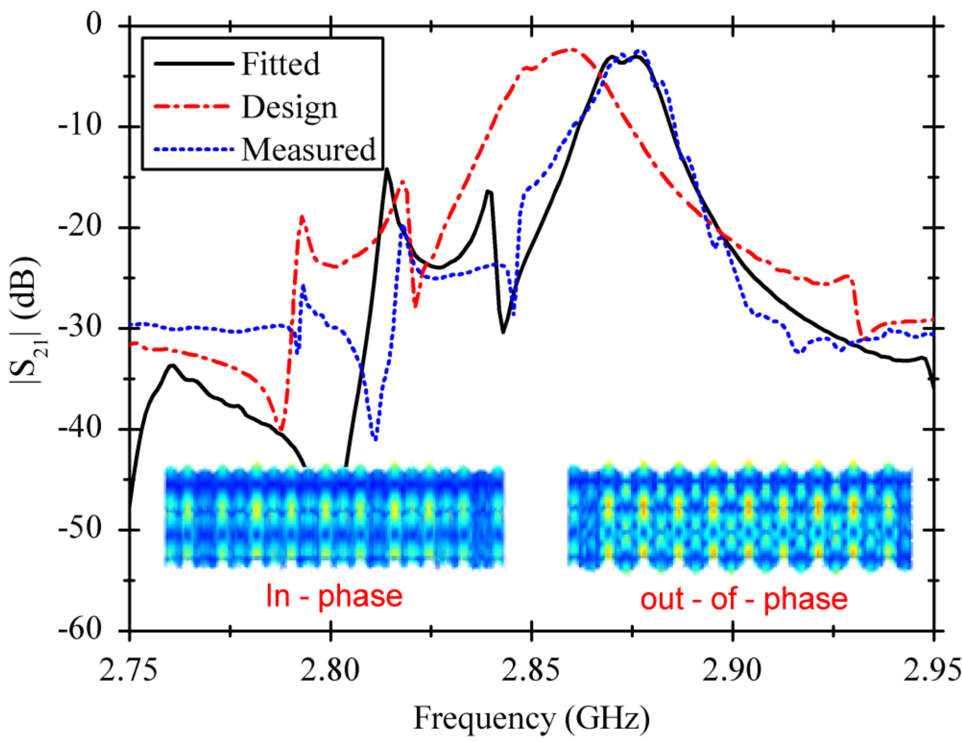

Figure 5-16: Frequency response near the fourth-order thickness mode of the filter shown in Figure 5-8. The design curve shows the simulation result considering the nominal design values and material properties. The fitted response involves variation of geometric parameters and the piezoelectric stress constant, e_{33}. Insets show harmonic response at the in-phase and out-of-phase frequencies.

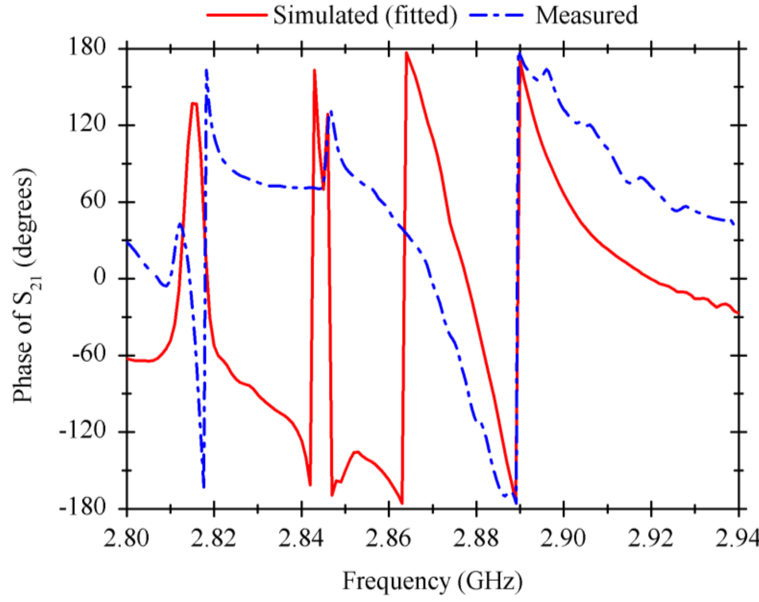

Figure 5-17: The measured and simulated (fitted) phase of the filter shown in Figure 5-8.

In TPoS filters, the frequency separation between the in-phase and out-of-phase modes primarily determines the bandwidth, which can be tailored to a large extent by changing the layout of the top interdigitated electrodes [87]. The piezoelectric stress constant, e_{33}, through the electromechanical coupling coefficient (k^2), determines the amount of energy converted from the electrical to the mechanical domain in each of the two electroded regions vibrating in thickness-extensional mode, and hence larger e_{33} values would make it possible for more charge to be collected at the output electrode with the same electric input signal. Depending on the sputtering conditions and seed material used, a wide range of e_{33} values have been measured for reactively-sputtered AlN [90], [91]. For example, e_{33} for AlN sputtered on Pt is extracted to be ~1.43 C/m^2 in [90], *i.e.* 94% of the bulk value (1.55 C/m^2). In addition, the exact orientation of the c-axis with respect to the wafer surface is not known. One can account for a non-vertical c-axis orientation by reducing the effective e_{33} value. To show the effect of e_{33} on the filter response, a set of simulations were performed by varying the AlN piezoelectric coefficient. Figure 5-18 shows the response when the piezoelectric stress coefficient, e_{33}, is reduced from 1.55 C/m^2 to 0.8 C/m^2. The bandwidth is a much better match for e_{33} of 1.1 C/m^2 for the deposited AlN film.

Table 5-3 lists some critical parameters used in the simulations. As a first approximation, this work assumes frequency-independent loss parameters. The loss parameters, or the damping ratio in the material, are set to match the measured insertion loss and Q of several filters on the wafer. These parameters are kept constant for the subsequent analysis presented.

Table 5-3: Parameters used in the finite element simulations.

	Acoustic damping	Dielectric loss tangent	Effective e_{33}
AlN	0.0015	0.001	1.1 C/m^2
Silicon	0.0005	-	-

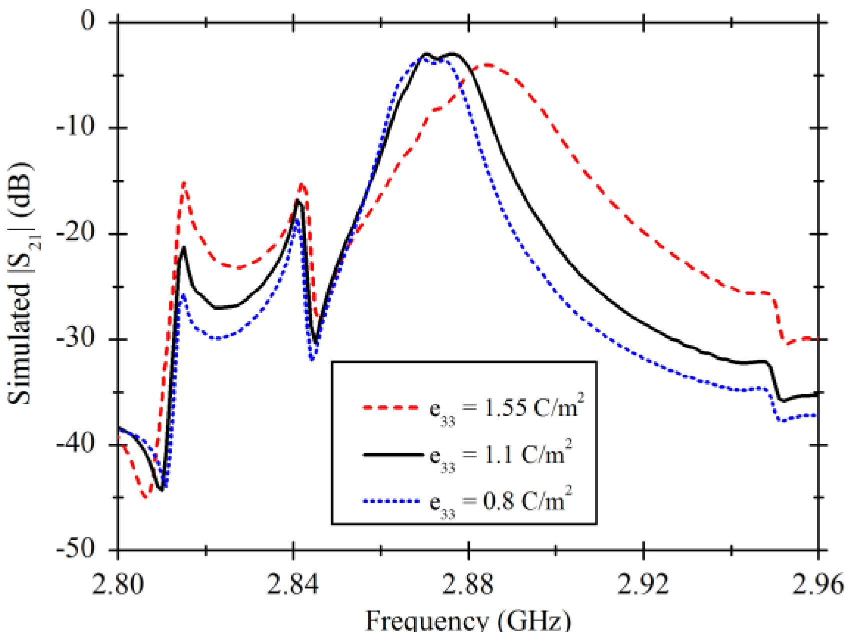

Figure 5-18: Simulated $|S_{21}|$ of the filter under varying AlN piezoelectric stress coefficient e_{33}. A reduced e_{33} of 1.1 C/m^2 is seen to best match the measured bandwidth and roll-off. The frequency shift seen with the increase in e_{33} may be attributed to the piezoelectric stiffening effect.

A significant advantage of finite element simulations over existing analytical techniques is the ability to predict secondary and spurious resonance modes with reasonable accuracy. Figure 5-19 (a) and (b) illustrate the measured and simulated second- and third-order thickness-mode responses showing good agreement.

To verify the general applicability of the model, the performance of a few devices on a particular die were also compared against simulations. Figure 5-20 presents the results, showing good agreement between the measured and simulated response of these devices.

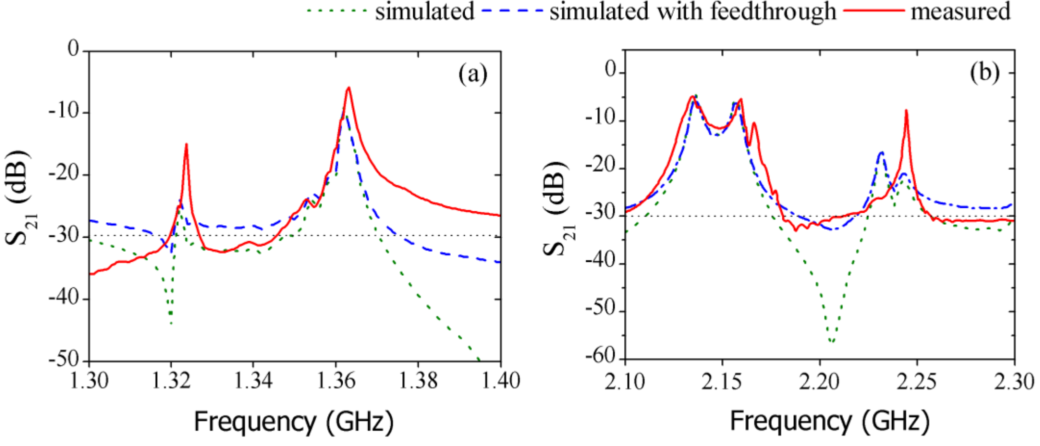

Figure 5-19: Simulated and measured filter response for (a) second and (b) third –order thickness-mode of resonance.

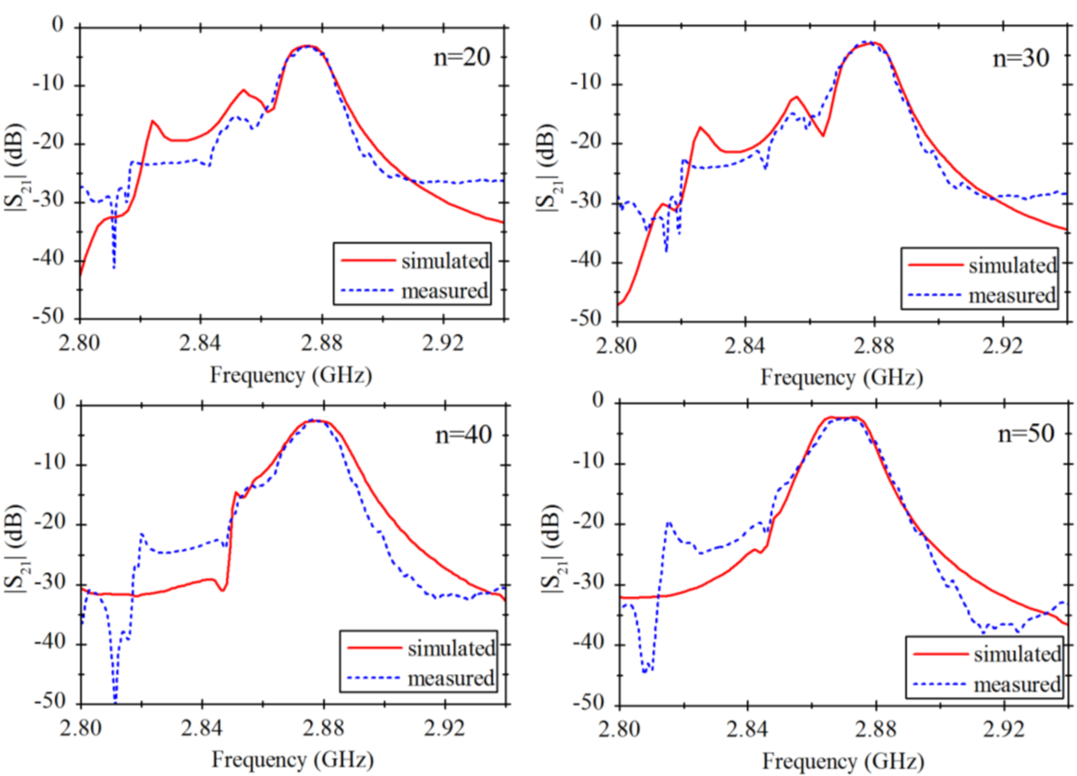

Figure 5-20: Comparison between the measured and simulated filter responses. All filters are on the same die. "n" is the number of electrode fingers. All devices have an electrode width in the range of 9.8 to 10.2 μm and finger spacing in the range of 4.8 to 5.2 μm with number of electrode fingers as shown in the plots. The actual thickness of the AlN and silicon layers as well as electrode dimensions were measured using SEM and used in these simulations. AlN e_{33} of 1.1 C/m^2 is used in all these simulations.

5.2.6 Design guidelines for acoustically coupled filters

From a review of available literature and from the results in Figure 5-20, it is clear that the filter performance is quite sensitive to the geometry of the top electrode layout [76], [78]. While the dispersion curves can provide an intuitive understanding of the effect of the top electrode layout on the filter performance, it fails to take into consideration the effect of other branches of the Lamb waves present at the frequency of interest. Such non-idealities make the electrode design process quite complicated and thus numerical tools are necessary to accurately predict the filter performance.

In the previous sections we characterized an AlN-on-silicon TPoS filter and used it to verify the accuracy and general applicability of the finite element simulation model. Here, we use the same model to obtain the frequency response of TPoS filters under varying geometric parameters for the interdigitated electrodes. This allows us to accurately estimate the geometric dependencies in the filter performance and will enable the design of filters with tunable passband characteristics. Based on the result of these simulations, we provide some design guidelines for achieving low-loss filters with varying percentage bandwidths.

5.2.6.1 Center Frequency

The center frequency has a strong dependency on the film thickness, which is expected considering that the device operates in its thickness mode. For a given stack, the trapping range is fixed by the cutoff frequencies of the electroded and the unelectroded regions (see Figure 5-3) and defines the frequency range in which a filter response may be designed. Therefore, varying lateral geometries can only marginally shift the center frequency of the filter within the lateral trapping range.

5.2.6.2 Bandwidth and Insertion Loss

Figure 5-21 shows the effect of varying interdigitated electrode spacing and number of electrode fingers on (a) the bandwidth and (b) the insertion loss of the filter. For this analysis, the electrode width is kept constant at 10 µm. The three curves represent three different electrode spacing values (3 µm, 5 µm and 7 µm). The bandwidth, taken at half power or -3 dB, is seen to increase as the electrode spacing is decreased. This is due to the stronger acoustic coupling between the electroded regions as the coupling is inversely proportional to the width of the coupling region (*i.e.* region without electrodes on top).

From Figure 5-21, it can be seen that for a given electrode width and spacing, the bandwidth remains fairly constant with large number of electrode fingers (number of electrode fingers > 32). However, as the number of fingers is increased beyond a certain point (40 in this case), the size of the device becomes too large and additional resonance modes corresponding to longer lateral wavelengths can get coupled, resulting in larger passband ripples causing a degradation of the insertion loss (Figure 5-23 (a)). Therefore, to obtain a low-loss and ripple-free passband, the electrode spacing has to be reduced and the number of electrode fingers has to be optimized using simulations.

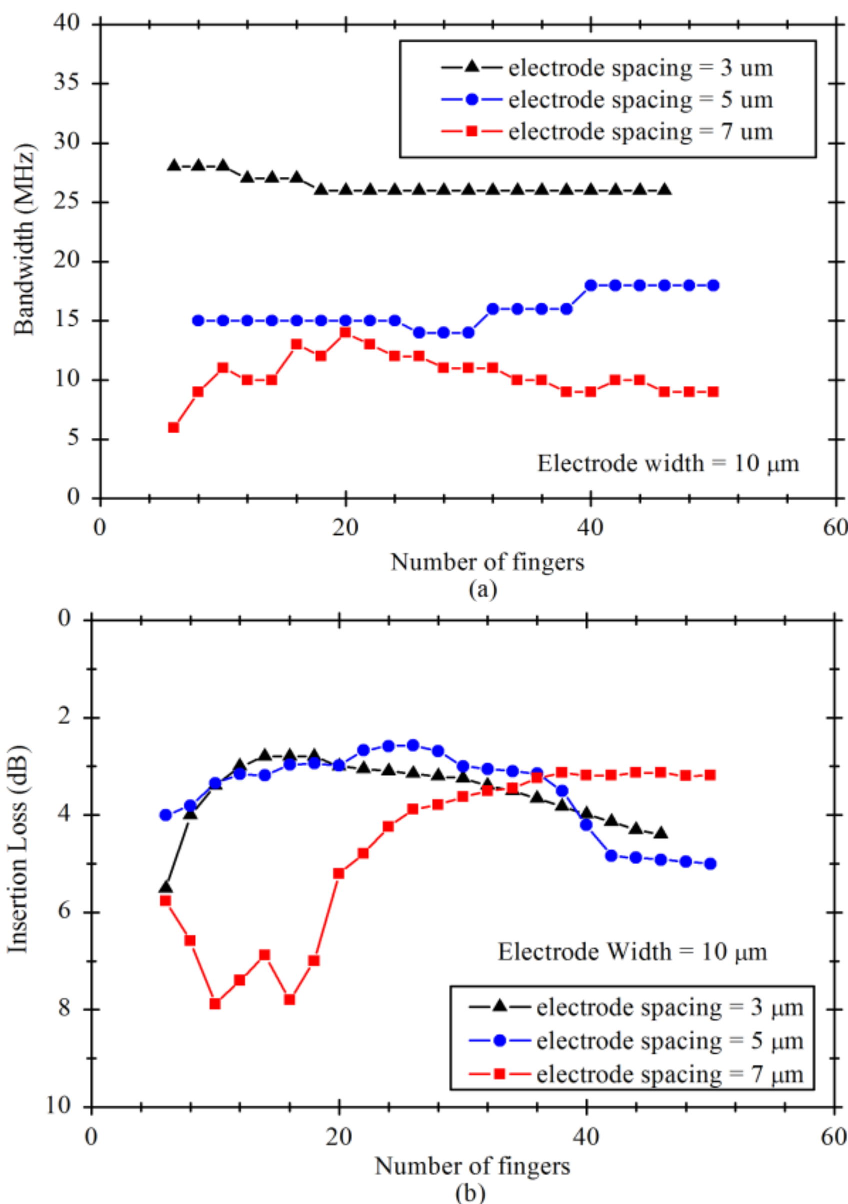

Figure 5-21: Simulated filter (a) bandwidth and (b) insertion loss versus number of fingers for different spacing between electrode fingers. The electrode width is kept constant at 10 µm. All filters are centered around 2.9 GHz.

A similar analysis is done to obtain the effect of variations in the electrode width. Figure 5-22 presents the simulated bandwidth and insertion loss as a function of number of electrode fingers keeping the spacing constant at 5 μm for three different electrode widths (10 μm, 12.5 μm and 15 μm). As seen from Figure 5-22, a smaller electrode width provides a wider bandwidth. From the dispersion curves shown in Figure 5-3, we can expect that as the electrode width decreases, frequencies of both the in-phase and the out-of-phase modes increase as a result of the shortened lateral wavelength. However, since the shift in the out-of-phase frequency is larger than the in-phase one (due to dispersion), the resulting bandwidth is wider. A further decrease in the electrode width causes the two resonance modes to move further away, and the passband ripple increases (beyond 3 dB) (see Figure 5-24). An electrode width of ~10 μm can provide a wide bandwidth without producing a large ripple in the passband.

From the analysis of the presented results we can say that smaller electrode spacing and narrower electrode width with sufficient number of electrodes produce a wider bandwidth and a lower insertion loss. In addition to the top electrode geometries, the piezoelectric coupling coefficient e_{33} of AlN plays an important role in determining the passband ripple and the bandwidth (Figure 5-23 (b)).

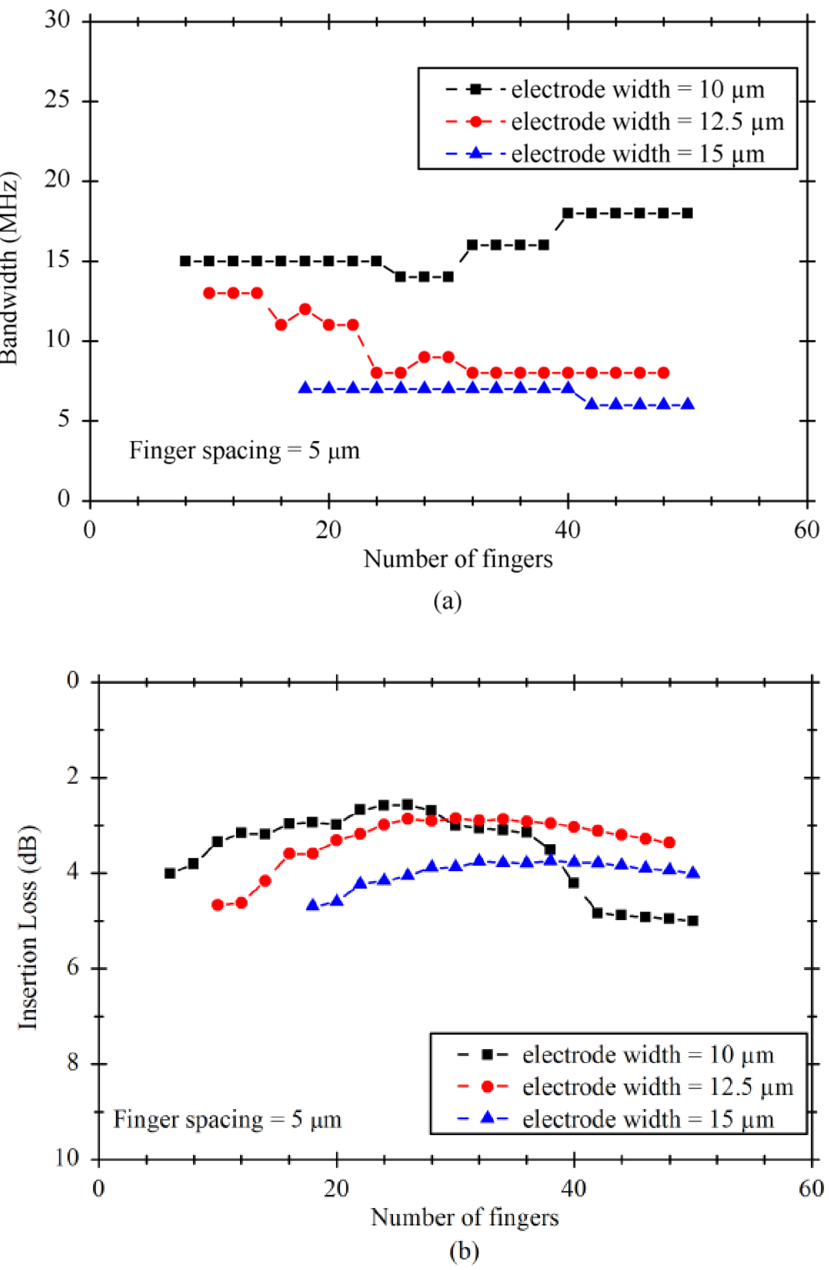

Figure 5-22: Simulated filter (a) bandwidth and (b) insertion loss versus number of fingers for different electrode widths. The electrode spacing is kept constant at 5 µm. All filters are at ~2.9 GHz.

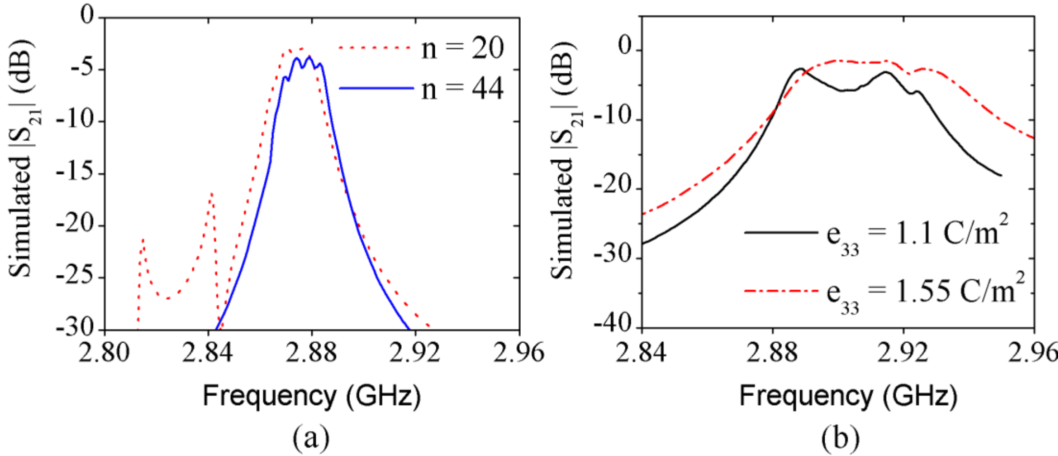

Figure 5-23: (a) Simulated filter response for n=20 and n=44 showing the generation of additional unwanted resonances in the passband as the number of fingers is increased beyond 40. For both curves the top electrode has a width of 10 µm and spacing of 5 µm. (b) Simulated effect of reduced piezoelectric stress constant in AlN. For both curves, the top electrode consists of 20 electrodes each 5 µm wide and having a spacing of 5 µm.

Figure 5-24 depicts the effect of top electrode geometry on the filter response, visualizing the results presented in Figure 5-21 and Figure 5-22. As shown, with the same stack thickness and material properties, the bandwidth of the filter can be designed to be anywhere between 0.2% and 1% having an insertion loss of less than 5 dB and passband ripple of less than 1 dB. The ripple can be reduced by changing the thickness of the top electrode, as shown in Figure 5-25. Increasing the electrode thickness results in a smaller bandwidth and a flatter passpand because of the higher energy trapping in the electroded regions and smaller coupling between them. Further increase in the electrode thickness (beyond an optimum value) results in increased insertion loss as shown in Figure 5-25 (inset).

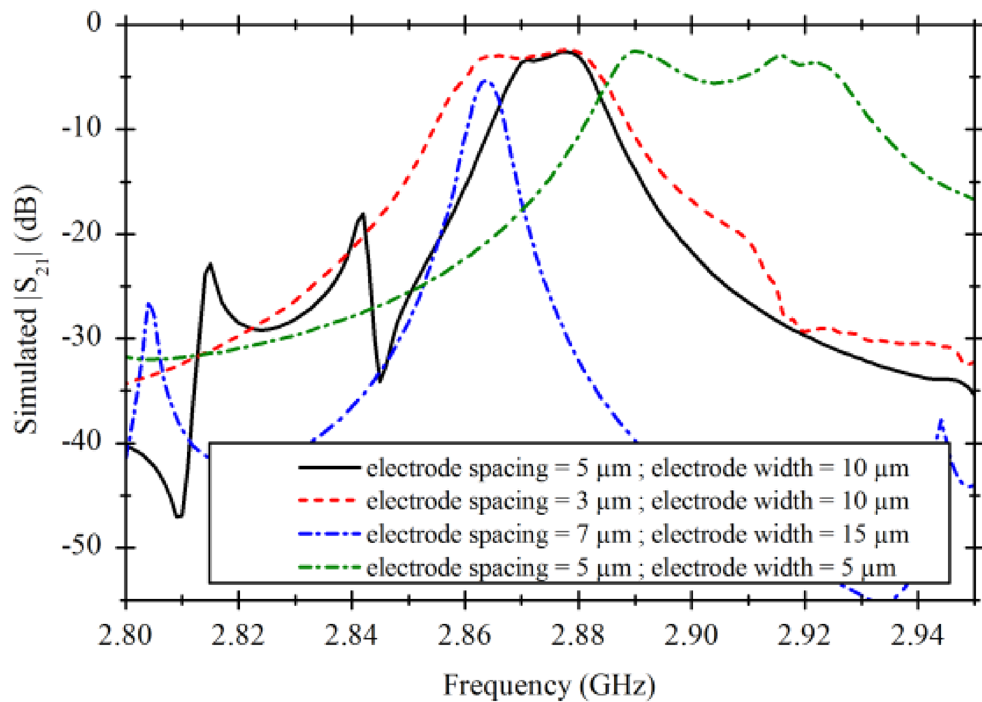

Figure 5-24: Simulated filter response indicating the effect of electrode width and electrode spacing. The top electrode layout is as marked. The number of electrode fingers is 20 in all cases.

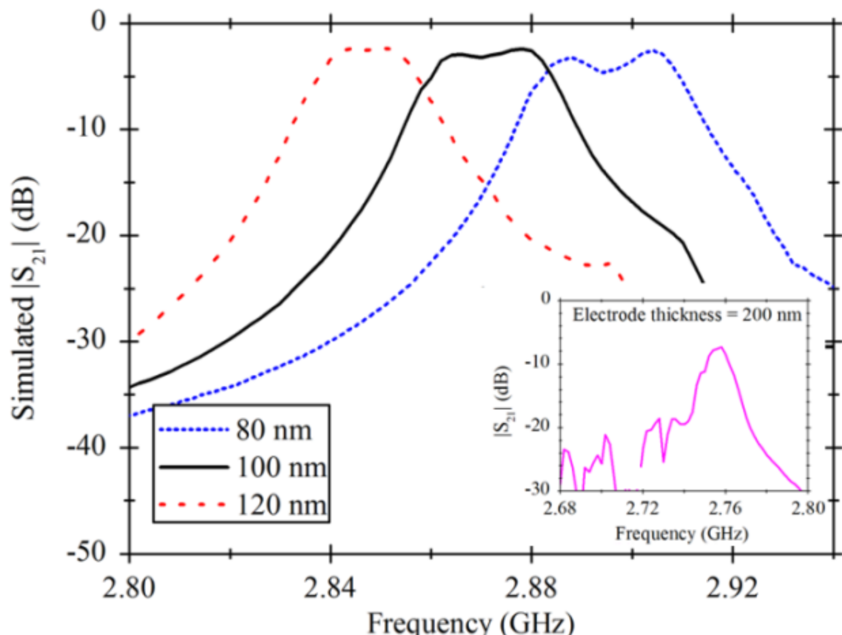

Figure 5-25: Simulated response of a TPoS filter indicating the effect of the electrode thickness on the passband ripple. Increased electrode thickness improves the coupling and can reduce the ripple. Inset shows the filter response with electrode thickness of 200 nm.

In an earlier work on acoustically coupled ZnO-on-Si TPoS filters, it was shown that the bandwidth increased as the number of electrode fingers was increased [78]. In that case, the total device area and the electrode spacing were kept constant and the number of interdigitated electrode fingers was gradually increased. This implies that the electrode width decreases as the number of fingers increases. To verify this observation, simulations were setup for AlN filters and the results are plotted in Figure 5-26.

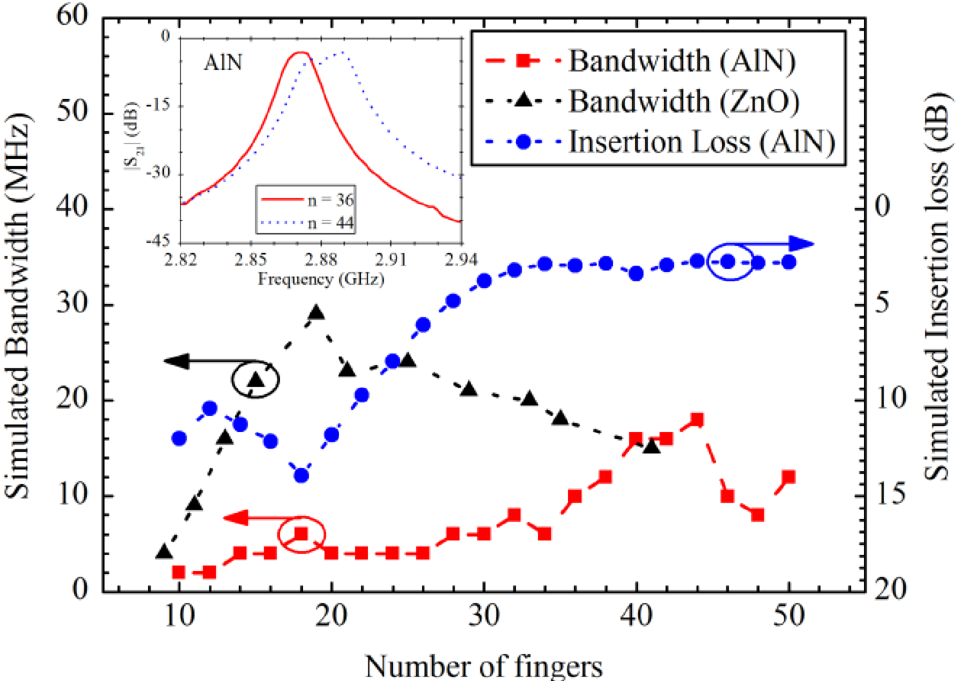

Figure 5-26: Simulated filter bandwidth and insertion loss versus number of electrode fingers. For AlN-on-Si, the total device width is kept constant at 595 μm and interdigitated finger spacing is fixed at 5 μm. In case of ZnO the device width is 260 μm and finger spacing is 3 μm. In both cases, as the number of fingers is increased, the electrode width is decreased. The results for AlN are at ~2.9 GHz while those for ZnO are at ~1.8 GHz.

It can be seen that the bandwidth indeed increases as the number of fingers is increased from 26 to 44 but this trend does not hold for other regions of the plot. A similar simulation was performed with ZnO. Similar to AlN the bandwidth of ZnO-

on-Si filters is seen to be a function of the number of fingers, having a positive slope only in a specific range. Depending on the stack material and geometric configuration, the range of fingers for which such a relation is seen varies. Thus, by adjusting the number of fingers, the bandwidth of the filter can be controlled to some extent.

To observe the effect of the thickness ratio of silicon to AlN on the filter bandwidth, simulations were performed with thickness ratio of 3:1 and results are compared with the presented work, *i.e.* thickness ratio of 5:1. For both cases, the AlN film thickness is taken to be 1 μm and thus the Si layer thickness is 3 μm and 5 μm, respectively. The top electrode layout is kept the same in for both and an exemplary result is plotted in Figure 5-27.

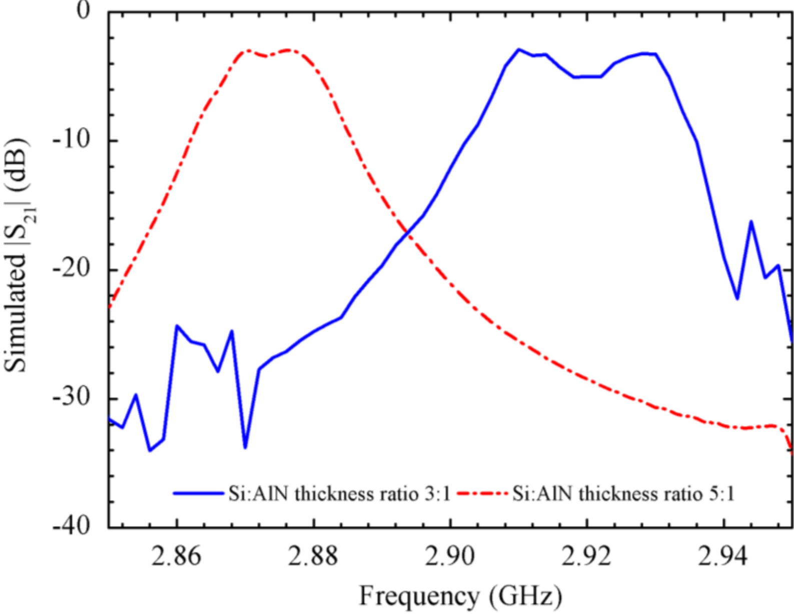

Figure 5-27: Simulated effect of silicon to AlN thickness ratio on the filter response. For both simulations, the top electrode geometry consists of 20 electrode fingers each 10 μm wide with 5 μm spacing in between. The AlN film thickness is 1 μm in both cases. A wider bandwidth with a larger ripple can be clearly seen for the stack with reduced silicon to AlN thickness ratio.

From the two curves, a larger frequency separation between the in-phase and out-of-phase modes and thus a wider bandwidth can be seen for a lower Si to AlN thickness ratio.

5.3 In-plane acoustically coupled filters

In the case of thickness-mode filters, we utilized the thickness-mode of resonance to set the filter operating frequency and achieved the mode coupling in one of the lateral directions. In order to enable multiple frequencies on the same die, it is possible to modify the thickness of the silicon layer through local oxidation and subsequent etching [80]. However, one drawback of this approach is the need to run a separate oxidation step for each target frequency. A second limitation is in the attainment of much lower frequencies below 200 MHz. Such filters will require the use of extremely thick silicon device layer and will significantly reduce the coupling coefficient due to the relatively small ratio of AlN to silicon. An alternative approach can utilize in-plane extension modes, wherein the filter frequency is defined by one lateral dimension with the lateral coupling achieved in the second in-plane dimension.

5.3.1 Design of an in-plane acoustically coupled filter

Contour-mode resonators utilizing the in-plane geometry to set the resonator frequency have been widely investigated in the literature [18], [59]. Such modes can be designed to have a large frequency range between 10 MHz to over 500 MHz while keeping the same device thickness. Figure 5-28 shows a schematic of an in-plane acoustically coupled filter. The dispersion curves for this structure around the first order width-extension mode are shown in Figure 5-29. Figure 5-30 plots the fundamental width extension mode and its first overtone.

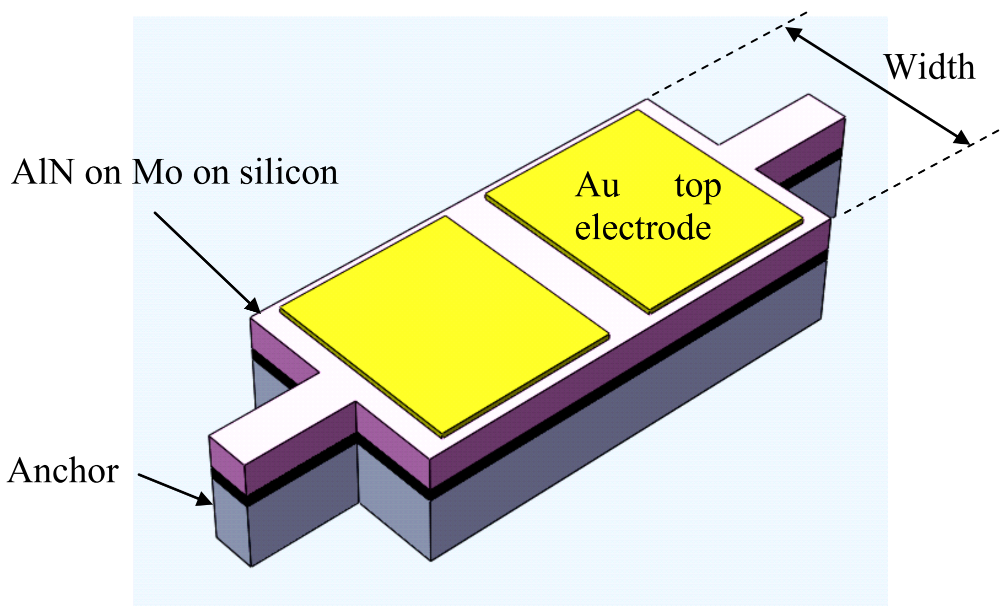

Figure 5-28: Schematic of an AlN-on-silicon contour-mode filter. The width of this structure is 200 µm. The device has the following stack geometry: 20 µm silicon, 100 nm Mo, 1 µm AlN and 100 nm of Au as the top electrode. (Not to scale)

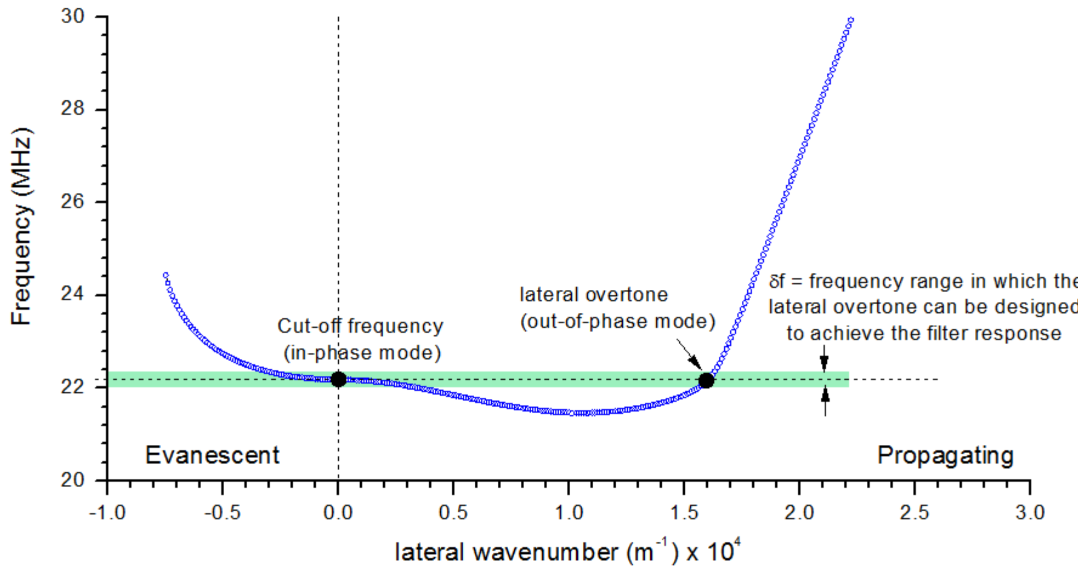

Figure 5-29: Dispersion curves around the first order width-extension mode for the device geometry shown in Figure 5-28. The lateral overtone *i.e.* the out-of-phase mode can be designed to have a range of frequencies through the design of the plate length. The highlighted zone shows the frequency range in which the overtone mode should be designed to achieve a coupled filter response.

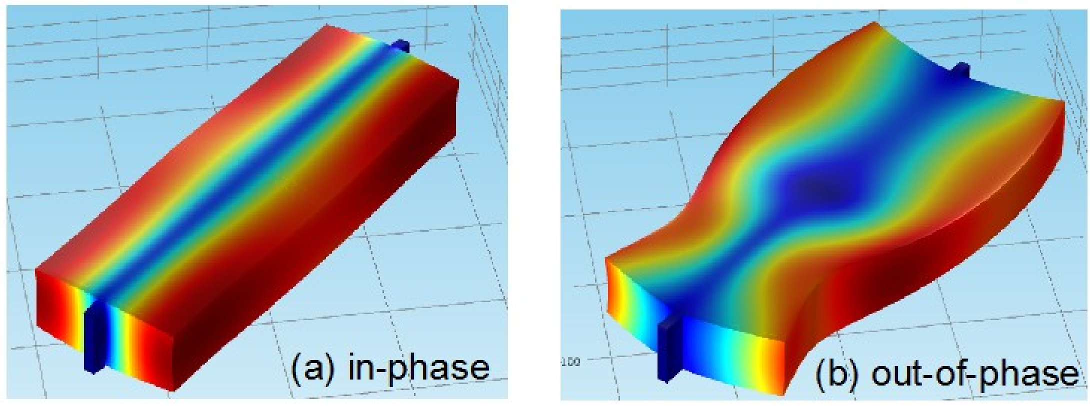

Figure 5-30: Simulated (a) in-phase *i.e.* the fundamental width-extension mode and (b) out-of-phase *i.e.* the first lateral overtone of the width-extension mode.

The cut-off frequency *i.e.* the frequency of the fundamental width-extension mode, defined by the plate width, can be clearly identified in the plot. The lateral geometry determines the frequency of the overtones of the width-extension mode. By increasing the length of the plate, the frequency of the out-of-phase mode follows the frequency given by the dispersion curve. This can be seen more clearly from a modified view of the dispersion curve shown in Figure 5-31, in which the frequency is plotted as a function of the lateral wavelength as opposed to lateral wavenumber. As the plate length is reduced, *i.e.*, the lateral wavelength is reduced, the frequency of the out-of-phase mode decreases until the knee region. Beyond this point, the frequency of the out-of-phase mode increases sharply as the plate length (*i.e.*, wavelength) decreases.

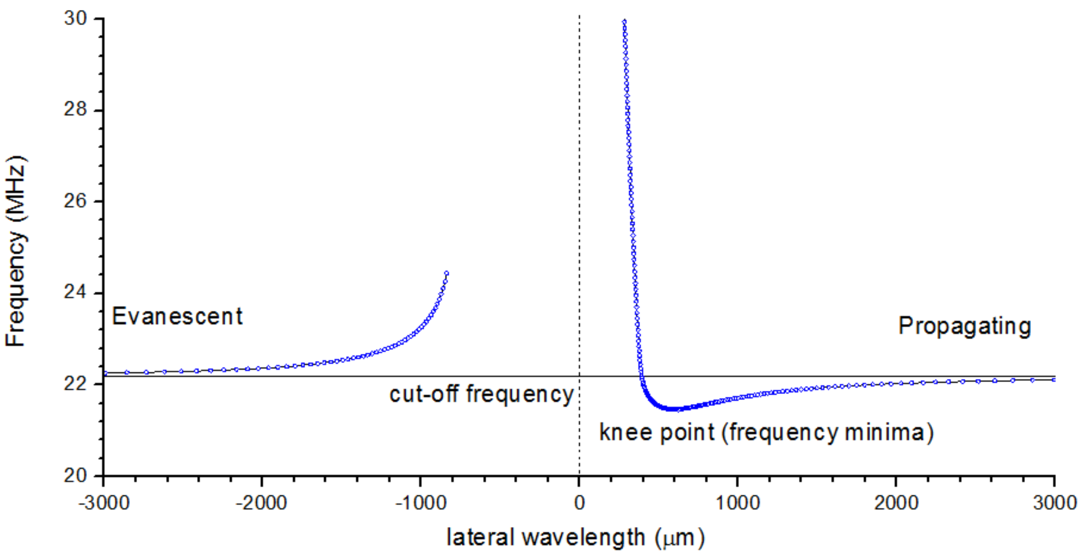

Figure 5-31: Modified representation of the dispersion curves shown in Figure 5-29 with filter frequency plotted as a function of the lateral wavelength as opposed to the lateral wavenumber..

5.3.2 Finite element modeling of the filter response

Using the simulation model verified earlier with the thickness-mode filters, the in-plane acoustically coupled filter is designed and its frequency response is estimated. Figure 5-32 plots the simulated $|S_{21}|$ and its phase for the device configuration shown in Figure 5-28. The simulation result in Figure 5-32 shows a filter with a bandwidth of 10 kHz with an insertion loss of 0.5 dB. Such a filter is ideally suited to clean up the frequency spectrum at the output of the mixer stage in the multi-resonator clock architecture, described in Chapter 3.

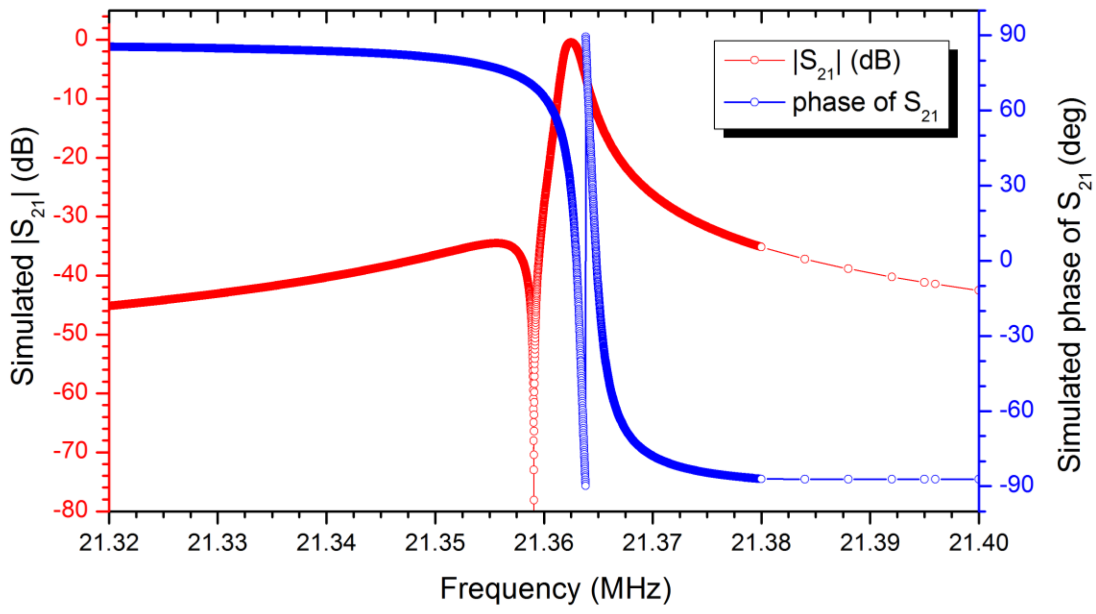

Figure 5-32: Simulated magnitude and phase of the S_{21}, for the in-plane filter shown in Figure 5-28. The filter has a plate width of 200 µm and plate length of 423 µm. The top electrode geometry consists of 2 electrodes with a gap of 10 µm.

5.3.3 Measured Results

In order to verify the performance of the in-plane filters, devices were fabricated on a 20 µm thick silicon device layer of a high-resistivity SOI wafer. This also ensures that the filters can be successfully integrated with the resonators presented in the previous chapters. The process flow utilized is similar to the one used for the coupled-ring and Lamé-mode resonators and is depicted in Figure 5-33. A SEM image of a fabricated filter is shown in Figure 5-34.

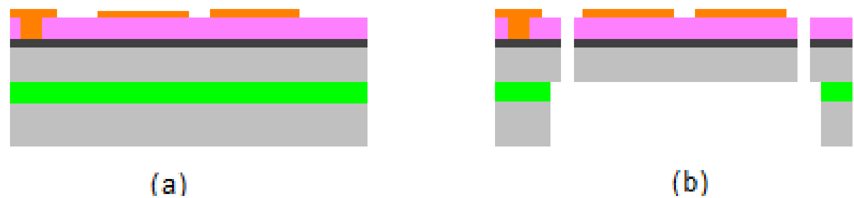

Figure 5-33: Process flow used in the filter fabrication. (a) Deposit and pattern Mo (100 nm) as bottom electrode, 1 µm AlN as the piezo layer, and lift-off pattern Cr/Au (10/90 nm) as top electrode. (b) Etch resonator contour (RIE and DRIE) to get self-aligned devices and release from backside using DRIE and etch BOX layer using BHF.

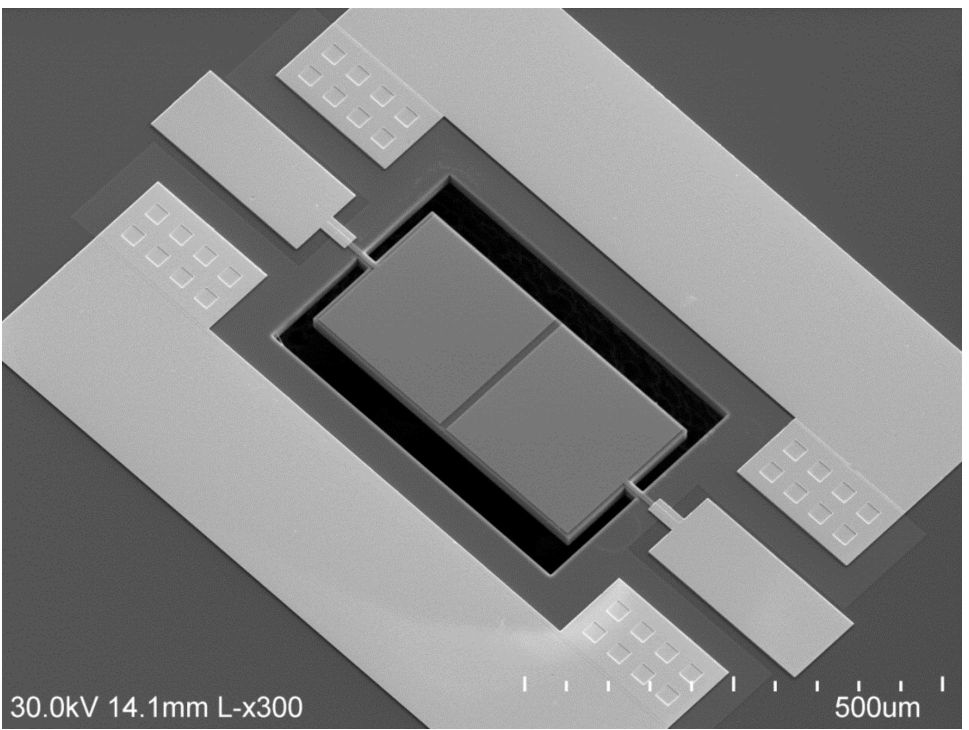

Figure 5-34: SEM image of a fabricated AlN-on-silicon in-plane acoustically coupled filter.

This filter response is measured in air and at room temperature (Figure 5-35). The filter has an insertion loss of 13 dB at 21.19 MHz with bandwidth of 4.3 kHz.

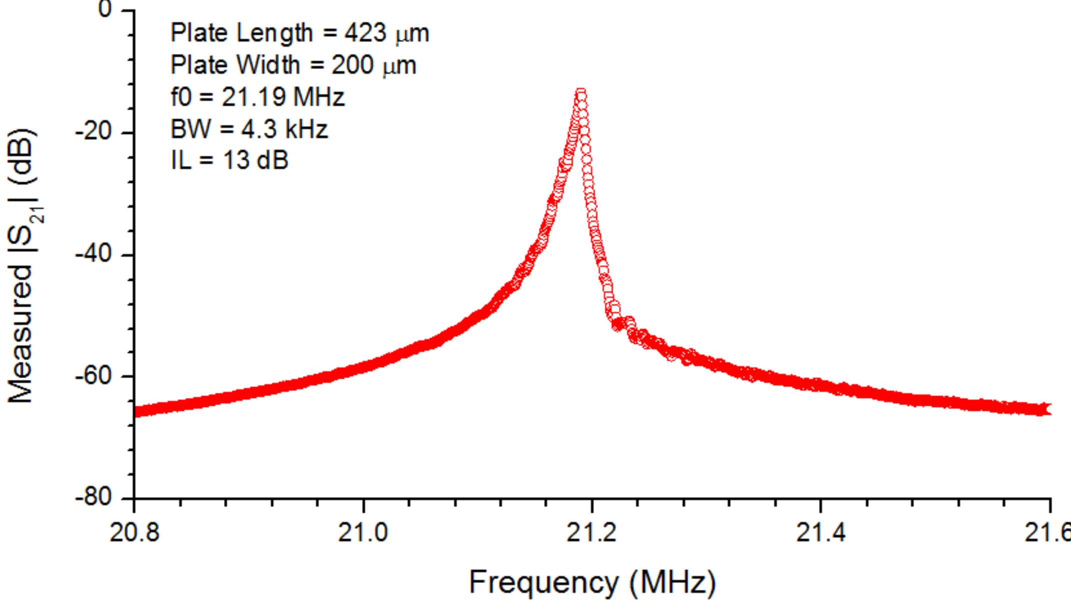

Figure 5-35: Measured $|S_{21}|$ of the filter shown in Figure 5-34. This device has plate width of 200 μm and plate length of 423 μm.

From the plot in Figure 5-31, we expect a relatively large shift in the frequency of the out-of-phase mode with small changes in the plate lateral geometry (length in this case). This can be verified from the measured results of two filters with plate length of 420 μm and 426 μm shown in Figure 5-36. A 6 μm change in plate length can be seen to shift the frequency of the out-of-phase mode by 100 kHz. As expected, the frequency of the in-phase mode does not change with the lateral geometry.

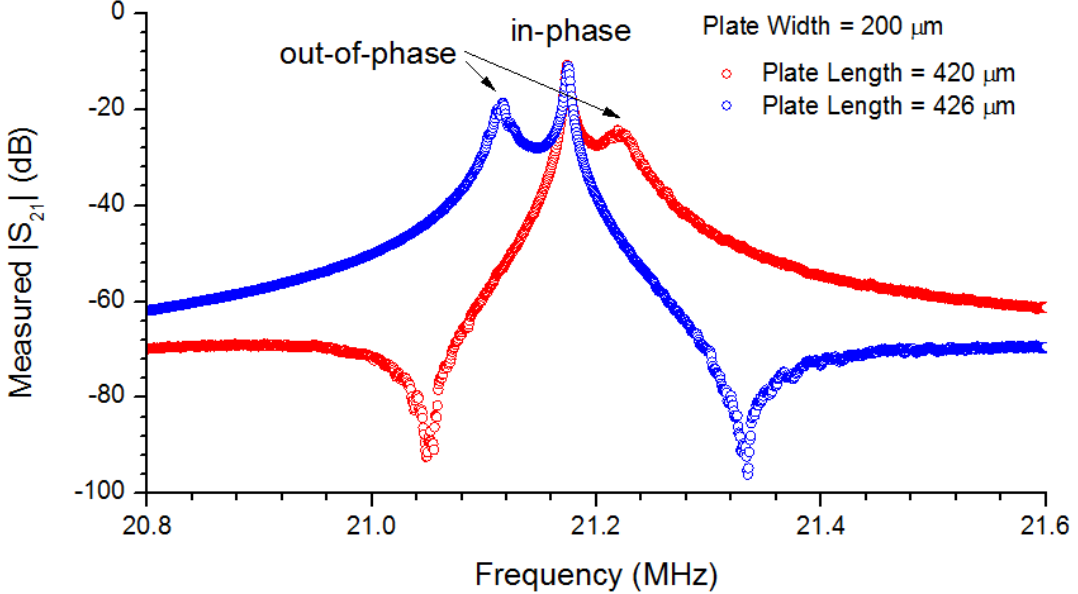

Figure 5-36: Measured $|S_{21}|$ for two filters with plate width of 200 μm and plate length of 420 μm and 426 μm. We see a 100 kHz shift in the out-of-phase mode with the change in the plate length in accordance with the nature of the dispersion curves of the width extension mode shown in Figure 5-31. The in-phase frequency is insensitive to the plate length and measured to be similar for both filters.

5.3.4 In-plane filters: Merits and Challenges

SAW devices working with Rayleigh waves require large device sizes on the order of a few millimeters to achieve low-frequency filters with a low insertion loss [92]. This is due to the relatively smaller wave velocity of the surface waves. More

importantly surface acoustic waves are non-dispersive in nature, *i.e.*, their velocity does not change with frequency [93]. On the other hand, acoustically coupled bulk wave filters show a strong dispersion character which is highlighted from Figure 5-31. At wavelengths smaller than the knee point, we note a very large change in frequency of the width-extension mode for a relatively small change in the wavelength. This allows us to achieve a low loss filter response in a much smaller device size as compared with SAW filters. However, the relatively sharp frequency-wavelength characteristics also give rise to a large sensitivity of the filter response to the device geometry. A small change in the plate length, leads to a relatively large frequency shift between the in-phase and out-of-phase modes of the filter leading to a weakly coupled system and a non-ideal filter response with a large passband ripple (Figure 5-36). More analysis of the dispersive properties of stack materials is necessary to overcome these challenges. In cognizance of the fact that the nature of dispersion is strongly dependent on the Poisson's ratio of the materials [93], acoustic engineering of the stack geometry and materials may help in changing the nature of the dispersion curves to reduce the slope of the frequency-wavelength curve, thus improving the device robustness against fabrication tolerances.

Another alternative could be to use higher order overtones to determine both the in-phase and out-of-phase modes of the filter. Using this approach, while the center frequency of the filter will be sensitive to the fabrication induced variations; the filter bandwidth will be relatively robust as both the coupled modes will see an equal frequency shift with small changes in plate geometry, similar to the case of the thickness-mode filter analyzed in Section 5.2.

5.4 Conclusions

Acoustically coupled AlN-on-silicon filters feature a smaller chip size compared to ladder-type electrically coupled filters. These features in addition to their excellent linearity at elevated RF power levels make them ideal candidates for applications in commercial handheld devices.

Thickness-mode acoustically coupled filters have been analyzed using finite element modeling and a low-loss proof-of-concept AlN-on-silicon bandpass filter is demonstrated. The finite element model is used to generate design guidelines to enable the design of filters with controlled specifications. These results are explained in the context of the stack dispersion characteristics, which determine the operation of such acoustically coupled filters.

To enable low-loss filters in the low MHz frequency range, use of in-plane extensional modes is explored. Utilizing the analysis presented for the thickness-mode filters and using the dispersion curves for the width-extension mode, an in-plane filter utilizing the fundamental width-extension mode is designed and fabricated with measured characteristics shown to be suitable for use in the multi-resonator clock.

Acoustically coupled filters can be monolithically integrated with AlN-on-silicon resonators. By utilizing the dispersive properties of Lamb waves, bandpass filters with sharp skirt angles, low insertion loss and having a relative bandwidth between 0.2 % to 1 %, across a large frequency range between a few MHz up to a few GHz can be enabled in a small device footprint. Such devices are crucial in the development of next generation wireless communication systems that need to support multiple communication standards within a miniaturized handheld device.

In summary, this chapter includes the following research contributions:

- A low-loss thickness-mode filter is presented as a potential solution to filtering requirements in modern communication systems
- A detailed analysis of such acoustically coupled filters is implemented culminating in some useful design guidelines.
- A novel filter design utilizing in-plane modes is presented for low-frequency applications, such as in the proposed multi-resonator clock. A filter with center frequency of 21 MHz and bandwidth of 4.3 kHz is demonstrated as a potential solution to the signal filtering required at the mixer output in the clock system.

Chapter 6 FUTURE WORK

6.1 Summary

This thesis described a novel timing reference algorithm utilizing multiple temperature-compensated silicon resonators and addressed the main requirement of this clock algorithm *i.e.* development of multiple resonators with unique frequency-temperature characteristics built in a common process flow. Multiple temperature-compensated and piezoelectrically actuated AlN-on-silicon resonators having characteristics ideally suited to the development of the clock were demonstrated. Using low motional impedance ring resonators, oscillators were built and their temperature performance was characterized. Using these oscillators along with n-PLLs and mixers, a proof-of-concept clock implementation is demonstrated with total temperature-induced frequency shift of < 8 ppm across -20 °C to +50 °C.

The second aspect of this thesis focused on the analysis and development of acoustically coupled filters using the same AlN-on-silicon stack for use in the multi-resonator clock. Their excellent performance characteristics achievable in a small footprint make them ideally suited for use at low frequencies in lieu of SAW filters. An in-plane acoustically coupled filter is demonstrated at 21 MHz with a bandwidth of 4.3 kHz for use in the clock system. Through the use of the in-plane contour and out-of-plane thickness-mode of operation, these filters can target a broad range of frequencies making them ideally suited for use in modern communication systems.

6.2 Future Research Directions

In the course of completing this thesis, a number of important insights were obtained for both resonators and filters. This section highlights some research directions that hold significant potential.

6.2.1 Clock Implementation

Chapter 3 of this thesis described our efforts at implementing a clock system using the temperature-compensated MEMS oscillators along with generic evaluation boards to achieve the mixer and multiplication functions. Implementing the mixer and n-PLL functions in an application specific integrated circuit (ASIC) will allow much improvement in the system performance and significant reduction in the total power consumption. Secondly, we note a small temperature dependence of ~ 8 ppm in the system output which is attributed to errors during the calibration of the individual oscillators. An integrated MEMS and circuit solution will provide improved calibration accuracy and will truly enable a temperature insensitive clock output.

6.2.2 AlN-on-Silicon Lamé-Mode Resonators

In Chapter 4, it was shown that the piezoelectric actuation of the Lamé-mode resonator is enabled through the inclusion of oxide islands within the resonator. While we were able to demonstrate the reliable actuation of this mode, its motional impedance was still high for use in low-power oscillators. Since Lamé-mode resonators have demonstrated the highest measured Q for thin-film piezoelectrically actuated micro-resonators, they hold a lot of potential for use in low-power and low-noise timing references. From the analysis of the Lamé-mode devices, it was shown

that due to the presence of oxide islands, the resonator *Q* is loaded between 60,000 to 400,000 while the piezoelectric interface loads the *Q* down to 16,000 to 77,000. From these results we note that in case of piezoelectrically actuated resonators, the device *Q* is primarily limited by the metal-piezoelectric interface. A reduction in the interface dissipation is thus expected to provide a significant improvement in the device *Q*. While the mechanism of this interface dissipation is as yet uncertain, from the measured data of devices with and without polysilicon (Chapter 4 Section 4.2.2), we can hypothesize that the effect of interface loss can be reduced by replacing the metal electrodes with doped silicon in the stack. Doped amorphous silicon can be deposited at low temperatures; thereby, potentially improving the device *Q* while maintaining a low-temperature process. Another alternative is through the use of Nickel Silicide (NiSi) as the electrode material. The formation of NiSi has been widely investigated in literature [71]; NiSi can also be formed at temperatures below 300 °C, thus maintaining the CMOS compatibility of the process.

From the measured *Q* *vs.* insertion loss trends shown in Figure 6-1, the insertion loss for Lamé-mode resonators is seen to have a strong dependence on the resonator *Q*. As can be seen from the linear fit to the data, a *Q* of 60,000 can reduce the insertion loss to less than 40 dB while an increase in *Q* to 100,000 can help achieve an insertion loss of only 10 dB. Thus, the use of novel electrode materials may help improve the *Q* and insertion loss of the Lamé-mode resonators; thereby, enabling low-power and low-noise temperature-insensitive clocks. In addition, the data for device *Q* as a function of electrode materials may provide a better

understanding of the mechanism of interface dissipation, which seems to be the dominant *Q* limiting mechanism in piezoelectrically actuated micro-resonators.

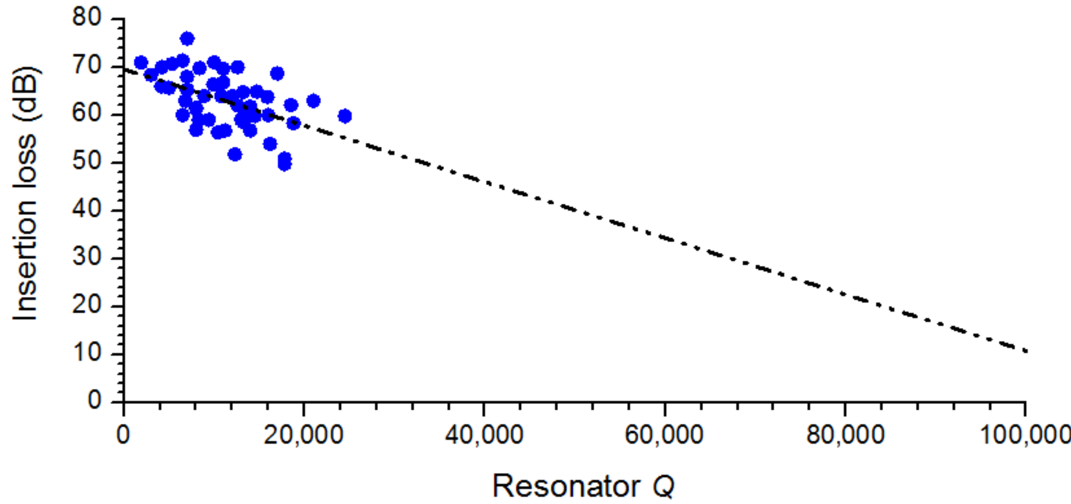

Figure 6-1: Measured insertion loss of piezoelectrically-actuated Lamé-mode resonators as a function of its *Q*. The black line represents a least squares fit to the measured data.

6.2.3 In-Plane Acoustically Coupled Filters

In Chapter 5, we analyzed the performance of acoustically coupled filters and presented a novel in-plane topology to achieve low-frequency and small-size filters. While this topology can achieve the required filter specifications, the sensitivity to geometric parameters, particularly the lateral plate geometry is noted to be high. This may lead to considerable changes in the filter performance depending on the process tolerances.

The origin of this geometric sensitivity may be explained with the use of the dispersion curves for an elastic plate. The dispersion curves are known to be strongly influenced by the Poisson's ratio of the plate material. Within the AlN-on-silicon platform, silicon being a cubic crystal demonstrates a strong orientation dependence of its elastic properties [36]. Figure 6-2 plots the dispersion curves and the rate of

frequency change with wavelength for a 200 μm wide silicon plate oriented along the (a) <100> and (b) <110> crystallographic directions in silicon. From Figure 6-2, we can note that around the design point (*i.e.*, for plate length to have out-of-phase frequency close to the in-phase frequency), the change in frequency with wavelength is much sharper along the <100> crystal orientation. As a result, the geometric sensitivity may be reduced by orienting the filter at 45° to the primary flat, *i.e.* by orienting the filter along the <110> crystal axis.

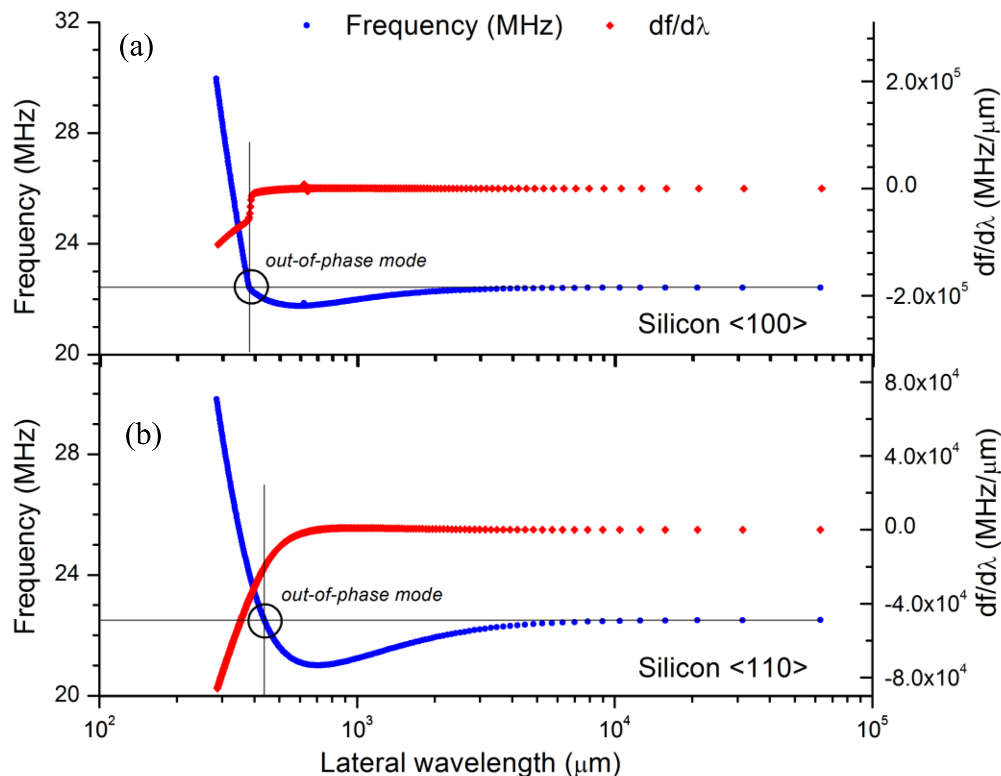

Figure 6-2: Plot of frequency *vs*. wavelength and the rate of change of frequency with wavelength for a silicon plate oriented along (a) <100> and (b) <110> crystal axis.

Apart from material parameter variations, it is also possible to acoustically engineer the geometry of the filter plate. Examples of acoustic engineering have been demonstrated in literature especially in the case of resonators to eliminate the

spurious resonance modes. Similar techniques may be used to obtain more lucrative Lamb wave dispersion characteristics suitable for robust filter implementations.

While this thesis restricts the application of in-plane acoustically coupled structures to low-frequency filters, in principle they may be used quite effectively at higher frequencies. By utilizing the higher order contour modes, frequencies higher than 1 GHz are easily attainable and resonators working in this frequency range have been successfully demonstrated [59]. Implementing in-plane filters in this frequency range would require the use of modified top electrode geometries. Figure 6-3 shows an example of a top electrode layout that may be used to actuate the third-order width-extension mode for signal filtering. Such filters will truly enable the signal processing requirements for multi-standard radios within a single AlN-on-silicon implementation.

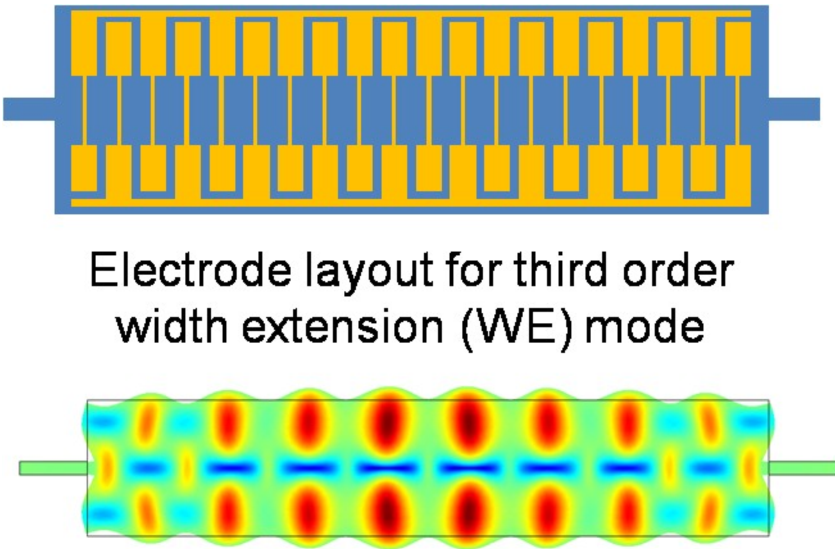

Figure 6-3: (Top) Top electrode layout that may be utilized to implement a third order width-extension mode filter. (Bottom) Simulated mode shape for the 19th overtone of the third-order width-extension mode.

APPENDIX A-1 DISPERSION CURVES

Experimental data and the subsequent analytical modeling effort on the propagation of seismic waves in the late 19th and early 20th century revealed the frequency dependent wave velocity characteristics of Lamb waves propagating in layered media. Over time this feature has been used extensively to estimate the elastic properties of materials and in fault detection in the field of non-destructive testing. With the advent of Quartz and subsequently the development of FBARs, this field has found applications in miniaturized devices to study the permissible Lamb modes that may be useful in device applications. While FBARs require the elimination of the secondary or lateral modes in order to obtain spurious free resonators, these lateral modes are essential in the development of acoustically coupled filters.

As has been discussed in Chapter 5, dispersion curves allow us to study the relationship between the lateral wavelength and frequency for the lateral modes and thus help us to design appropriate filter geometries. The computation of the dispersion curves requires a precise knowledge of the different materials in the stack and their material properties. For the sake of completeness, in this section we detail the steps necessary in the computation of the dispersion curves [84].

For a *plane wave* propagating in an elastic medium, the equation of motion may be written as,

$$\rho \frac{\partial^2 \boldsymbol{u}}{\partial t^2} = (\lambda + \mu)\nabla(\nabla.\boldsymbol{u}) + \mu\nabla^2\boldsymbol{u}, \qquad \text{Equation A1-1}$$

where, λ and μ are Lamé elastic stiffness constants, u denotes the displacement along coordinates x, ∇ is the vector operator, and ∇^2 is a scalar operator.

The solution for Equation A1-1, can be written as,

$$\phi = A_L e^{i(\boldsymbol{k}.\boldsymbol{x}-\omega t)}, \qquad \text{Equation A1-2}$$

$$|\psi| = A_S e^{i(\boldsymbol{k}.\boldsymbol{x}-\omega t)}, \qquad \text{Equation A1-3}$$

where ϕ and ψ are the respective scalar and vector functions, A_L and A_S are the longitudinal and shear wave amplitudes, respectively, $\boldsymbol{k}$ is the wavenumber, and ω is the angular frequency. We note that $\boldsymbol{k}$ is a vector oriented along the direction of wave propagation and describes the wave velocity and its wavelength.

The displacement fields, longitudinal and shear can then be written as,

$$\boldsymbol{u}_L = \nabla.\phi \qquad \text{Equation A1-4}$$

$$\boldsymbol{u}_S = \nabla \times \psi \qquad \text{Equation A1-5}$$

Substituting Equation A1-4 and Equation A1-5 in Equation A1-2 and Equation A1-3 yield the wave velocities as,

$$c_L = \sqrt{\frac{\lambda+\mu}{\rho}} = \alpha \qquad \text{Equation A1-6}$$

and

$$c_S = \sqrt{\frac{\mu}{\rho}} = \beta \qquad \text{Equation A1-7}$$

where c_L or α is the longitudinal wave velocity, and c_S or β is the shear wave velocity in the medium.

For the computation of the supported lateral waves in the medium, it is necessary to first specify the assumptions used:

1) The analytical model assumes that the materials are isotropic in nature. In case of the anisotropic materials such as silicon, it is necessary to calculate the equivalent isotropic material properties along the device orientation.

2) Plane Strain - The plate depth is ignored. Since the wavelengths are much smaller than the lateral geometry, the validity of a plane strain analysis is assumed.

3) Plate boundaries are ignored, *i.e.* the plate is assumed to have infinite lateral geometries

With these assumptions, the displacement equations for longitudinal and shear waves can be written as

$$\boldsymbol{u}_L = \nabla.\phi = \begin{Bmatrix} k_1 \\ k_2 \\ 0 \end{Bmatrix} A_L e^{i(\boldsymbol{k}.\boldsymbol{x}-\omega t)} \,, \qquad \text{Equation A1-8}$$

$$\boldsymbol{u}_S = \nabla \times \psi = \begin{Bmatrix} k_1 \\ -k_2 \\ 0 \end{Bmatrix} A_S e^{i(\boldsymbol{k}.\boldsymbol{x}-\omega t)} \,. \qquad \text{Equation A1-9}$$

For the analysis of layered media, it is necessary to consider a total of eight waves at each material interface, four incident longitudinal and shear waves (two from above and two from below) and four reflected longitudinal and shear waves (two from above and two from below). Thus, each layer will have a total of four waves (two incident and two reflected or transmitted) as shown in Figure A1-1. Now, for these waves to interact, they need to share the same frequency and lateral wavenumber at each interface, in accordance with Snell's law and thus all equations for stress and displacement have the same frequency and x component of wavenumber (k_1).

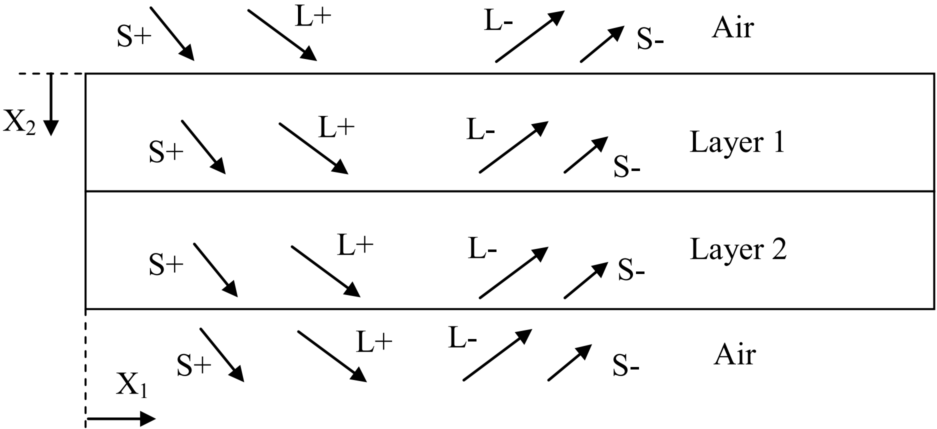

Figure A1-1. A multi-layer plate model with two material layers surrounded by air.

Due to the constraints from Snell's law, we can write

$$\frac{k_1}{\omega} = \frac{1}{c_{ph}} = \frac{\sin(\theta_L)}{\alpha} = \frac{\sin(\theta_S)}{\beta}, \qquad \text{Equation A1-10}$$

where c_{ph} is the phase velocity, and θ_L and θ_S denote the angles at which the longitudinal and shear waves propagate with respect to X_2. The displacement and stresses across a given layer has contributions from the four waves in each layer. Since, we have continuity of displacement and stress at the interfaces, we can write the system equations in the form,

$$\begin{Bmatrix} u_1 \\ u_2 \\ \sigma_{22} \\ \sigma_{12} \end{Bmatrix} = [m_{ij}].\begin{Bmatrix} A_{L+} \\ A_{L-} \\ A_{S+} \\ A_{S-} \end{Bmatrix}, \qquad \text{Equation A1-10}$$

where A terms are the amplitudes of the respective incident and reflected longitudinal and shear waves, u and σ are the relevant displacement and stress components, m_{ij} are the coefficients calculated using material properties of the layer and its dimension normal to X_1. The above Equation A1-10 summarizes the field parameters of interest in the estimation of the lateral dispersion curves. Since we have continuity of stress and displacement, at each interface we have,

$$\begin{Bmatrix} u_1 \\ u_2 \\ \sigma_{22} \\ \sigma_{12} \end{Bmatrix}_{layer\ 1,\ bottom} = \begin{Bmatrix} u_1 \\ u_2 \\ \sigma_{22} \\ \sigma_{12} \end{Bmatrix}_{layer\ 2,\ top} . \qquad \text{Equation A1-11}$$

Using Equation A1-11, we can express the stresses and displacements in one layer as a function of those in the adjacent layer. Thus, by including the $[m_{ij}]$ for each layer, we can write,

$$\begin{Bmatrix} u_1 \\ u_2 \\ \sigma_{22} \\ \sigma_{12} \end{Bmatrix}_{1^{st}\ layer,\ bottom} = [S] \begin{Bmatrix} u_1 \\ u_2 \\ \sigma_{22} \\ \sigma_{12} \end{Bmatrix}_{n^{th}\ layer,\ bottom} , \qquad \text{Equation A1-12}$$

where $[S]$ is the layered matrix and can be written in terms of $[m_{ij}]$ in each layer. At the boundaries we have air interfaces for which we require stress free boundaries and thus $\sigma_{ij} = 0$. Now, we can rewrite the system equation as

$$\begin{Bmatrix} u_1 \\ u_2 \\ 0 \\ 0 \end{Bmatrix}_{plate,\ bottom} = \begin{Bmatrix} u_1 \\ u_2 \\ 0 \\ 0 \end{Bmatrix}_{plate,\ top} . \qquad \text{Equation A1-13}$$

The characteristic equation can be obtained by solving for the stresses and is written as

$$\begin{Bmatrix} 0 \\ 0 \end{Bmatrix}_{plate,\ bottom} = \begin{bmatrix} S_{31} & S_{32} \\ S_{41} & S_{42} \end{bmatrix} \begin{Bmatrix} 0 \\ 0 \end{Bmatrix}_{plate,\ top} . \qquad \text{Equation A1-14}$$

The non-trivial solution to Equation A1-14 requires

$$S_{31} \times S_{42} - S_{41} \times S_{32} = 0. \qquad \text{Equation A1-15}$$

The solution to Equation A1-15 gives the dispersion curves, *i.e.* the lateral wavenumbers that can propagate at a given frequency. The coefficients of $[S]$ are dependent on the geometry of each layer in the stack and its material properties. At a

given frequency, multiple lateral wavenumbers can exist corresponding to different Lamb modes propagating in the system.

Since it is not possible to form a generally applicable closed-form expression for the frequency as a function of wavenumber, the solutions must be obtained numerically. For the plots presented in Chapter 5, the solution is obtained using a simple MATLAB script utilizing the bisection technique to ensure a robust estimation of the dispersion curves. For a given frequency, the lateral wavenumber is varied across the range of interest and roots for that frequency are identified (change in sign of the function). The root finding algorithm is repeated around each root to get a fine resolution of the solution for the lateral wavenumber. This procedure is repeated across the range of frequencies to generate the complete dispersion diagram. It should be noted here that the simple algorithm used here has a limitation of missing redundant solutions, *i.e.* combinations of frequency and wavenumber at which two separate modes can co-exist. However, such specific non-ideal situations can be manually corrected for once the dispersion curves are known. An alternative approach to overcome this limitation is to utilize more advanced predictive curve following algorithms such as those using the Runge-Kutta methods.

BIBLIOGRAPHY

[1] E. Rubiola, Phase noise and frequency stability in oscillators, 1st ed., Cambridge: Cambridge University Press, 2008.

[2] F. Ayazi, "MEMS for integrated timing and spectral processing," in *IEEE Custom Integrated Circuits Conference*, 2009.

[3] S. Bhave, "Micro- (and nano-) mechanical signal processors," in *Proceedings of SPIE, 7679, Nano-electronics and high-frequency MEMS/NEMS*, Orlando, 2010.

[4] C. T. C. Nguyen, "MEMS technology for timing and freqeuncy control," *IEEE Transactions on Ultrasonics, Ferroelectrics and Frequency Control,* vol. 54, no. 2, pp. 251-270, 2007.

[5] "www.sitime.com," Sitime, inc., [Online]. Available: www.sitime.com. [Accessed 18 November 2012].

[6] "www.discera.com," [Online]. Available: www.discera.com. [Accessed 18 November 2012].

[7] "www.idt.com," [Online]. Available: www.idt.com. [Accessed 18 November 2012].

[8] A. Hajimiri and T. Lee, "A general theory of phase noise in electrical oscillators," *IEEE Journal of Solid-State Circuits,* vol. 33, no. 2, pp. 179-194, 1998.

[9] H. Lee, A. Partridge and F. Assaderaghi, "Low jitter and temperature stable MEMS oscillators," in *IFCS*, Baltimore, 2012.

[10] S. Pourkamali, A. Hashimura, R. Abdolvand, G. Ho, A. Erbil and F. Ayazi, "High-Q Single Crystal Silicon HARPSS Capacitive Beam Resonators with Sub-micron Transduction Gaps," *IEEE/ASME Journal of Microelectromechanical Systems,* vol. 12, no. 4, pp. 487-496, 2003.

[11] J. T. M. v. Beek and R. Puers, "A review of MEMS oscillators for frequency reference and timing applications," *Journal of Micromechanics and Microengineering,* vol. 22, no. 1, p. 013001, 2012.

[12] V. Thakar and M. Rais-Zadeh, "Optimization of tether geometry to achieve low anchor loss in Lamé-mode resonators," in *IFCS*, Prague, 2013.

[13] G. Ho, K. Sundaresan, S. Pourkamali and F. Ayazi, "Micromechanical IBARs: tunable high-Q resonators for temperature-compensated reference oscillators," *IEEE/ASME J. of Microelectromechanical Systems,* vol. 19, no. 3, pp. 503-515, 2010.

[14] S. Tallur, T. Cheng, S. Sridaran and S. Bhave, "Motional impedance analysis: bridging the 'gap' in dielectric transduction," in *IEEE International frequency control Symposium*, San Francisco, 2011.

[15] J. Yang, An Introduction to the Theory of Piezoelectricity, Springer US, 2005.

[16] G. Piazza, R. Abdolvand, G. Ho and F. Ayazi, "Piezoelectrically-transduced, capacitively-tuned, high-Q single-crystal silicon micromechanical resonators on SOI wafers," *Sensors and Actuators A,* vol. 111, no. 1, pp. 71-78, 2004.

[17] V. Thakar, Z. Wu, A. Peczalski and M. Rais-Zadeh, "Piezoelectrically transduced temperature-compensated flexural-mode silicon resonators," *JMEMS,* vol. 22, no. 3, pp. 819-823, 2013.

[18] V. Gokhale, J. Roberts and M. Rais-Zadeh, "High Performance bulk mode Gallium Nitride Resonators and Filters," in *International Conference on Solid-State Sensors, Actuators and Microsystems (Transducers'11)*, Beijing, 2011.

[19] "http://www.oemgroupinc.com/ams.php," OEM Group, inc, [Online]. Available: http://www.oemgroupinc.com/ams.php. [Accessed 17 April 2014].

[20] D. Moy, "Avago Technologies' FBAR filter technology designed into latest generation of 4G and LTE Smartphones," [Online]. Available: www. avagotech.com/fbar. [Accessed 1 July 2013].

[21] Z. Wu and e. al., "Piezoelectrically transduced high-Q silica micro resonators," in *IEEE International Conference on Microelectromechanical Systems (MEMS'13)*, Taipei, Taiwan, 2013.

[22] T. Nan, Y. Hui, M. Rinaldi and N. X. Sun, "Self-Biased 215MHz Magnetoelectric NEMS Resonator for Ultra-Sensitive DC Magnetic Field Detection," *Scientific Reports,* no. 3, p. 1985, 2013.

[23] A. Rahafrooz, A. Hajjam, B. Tousifar and S. Pourkamali, "Thermal actuation, a suitable mechanism for high frequency electromechanical resonators," in *IEEE International Conference on Microelectromechanical Systems (MEMS'10)*, Cancun, Mexico, 2010.

[24] R. Tabrizian, M. Rais-Zadeh and F. Ayazi, "Effect of phonon interactions on limiting the f.Q product of micromechanical resonators," in *Solid-State Sensors, Actuators and Microsystems (Transducers'09)*, Denver, 2009.

[25] S. Chandorkar, "Limits of quality factor in bulk-mode micromechanical resonators," in *MEMS*, Tucson, 2008.

[26] A. Akhieser, "On the absorption of sound in solids," *Journal of Physics, Academy of Sciences USSR,* vol. 1, no. 4, pp. 277-287, 1939.

[27] L. Landau and G. Rumer, "über schallabsorption in festen körpern," in *Collected papers of L. D. Landau*, 2 ed., D. T. Harr, Ed., 1967, pp. 187-192.

[28] R. Candler and e. al, "Investigation of energy loss mechanisms in micromechanical resonators," in *12th International Conference on Solid-State Sensors, Actuators and Microsystems (Transducers '03)*, 2003.

[29] K. Wang, A.-C. Wong and C. Nguyen, "VHF free-free beam high-Q micromechanical resonators," *Journal of Microelectromechanical Systems,* vol. 9, no. 3, pp. 347-360, 2000.

[30] Z. Hao, A. Erbil and F. Ayazi, "An analytical model for support loss in micromachined beam resonators with in-plane flexural vibrations," *Sensors and Actuators A,* vol. 109, pp. 156-164, 2003.

[31] Z. Hao and B. Liao, "An analytical study on interfacial dissipation in piezoelectric rectangular block resonators with in-plane longitudinal-mode vibrations," *Sensors and Actuators A,* vol. 163, pp. 401-409, 2010.

[32] D. Bindel and S. Govindjee, "Elastic PMLs for resonator anchor loss simulation," *International Journal for Numerical Methods in Engineering,* vol. 64, pp. 789-818, 2005.

[33] R. Melamud, "Temperature-compensated high-stability silicon resonators," *Applied Physics Letters,* vol. 90, no. 24, p. 244107, 2007.

[34] R. Tabrizian, G. Casinovi and F. Ayazi, "Temperature-stable high-Q AlN-on-silicon resonators with embedded array of oxide pillars," in *Hilton Head*, Hilton Head Island, 2010.

[35] A. Samarao and F. Ayazi, "Temperature compensation of silicon resonators via degenerate doping," *IEEE Transactions on Electron Devices,* vol. 59, no. 1, pp. 87-93, 2012.

[36] H. Zhu, G. C. Shan, C. Tu and J. E. Lee, "Crystallographic and eigenmode dependence of TCf for single crystal silicon contour mode resonators," in *IEEE Micro Electro Mechanical Systems (MEMS '13)*, Taipei, Taiwan, 2013.

[37] V. Thakar, Z. Wu, C. Figueroa and M. Rais-Zadeh, "A temperature-stable clock using multiple temperature-compensated micro-resonators," in *IEEE International*

Frequency Control Symposium, Taipei, Taiwan, 2014.

[38] W. Pan, V. Thakar, M. Rais-Zadeh and F. Ayazi, "Acoustically coupled thickness-mode AlN-on-Si bandpass filters, Part I: principle and devices," *IEEE Transactions Ultrasonics, Ferroelectrics and Frequency Control,* vol. 59, no. 10, pp. 2262-2269, 2012.

[39] V. Thakar and M. Rais-Zadeh, "Temperature-Compensation and Piezoelectric Actuation of Lamé-mode Resonators," in *MEMS 2014*, San Francisco, 2014.

[40] V. Thakar, W. Pan, F. Ayazi and M. Rais-Zadeh, "Acoustically coupled thickness-mode AlN-on-Si bandpass filters, Part II: simulation and analysis," *IEEE Transactions on Ultrasonics, Ferroelectrics and Frequency Control,* vol. 59, no. 10, pp. 2270-2277, 2012.

[41] G. Bahl and e. al., "Observations of fixed and mobile charge in composite MEMS resonators," in *Solid-State Sensors, Actuators, and Microsystems Workshop (Hilton Head 2008)*, Hilton Head Island, 2008.

[42] "http://www.comsol.com/showroom/gallery/1439/," [Online]. Available: http://www.comsol.com/showroom/gallery/1439/,. [Accessed 18 November 2012].

[43] R. Abdolvand, H. Johari, G. Ho, A. Erbil and F. Ayazi, "Quality factor in trench-refilled polysilicon beam resonators," *IEEE/ASME Journal of Microelectromechanical Systems,* vol. 15, no. 3, pp. 471-478, 2006.

[44] F. Ayazi, R. Tabrizian and S. L, "Compensation, tuning, and trimming of MEMS resonators," in *IEEE International Frequency Control Symposium (IFCS '12)*, 2012.

[45] Z. Wu, A. Peczalski and M. Rais-Zadeh, "Device-layer ovenization of fused silica micromechanical resonators for temperature-stable operation," in *Solid-State Sensors, Actuators, and Microsystems Workshop (Hilton Head 2014)*, Hilton Head Island, 2014.

[46] Z. Wu, A. Peczalski, V. Thakar and M. Rais-Zadeh, "A low phase-noise Pierce oscillator using a piezoelectric-on-silica micromechanical resonator," in *17th International Conference on Solid-State Sensors, Actuators and Microsystems (Transducers '13)*, Barcelona, 2013.

[47] C. Jha and e. al., "Thermal isolation of encapsulated MEMS resonators," *IEEE/ASME Journal of Microelectromechanical Systems,* vol. 17, no. 1, pp. 175-184, 2008.

[48] C. Zuo, N. Sinha, J. Spiegel and G. Piazza, "Multifrequency pierce oscillators based on piezoelectric AlN contour-mode MEMS technology," *IEEE/ASME Journal of Microelectromechanical Systems,* vol. 19, no. 3, pp. 570-580, 2010.

[49] G. Gonzalez, Foundation of Oscillator Circuit Design, Norwood, MA: Artech House, 2006.

[50] R. Tabrizian, M. Pardo and F. Ayazi, "A 27 MHz temperature compensated MEMS oscillator with sub-ppm instability," in *IEEE International Conference on Microelectromechanical Systems (MEMS '12)*, 2012.

[51] G. Ho, K. Sundaresan, S. Pourkamali and F. Ayazi, "Temperature Compensated IBAR Reference Oscillators," in *IEEE International Conference on Microelectromechanical Systems*, Istanbul, 2006..

[52] R. Abdolvand, H. Lavasani, G. Ho and F. Ayazi, "Thin-film piezoelectric-on-silicon resonators for high-frequency reference oscillator applications," *IEEE Transactions on Ultrasonics, Ferroelectrics and Frequency Control,* vol. 55, no. 12, p. 2596, 2008.

[53] H. Bhugra, W. Pan, D. Lei and S. Lee, "Introducing high performance crystalfree™ pMEMS oscillators," in *IEEE International Frequency Control Symposium (IFCS '12)*, Baltimore, 2012.

[54] R. Candler and e. al., "Long-Term and Accelerated Life Testing of a Novel Single-Wafer Vacuum Encapsulation for MEMS Resonators," *Journal of Microelectromechanical Systems ,* vol. 15, no. 6, pp. 1446-1456, 2006.

[55] Y. Cheng, L. Lin and K. Najafi, "Localized silicon fusion and eutectic bonding for MEMS fabrication and packaging," *IEEE/ASME Journal of Microelectromechanical Systems,* vol. 9, no. 1, pp. 3-8, 2000.

[56] R. Tabrizian, G. Casinovi and F. Ayazi, "Temperature-Stable Silicon Oxide (SilOx) Micromechanical Resonators," *IEEE Transactions on Electron Devices,* vol. 60, no. 8, pp. 2656-2663, 2013.

[57] G. Piazza, P. Stephanou and A. Pisano, "Piezoelectric Aluminum Nitride Vibrating Contour-Mode MEMS Resonators," *IEEE/ASME Journal of Microelectromechanical Systems,* vol. 15, no. 6, pp. 1406-1418, 2006.

[58] A. Ansari, V. Gokhale, V. Thakar, J. Roberts and M. Rais-Zadeh, "Gallium nitride-on-silicon micromechanical overtone resonators and filters," in *IEEE Electron Device Meeting (IEDM '11)*, Washington, 2011.

[59] M. Rinaldi, C. Zuniga, C. Zuo and G. Piazza, "Super-High-Frequency Two-Port AlN Contour-Mode Resonators for RF Applications," *IEEE Transactions on Ultrasonics, Ferroelectrics, and Frequency Control,* vol. 57, no. 1, pp. 38-45, 2010.

[60] J. Lee, J. Yan and A. Seshia, "Study of lateral mode SOI-MEMS resonators for reduced anchor loss," *J. Micromech. Microeng.,* vol. 21, p. 045010, 2011.

[61] L. Khine, M. Palaniapan and W.-K. Wong, "6Mhz Bulk-Mode Resonator with Q Values Exceeding One Million," in *14th International Conference on Solid-State Sensors, Actuators and Microsystems (Transducers '07)*, 2007.

[62] L. Khine, M. Palaniapan and W.-K. Wong, "12.9MHz Lame-Mode Differential SOI Bulk Resonators," in *15th International Conference on Solid-State Sensors, Actuators and Microsystems (Transducers '09)*, 2009.

[63] Z. Hao and F. Ayazi, "Support Loss in the Radial Bulk-mode Vibrations of Center-supported Micromechanical Disk Resonators," *Sensors and Actuators A,* vol. 134, pp. 582-593, 2007.

[64] J.-P. Bérenger, "A perfectly matched layer for the absorption of electromagnetic waves," *Journal of Computational Physics,* vol. 114, pp. 185-200, 1994.

[65] A. Frangi, A. Bugada, M. Martello and P. Savadkoohi, "Validation of PML-based models for the estimation of anchor dissipation in MEMS Resonators," *European Journal of Mechanics A,* vol. 37, pp. 256-265, 2013.

[66] "www.comsol.com," COMSOL, inc., [Online]. Available: www.comsol.com.

[67] P. Laura, J. Pombo and E. Susemihl, "A note on the vibrations of a clamped-free beam with a mass at the free end," *Journal of Sound and Vibration,* vol. 37, no. 2, pp. 161-168, 1974.

[68] G. Ho, K. Sundaresan, S. Pourkamali and F. Ayazi, "Low-motional-impedance highly-tunable I2 resonators for temperature-compensated reference oscillators," in *IEEE International Conference on Microelectromechanical Systems (MEMS '05)*, 2005.

[69] "http://www.ioffe.ru/SVA/NSM/Semicond/index.html," [Online]. Available: http://www.ioffe.ru/SVA/NSM/Semicond/index.html. [Accessed 18 November 2012].

[70] D. Serrano, R. Tabrizian and F. Ayazi, "Electrostatically Tunable Piezoelectric-on-Silicon Micromechanical Resonator for Real Time Clock," *IEEE Transactions on Ultrasonics, Ferroelectrics, and Frequency Control,* vol. 59, no. 3, pp. 358-365, 2012.

[71] J. Kittl and e. al., "Silicides and germanides for nano-CMOS applications," *Materials Science and Engineering: B,* Vols. 154-155, pp. 144-154, 2008.

[72] R. Vazny and e. al., "Front-end implications to multi-standard cellular radios: State-of-the-art and future trends," in *IEEE Ultrasonics Symposium*, 2010.

[73] R. Aigner, "SAW and BAW technologies for RF filter applications: a review of the

relative strengths and weaknesses," in *IEEE Ultrasonics Symposium,*, 2008.

[74] D. Shick and H. Tiersten, "An Analysis of thickness-extensional trapped energy mode transducers," in *IEEE Ultrasonics Symposium*, 1982.

[75] T. Pensala, J. Meltaus, K. Kokkonen and M. Ylilammi, "2-D modeling of laterally acoustically coupled thin film bulk acoustic wave resonator filters," *IEEE Transactions on ultrasonics, ferroelectrics, and frequency control,* vol. 57, no. 11, 2010.

[76] R. Milsom, "Analysis and design of coupled-mode miniature bar resonators and monolithic filters," *IEEE Transactions on Sonics and Ultrasonics,* vol. 30, no. 3, 1983.

[77] P. Bradley, "2X size and cost reduction of film bulk acoustic resonator (FBAR) chips with tungsten electrodes for PCS/GPS/800 MHz multiplexers," in *IEEE Ultrasonics Symposium*, New York, 2007..

[78] W. Pan, R. Abdolvand and F. Ayazi, "A low-loss 1.8GHz monolithic thin-film piezoelectric-on-substrate filter," in *IEEE MEMS Conference*, Tucson, 2008..

[79] R. Abdolvand and F. Ayazi, "Enhanced power handling and quality factor in thin-film piezoelectric-on-substrate resonators," in *IEEE Ultrasonics Symposium*, 2007.

[80] W. Pan and F. Ayazi, "Multiple-frequency thickness-mode thin-film piezoelectric-on-substrate filter array," in *IEEE International Frequency Control Symposium*, 2008.

[81] R. Abdolvand and F. Ayazi, "Monolithic thin-film piezoelectric-on-substrate filters," in *IEEE/MTT-S International Microwave Symposium Tech. Digest*, 2007.

[82] IEEE Standard on Piezoelectricity, IEEE, 1987, p. 59.

[83] W. Mason, "Equivalent Electromechanical Representation of Trapped Energy Transducers," *Proceedings of the IEEE,* vol. 57, no. 10, 1969.

[84] M. Lowe, "Matrix techniques for modeling ultrasonic waves in multilayered media," *IEEE Transactions on Ultrasonics, Ferroelectrics and Frequency Control,* vol. 42, no. 4, pp. 525-541, 1995.

[85] Dworsky, "An Improved Circuit Model for Monolithic Crystal Filters," *Transactions on Sonics and Ultrasonics,* vol. 28, no. 4, 1981.

[86] W. Beaver, Theory and design principle of the monolithic crystal filter, PhD dissertation, Lehigh University, 1967.

[87] K. Lakin, "Coupled resonator filters," in *Proceedings of IEEE Ultrasonics*

Symposium, Germany, 2002.

[88] H. Tiersten and D. Stevens, "An analysis of thickness-extensional trapped energy resonant device structures with rectangular electrodes in the piezoelectric thin film on silicon configuration," *Journal of Applied Physics,* vol. 54, no. 10, 1983.

[89] D. Pozar, in *Microwave Engineering*, Addison Wesley, 1990, p. 217 and 235.

[90] M. Dubois and P. Muralt, "Properties of AlN thin films for piezoelectric transducers and microwave filter applications," *Applied Physics Letters,* vol. 74, p. 20, 1999.

[91] M. Dubois and P. Muralt, "Stress and piezoelectric properties of aluminum nitride thin films deposited onto metal electrodes by pulsed direct current reactive sputtering," *Journal of Applied Physics,* vol. 89, no. 11, 2001.

[92] D. King and S. Gopani, "SAW filters in CDMA mobile communication networks," in *Proc. Wireless Technologies China '99*, 1999.

[93] K. Graff, Wave Motion in Elastic Solids, Dover, 1991.